Andrés Felipe Bolaños Acosta

Two approximations for solving non-equilibrium condensation shocks in supersonic nozzle flows

São Paulo
August 2022

Andrés Felipe Bolaños Acosta

Two approximations for solving non-equilibrium condensation shocks in supersonic nozzle flows

Revised Version

Dissertation submitted to Escola Politécnica
da Universidade de São Paulo
for the Degree of Master in Science.

Concentration Area:
Mechanical Engineering
Energy and Fluids

Advisor:
Prof. Dr. José Roberto Simões-Moreira

São Paulo
2022

Este exemplar foi revisado e corrigido em relação à versão original, sob responsabilidade única do autor e com a anuência de seu orientador.

São Paulo, _____ de _____ de _____

Assinatura do autor: _____

Assinatura do orientador: _____

Catalogação-na-publicação

Bolaños-Acosta, Andrés Felipe

Two approximations for solving non-equilibrium condensation shocks in supersonic nozzle flows. / A. F. Bolaños-Acosta -- versão corr. -- São Paulo, 2022.

113 p.

Dissertação (Mestrado) - Escola Politécnica da Universidade de São Paulo. Departamento de Engenharia Mecânica.

1.Escoamento compressível 2.Gás Real 3.Condensação 4.Vapor d'água 5.Dióxido de carbono I.Universidade de São Paulo. Escola Politécnica. Departamento de Engenharia Mecânica II.t.

"Un hombre solo tiene derecho a mirar a otro hacia abajo cuando ha de ayudarle a levantarse."
Gabriel Garcia Márquez

"The cave you fear to enter holds the treasure you seek."
Joseph Campbell

"All the darkness in the world cannot extinguish the light of a single candle."
St. Francis of Assisi

LIST OF FIGURES

LIST OF TABLES

ACRONYMS

CFD Computational Fluid Dynamics

CNT Classical Nucleation Theory

DDT Deflagration-Detonation Theory

DGT Droplet Growth Theory

EoS Equations-of-State

INT Interferometry

iPRSV improved Peng-Robinson with the Stryjek-Vera modification

LLS Laser-Light Scattering

SANS Small-Angle Netron Scattering

SAXS Small-Angle X-ray Scattering

SFM Single-Fluid Model

SPM Static Pressure Meassurements

SW Span and Wagner

TFM Two-Fluid Model

NOTATIONS

Symbols

P	Pressure, [Pa]
ρ	Density, [kg m^{-3}]
$\tilde{\rho}$	Two-phase non-equilibrium density, [kg m^{-3}]
T	Temperature, [K]
c_v	Isochoric heat capacity, [J kg^{-1} K^{-1}]
c_p	Isobaric heat capacity, [J kg^{-1} K^{-1}]
γ	Specific heat ratio, [-]
w	Speed of sound, [m s^{-1}]
h	Specific enthalpy, [J kg^{-1} K^{-1}]
$\tilde{h}$	Two-phase non-equilibrium enthalpy, [J kg^{-1} K^{-1}]
$\boldsymbol{A}$	Dimensionless Helmholtz free energy, [-]
ϕ	Specific Helmholtz free energy, [J kg^{-1}]
R	Real gas constant, [m^3 Pa K^{-1} mol^{-1}]
s	Specific entropy, [J kg^{-1} K^{-1}]
$\tilde{s}$	Two-phase non-equilibrium entropy, [J kg^{-1} k^{-1}]
$\tilde{e}$	Two-phase non-equilibrium internal energy, [J kg^{-1}]
v	Molar volume, [m^3 mol^{-1}]
ω	Acentric factor, [-]
M	Arbitrary thermodynamic property
Z	Compressibility factor, [-]
$\varnothing$	Fugacity coefficient, [-]
f	Fugacity, [Pa]
Ma	Mach number, [-]
u	Velocity, [m s^{-1}]
a	Fluid parameter, [Pa m^6 kg^{-2}]
a_c	Fluid's critical coefficient
A	Area, [m^2]
q	Specific heat, [J kg^{-1}]
X	Vapor quality, [-]
χ	Reduced temperature parameter, [-]
k	iPRSV's acentric parameter, [-]
$\mathbf{J}$	Mass flux, [kg s^{-1} m^{-2}]
S	Supersaturation ratio, [-]
ΔT	Amount of subcooling, [K]
ΔG	Gibb's free energy variation, [J kg^{-1}]
ΔG^*	Gibb's free energy barrier, [J kg^{-1}]

r	Droplets' radius, [m]
r^*	Droplets' critical radius, [m]
$\bar{r}$	Mean radius, [m]
σ	Surface tension, [N m^{-1}]
q_c	Condensation coefficient [-]
k_B	Boltzmann constant, [m^2 kg s^{-2} K^{-1}]
J	Nucleation rate, [m^3 s^{-1}]
κ	Kinetic factor, [-]
C	Non-isothermal correction factor, [-]
ξ	Calibration factor, [-]
τ^*	Characteristic time, [s]
Kn	Knudsen number, [-]
μ	Dynamic viscosity, [Pa s]
$\widetilde{l}$	Mean free path, [m]
α	Transport coefficient, [m^2 s^{-1}]
$\dot{Q}$	Latent heat released, [J kg^{-1}]
m_c	Condensing mass flow rate, [kg s^{-1}]
λ	Conductivity, [W m^{-1} K^{-1}]
Pr	Prandtl number, [-]
ς	Correction factor, [-]
ψ	Calibration parameter, [-]
t	Time, [s]
y	Wetness fraction, [-]
N	Number of droplets per unit mass [kg^{-1}]
Err	Accepted error level, [-]
I	Momentum integral term, [Pa m^2]
ϵ, ϱ	Roots cubic equations-of-state, [-]
τ_1, τ_2	iPRSV's temperature factors, [-]
Υ, Ψ	Fluid parameter ratios, [-]

Subscripts

c	Critical fluid's condition
r	Reduced condition
π	Phase
l	Liquid
v	Vapor
ref	Reference
sat	Saturated state
d	Droplet

continue...

o	Stagnated
xj	Arbitrary nozzle location

Superscripts

r	Residual part
o	Ideal part
$**$	Guess value

CONTENTS

ACKNOWLEDGEMENTS

Firstly, I want to express my gratitude to God for giving me enough strength and faculties to complete my Master's studies. I am also grateful with him for putting such valuable people in my life.

I would like to express my very great appreciation to my supervisor Prof. Dr. José Roberto Simões-Moreira for opening the doors and giving me a place to develop my research in the SISEA laboratory. I am thankful for his comprehension, attention, help and guidance during this academic research.

My special thanks are extended to my fellows in the laboratory. To Beethoven Narvaez-Romo for his unconditional companionship, help and encouragement. I would also like to thank to Julian Camilo Restrepo for his friendship, assistance and useful critiques of this work. I thank Lina Maria Varon, Gustavo Barreto, Eliane Suzuki, Larissa Costa Sobral and Wellorzon Novais for their valuable friendship and enjoyable conversations in the laboratory.

My deep gratitude to my parents; to my mother Tirza Acosta for her unconditional support and encouragement throughout every project in my life. To my father Servio Tulio Bolaños for his earnest attention and comprehension. Their exemplarity has always encouraged me to give my best and to take up challenges. Without their support the realization of this research would not have been possible.

I also would like to acknowledge the Research Centre for Greenhouse Gas Innovation (RCGI) and Shell/Brazil Company for the financial support during this investigation period.

RESUMO

Condensação em condições de não equilíbrio ocorre em aplicações de engenharia como turbinas a vapor, injetores, compressores supercríticos de dióxido de carbono e separadores supersônicos. Em consequência, modelagens deste fenômeno são realizadas na área. Esta pesquisa descreve duas aproximações para a caracterização de choques de condensação em escoamentos supersônicos. Uma modelagem de gás cinética foi desenvolvida com base na aproximação de um modelo de fluido único, que consiste no acoplamento dos conceitos de nucleação e de crescimento de gotículas à solução de equações algébricas de conservação para escoamento compressível. O segundo método assume a transição de fase como uma descontinuidade no escoamento, sendo que as condições de salto através do choque de condensação são determinadas a partir das interseções nas curvas Rayleigh e Hugoniot. Os dois métodos foram implementados assumindo o estado estacionário em um modelo de escoamento quase-unidimensional, usando equações cúbicas e multiparamétricas para reproduzir o comportamento não ideal em escoamentos de vapor e de dióxido de carbono. Várias simulações foram realizadas para diferentes geometrias de bocal e condições de fluxo. Os resultados mostram que a solução da detonação fraca na modelagem da descontinuidade, a aproximação gas-cinética estimam com precisão a recuperação de pressão que ocorre na condensação em escoamentos supersônicos. O modelo indicou que as linhas de pressão nas expansões têm baixo desvio com respeito aos dados experimentais da fase vapor d'água (menores que 3%), sendo que as discrepâncias menores que 8% foram atingidas no caso do dióxido de carbono. A estimativa da distribuição do tamanho médio do raio das gotículas apresenta a ordem de magnitude dos valores experimentais reportados na literatura.

Palavras-chave: choques de condensação. escoamentos supersônicos. gás real, vapor, dióxido de carbono.

ABSTRACT

Non-equilibrium condensation occurs in engineering applications such as steam turbines, injectors, carbon dioxide supercritical compressors and supersonic gas flow separators. Consequently, any model able to characterize such a phenomenon is pursued in the field. This Master's dissertation describes two approximations for solving condensation shocks in supersonic nozzle flows. A gas-kinetic model has been developed based on a Single Fluid Model approximation, which consists of coupling nucleation and droplet growth concepts to the solution of algebraic conservation equations for compressible flow. The second method assumes the phase transition as a flow discontinuity, the jump conditions across the condensation shock are determined from intersections on Rayleigh and Hugoniot curves. Both methods have been implemented assuming steady-state in a quasi-one-dimensional flow model, and using cubic and complex multi-parameter equations-of-state in order to reproduce the non-ideal gas flow behavior of steam and carbon dioxide. Several simulations were performed in different nozzle geometries and flow conditions. The results shows that the weak detonation state from the discontinuity model, and the implemented gas-kinetic approximation estimate with accuracy the pressure recovery that occurs in condensing nozzle flows. It has been found that the predicted pressure expansion lines are in agreement with experimental data for steam, and discrepancies within 8% were found for the carbon dioxide case. The estimated average droplet radius size distribution presents the order of magnitude of the experimental values reported by the literature.

Keywords: condensation shocks. supersonic nozzle flows. real-gas, steam, carbon dioxide.

1 INTRODUCTION

The phenomenon of condensation is simply defined as "the process of a gas changing into liquid "(Simpson; Weiner, 1989). It occurs in natural events such as cloud formation, and the growth of droplets on cooled surfaces due to thermal and chemical interactions (Sidin, 2009).

The process that triggers condensation is known as nucleation and it is driven by two mechanisms: homogeneous and heterogeneous ones. These mechanisms differs on how they are initialized. The homogeneous case, also known as spontaneous condensation involves the formation of liquid clusters due to molecular collisions in supersaturated vapor (Lamanna, 2000). In the heterogeneous case foreign particles such as impurities activate the condensation process (Fakhari, 2010). Foggy mirrors, foggy windshields and cloud formation are examples of heterogeneous nucleation (Pandey, 2014). Homogeneous nucleation, on the other hand, occurs in flow at high speeds namely supersonic, such as the flow surrounding a supersonic aircraft and in nozzles (Sidin, 2009). (Fig. 1.1 displays other examples of this type of condensation).

(a)

(b)

Figure 1.1 – Examples of condensation in metaestable flow conditions: (a) flow surrounding a supersonic aircraft, (b) Wilson cloud in Beirut's explosion in 2020.
Fonts: (a) https://commons.wikimedia.org/wiki/File:FA-18-going-transonic, (b) https://twitter.com/nktpnd/status/1290673830676111362/photo/1

In fact, homogeneous and heterogeneous nucleation coexist in condensation processes at high speed flows. However, the high expansion rate avoids the effect of cold walls, dust, particles, salt crystals, or any impurities (Fakhari, 2010). The effects of spontaneous condensation are significantly higher than the heterogeneous ones. Hence, calculations can often neglect the effects of the heterogeneous mechanism.

Spontaneous condensation plays a primary role in engineering applications such as steam turbines (Hasini et al., 2012), injectors (Heinze, 2015) supercritical compressors (Lettieri et al., 2017) and supersonic gas flow separators (Niknam et al., 2018) as well.

Steam turbines, in conjunction with fossil-fueled and nuclear plants, supply 80% of the world's electricity demand (Fakhari, 2010). They are the most expensive piece of equipment

employed by the electrical power supply (Dykas, 2001). However, the droplets' impingement on turbine blades leads to erosion of the components and also changes flow patterns. These undesirable effects reduce steam turbines' performance efficiency and lifetime. Consequently, any model able to predict the condensation phenomenon in these devices allows losses to be determined and tracked (Dykas, 2001).

Non-equilibrium condensation also has undesirable effects on supercritical carbon dioxide compressors. This technology has emerged from the need for the reduction of the carbon dioxide footprint in propulsion and power applications. The phase-change process occurs on the suction side of the compressor's blade, due to pressure drop that bring the flow into a favorable metastable condition for liquid formation. Further, a high non-ideal behavior characterizes the phase-transition in such devices (Azzini, 2019).

On the other hand, technologies such as steam injectors and supersonic separators take advantage of condensation for operational purposes (Anand, 1993). In the case of steam injectors, the optimization and characterization of the condensation process allows driving heat exchange and mixing efficiently (Heinze, 2015); this is being widely applied to many areas of the industry, such as thermal engineering air conditioning and desalination (Trela et al., 2010).

Fig. 1.2 presents a schematic representation of a steam injector and its components: a convergent-divergent nozzle, a mixing chamber and a diffuser. The steam first expands in the convergent-divergent nozzle and produces an outlet pressure below the suction water one. The flow then enters the mixing chamber where the suction water is introduced and the condensation phenomenon (commonly referred to as condensation shocks) occurs close to the mixing chamber's throat. Finally, the two-phase mixture flows into the diffuser where the static pressure increases (Heinze, 2015).

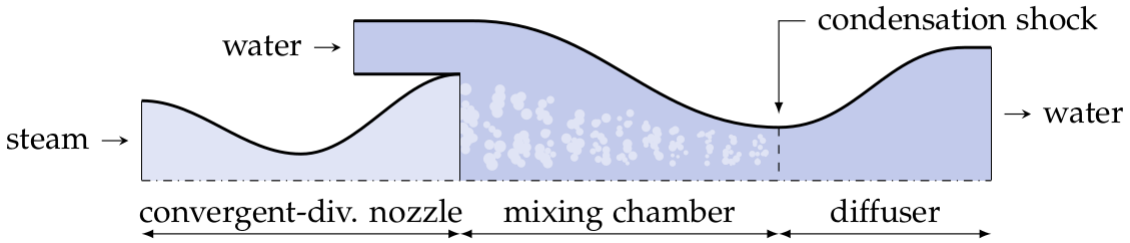

Figure 1.2 – Schematic steam injector.
Font: Heinze (2015).

Aside from conventional applications for power generation, condensation in high speed-flows plays a relevant role in gas purification applications. Therefore, supersonic gas separators are a technology that has emerged in recent years, for separation of water and other hydrocarbons from natural gas (Azzini, 2019). Their low maintenance requirements, compact design without rotating parts, and no adding of chemical solvents are some advantages that supersonic gas flow separators present concerning other separation technologies (Niknam et al., 2018). These devices are commercialized by Dutch Twister BV and Russian ENGO Engineering companies.

Fig. 1.3 displays a sketch of a supersonic separator. The flow acquires a swirl motion at the inlet, and expands inside the device's body. This reduces the temperature and static pressure, leading to the formation of droplets. Due to the swirling motion and the shape of the device's walls, the droplets are collected. The mainstream then enters into the diffuser where the static pressure is recovered (Imaev et al., 2014).

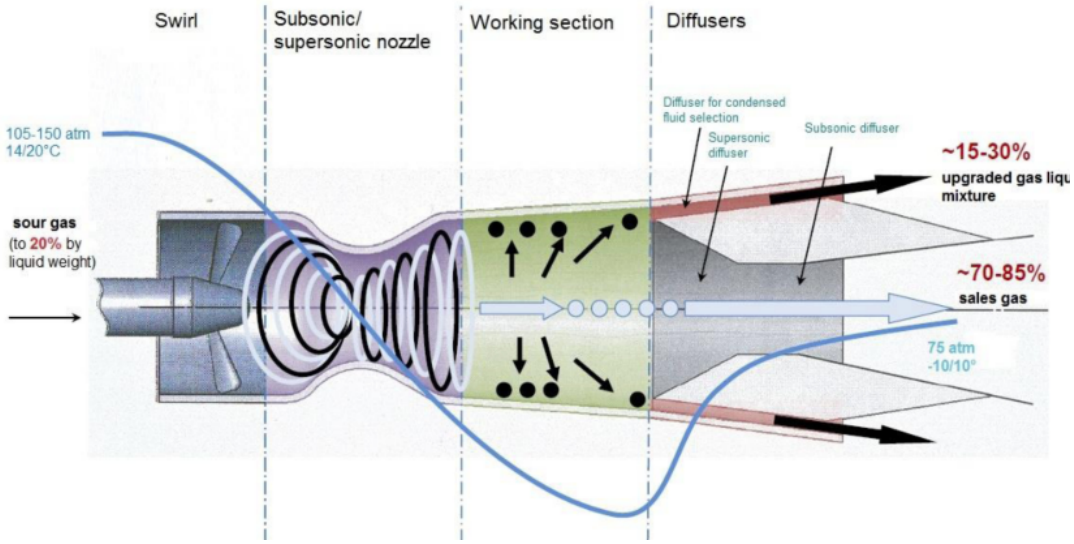

Figure 1.3 – Sketch of the supersonic separator device developed by ENGO Engineering. Font: Imaev et al. (2014).

Spontaneous condensation is a complex process, because it occurs at non-equilibrium thermodynamic conditions. This means that the flow is still dry when it reaches the saturation curve, and it continues expanding in the vapor metastable region until it attains the state known as the Wilson point (state where droplets start to form and grow); at this point a fog of small droplets form and condensation occurs (Blondel et al., 2015).

In addition to compressible flow behavior and the phase transition process, from a thermodynamic point-of-view, operating conditions of the previously described devices, present an extra challenge since thermodynamic flow conditions are not ideal; consequently, complex Equations-of-State (EoS) are required to determine them.

As discussed, a convergent-divergent nozzle (also known as a Laval nozzle) is one of the most important components in steam injectors. Such a device is widely employed to examine condensation due to the complex nature of the flow, especially in supersonic flow separators, supercritical compressors and steam turbines (Dykas, 2001; Yang; Shen, 2009). Some of the most common nozzle geometries employed for this purpose are Barschdorff (1971), Moore et al. (1973), and Moses & Stein (1978).

Non-equilibrium condensation has been analyzed from several perspectives as shown in the Fig. 1.4. Single (SFM), Two fluid models (TFM) and Method of Moments (MoM) have been studied in Computational Fluid Dynamics (CFD) numerical works. Those methods are based on nucleation and droplet growth laws from gas-kinetic theories, and characterize the droplet size distribution during nucleation and two-phase expansions processes.

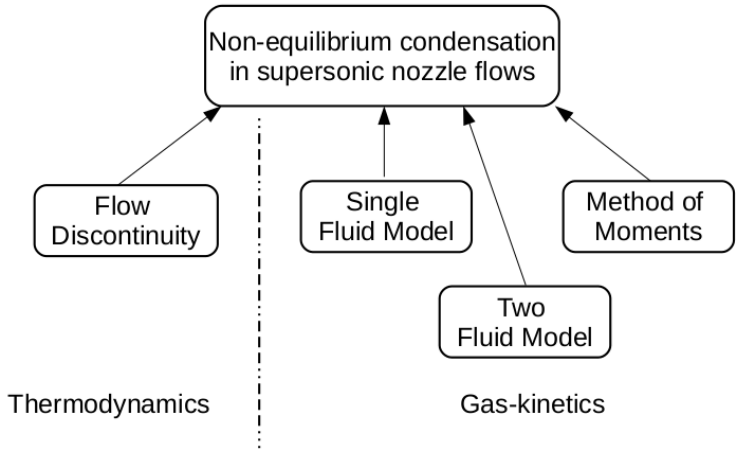

Figure 1.4 – Existing approximations for solving non-equilibrium condensation in nozzle flows. Font: Author.

MoM evaluates the lower order of the particles‘ size distributions and has been extensively employed in aerosol sciences. On the other hand, TFM applies conservation equations for both liquid and vapor phases. In this model, homogeneous condensation effects have been taken into account in source terms in the equations. However, both MoM and TFM requires high computational cost, thus, they are not the object of investigation in the present study. Moreover the SFM assumes that the two-phase dispersed flow behaves as a one fluid, thus, neglecting velocity slip between the phases and assuming averaged properties for the two-phase mixture.

Alternatively, the phase-transition in supersonic condensing flows has been approached from the Deflagration-Detonation Theory (DDT), which categorizes it as a weak detonation. According to this approximation, the flow condenses instantaneously at an specific cross-sectional area of the nozzle namely as a flow discontinuity. The intersections on the Rayleigh and Hugoniot curves determines the jump conditions across the discontinuity, making the model dependent just on the solution of the mass, energy and momentum conservation equations.

It is worth mentioning that CFD numerical works employ partial differential equations, and no CFD research using algebraic ones features on the literature. Consequently, the implementation with algebraic equations, taking into account the gas-kinetic theory and concepts involved in SFM is one aim in the present investigation. It is relevant to mention that the use of a quasi-one-model allows complex EoS to be implemented aiming to describe accurately the phase-change process in the entire operating regions where those EoS cover.

The other and the principal purpose of this research is to implement the discontinuity approximation for condensation shocks in non-ideal thermodynamic gas conditions. Since this model has so far only been implemented in earlier investigations about condensation in wind tunnels assuming perfect-gas behavior.

1.1 Objectives

The principal objective of this research is to implement and to evaluate a gas-kinetic SFM and a flow discontinuity approximations for characterizing non-equilibrium condensation in supersonic nozzle flows, using the algebraic form of conservation equations for quasi-one- dimensional flow, and taking into account non-ideal gas behavior of steam and carbon dioxide. Therefore the following specific objectives have been proposed:

- To select and to implement accurate EoS for computing thermodynamic properties of steam and carbon dioxide.
- To select an appropriate nucleation and droplet growth rate models in order to characterize the phase-transition process from a gas-kinetic approach;
- To analyze the jump conditions across the condensation shock from intersections on Rayleigh and Hugoniot curves and their physical significance; and
- To compare both approximations with available experimental data of carbon dioxide and steam under low and high pressure conditions.

1.2 Dissertation outline

In this chapter, a description of the problem is presented. It gives a definition for non-equilibrium condensation, and describes engineering applications where this phenomenon occurs, in order to determine the knowledge gaps that the current study fills.

Chapter 2 gives a general overview of the studies carried out in this field.

Chapter 3 determines the theoretical background to approach non-equilibrium condensation. This chapter presents the used real-gas EoS to take into account non-ideal gas behavior, compressible flow definitions, and two-methods for characterizing condensation shocks in supersonic nozzle flows.

A detailed description of the algorithms and procedures used to implement the EoS, and to solve compressible flow equations from the discontinuity flow and gas-kinetic approximations, is given by Chapter 4.

Chapter 5 presents the results and comparisons with experimental data of both approaches carried out with steam and carbon dioxide under several flow conditions.

Finally, Chapter 6 presents conclusions and discusses future work on the treated subject in the present study.

2 LITERATURE REVIEW

Investigations on non-equilibrium condensation in supersonic nozzles started when Prandtl showed a Schlieren picture (see Fig. 2.1) of this disturbance at the Volta congress in 1935. The researchers were baffled by the observation of two oblique condensation shock-like phenomena that appeared close to the throat, in the divergent nozzle section (Wegener, 1954). Investigations about condensation in converging-diverging nozzles have since been developed due to the engineering applications in which this phenomenon takes place. Therefore, the current work categorizes some of the existing studies in experimental and theoretical ones. It should be mentioned that the theoretical group also includes numerical studies.

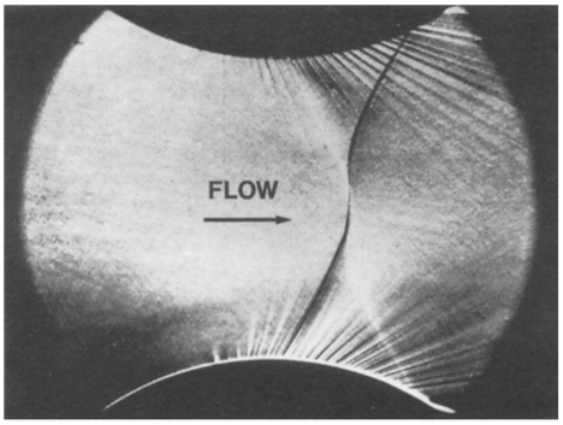

Figure 2.1 – Schlieren picture of a condensation shock presented by Prandtl.
Font: Lamanna (2000).

2.1 Overview of experimental studies

Barschdorff (1971) realized several experiments to analyze condensation shocks of steam in converging-diverging nozzles. Those experiments were executed in an arc nozzle, with a wall curvature of 584 mm and throat's height of 60 mm. The stagnation conditions were maintained at a constant pressure of 0.78390 bar, and the temperature varied from 97 to 126.75 ^{o}C. Barschdorff (1971) presented the nozzle's pressure distribution and the droplet's mean radius (which was in the order of 10^{-8} m) as well. Experiments for steam under low pressures were also carried out by Moore et al. (1973).

Other authors such as Moses & Stein (1978), also performed a series of experiments of steam condensation in a de Laval nozzle. The conditions at the nozzle's inlet were below of 0.8 bar. They used static pressure measurements and Lasser Light Scattering (LLS) techniques to document the growth of liquid-phase. Moses & Stein (1978) reported that the onset of condensation occurred in a temperature range between 233 and 313 K.

However, the experimental data provided by previously mentioned authors has been widely used to validate numerical and theoretical models applied in steam injectors and low-pressure

steam turbines applications.

Gyarmathy (2005), on the other hand, studied the characteristics of the nucleation process of high-pressure saturated steam. Gyarmathy's study determined the fog structure and location of the onset of condensation for several nozzles that allowed expansion rates between 10 000 and 200 000 s^{-1}. The inlet stagnation states were between 10 and 110 bar. Gyarmathy (2005) observed that higher expansion rates involved higher supersaturated conditions, producing small but numerous droplets (radius in the order of 6 10^{-8} m).

In respect to experimental investigations on carbon dioxide (CO_2) spontaneous condensation. Bier et al. (1990b) obtained this fluid's Wilson lines by performing a series of vapor expansions in two different nozzles. They realized static pressure measurements along the nozzles' axis; to determine the onset of condensation in a range between carbon dioxide's triple point and 90 % of the fluid's critical pressure.

Paxson (2016) focused on the characterization of the behavior of CO_2 non-equilibrium condensation close to the fluid's critical point. By using optical interferometry techniques and static pressure measurements, he determined the CO_2 density distribution in a de Laval nozzle and the fluid's Wilson curve as well.

Lettieri et al. (2017) performed a series of CO_2 experiments on Paxson's test rig. They documented pressure profiles along their nozzle's axis for a variety of inlet stagnation conditions ranging from 59 to 84 bar. The characterization of CO_2 behavior in those experiments defined inlet conditions free of condensation in supercritical CO_2 compressors. Lettieri et al. (2017) reported that the new inlet conditions could reduce the compressor's shaft power input by 16 %.

The experimental study of spontaneous condensation in other substances such as heavy water and mixtures has been approached by Lamanna (2000), Kim et al. (2004) and Sinha et al. (2009) to mention a few. Lamanna (2000) employed interferometry techniques to visualize the density of condensing flow at total nozzles's inlet conditions of 0.88 bar and temperatures between 282 and 300 K.

Kim et al. (2004) carried out experimental analyses focused on direct measurements of stationary, homogeneous nucleation rates and determined the number of formed droplets from Small-Angle Neutron Scattering (SANS) measurements, the supersaturation ratio at the onset of condensation lied between 43 and 143. However, other techniques such as Small-Angle X-ray Scattering (SAXS) have also been implemented by Sinha et al. (2009) to measure peaks of nucleation rates and to qualitatively determine the growth of small droplets produced under non-equilibrium conditions.

Tab. 2.1 provides formation about the stagnation pressure P_o and temperature T_o at the inlet, the magnitude of the measured mean radius $\bar{r}$ of droplets, and techniques used in the previously mentioned experimental investigations.

Table 2.1 – Experimental researches on condensation in nozzle flows

Author	Fluid	Po (bar)	To (K)	$\bar{r}$ (10^{-8}m)	Technique
Barschdorff (1971)	Steam	0.7839	370-400	0-7	INT [1]
Moore et al. (1973)	Steam	0.2-0.3	340-358	5	NR[2]
Moses & Stein (1978)	Steam	0.4-0.67	366-386	NR	LLS
Bier et al. (1990b)	CO_2	45	300-326	NR	SPM[3]
Lamanna (2000)	NO_2/H_2O	0.88	282-300	1-4	INT
Kim et al. (2004)	D_2O	0.597	288-310	0.4-1.2	SANS
Wyslouzil et al. (2007)	D_2O	0.3-0.6	298-308	0.4-1	SAXS
Gyarmathy (2005)	Steam	10-110	400-640	1-14	LLS
Paxson (2016)	CO_2	58-93	309-312.5	NR	INT
Lettieri et al. (2017)	CO_2	59-84	313-315	NR	SPM

[1] Interferometry.
[2] Not reported value.
[3] Static pressure measurements.

2.2 Overview of theoretical and numerical studies

The current section categorizes the reviewed theoretical and numerical studies into two groups. The first one approaches condensation shocks as discontinuities, and the second one treats non-equilibrium condensation from gas-kinetics involving nucleation and droplet growth theories.

2.2.1 Discontinuities

In the earlier investigations in condensation shocks, Heybey & Reed (1955) discussed the physical aspects of rapid condensation processes, considering a condensation shock as a discontinuity. According to their research, condensation shocks present characteristics of weak detonations due to the exothermic character that establishes a relation concerning flow processes involving chemical reactions, which is not correct.

Years later, Wegener & Mack (1958) discussed in detail the theory of weak detonations for perfect condensing vapor flows in wind tunnels. In their study, a graphical analysis based on the intersections on the Hugoniot and Rayleigh lines included other mathematical possible solutions such as strong detonations and the Chapman-Jouquet state for supersonic condensing flow.

This theory has since been continued by Blythe & Shih (1976), Thompson (1988) and Guha (1994). Blythe & Shih (1976) employed the theory developed by Wegener & Mack (1958) to model the jump conditions for condensation shocks of a mixture composed by a condensing vapor and an inert carrier gas. They assumed a quasi-one-dimensional model and treated the vapor phase of each mixture's component as a perfect gas.

Thompson (1988), on the other hand, presented the theory of discontinuities from a general perspective. He focused on the flow characteristics to achieve normal shock waves and condensation shocks as well.

Guha (1994) presented and unified theory for aerodynamic condensation shock waves in condensing vapor flows with the presence of inert carrier gas. By applying conservation equations, he derived the jump conditions for such discontinuities and defined them as the generalized Rankine-Hugoniot equations for two-phase flow. He also highlighted that those equations could be used in both homogenous and heterogeneous condensation models. And most recently by Korpela (2012), who neglected the exothermic condition in the jump equations for condensation shocks.

It should be stressed that all the previously cited investigations did not considered a non-ideal gas behavior model in order to characterize the phase transition as a discontinuity. Furthermore, no CFD numerical work has addressed such a method in previous times, it is also necessary to highlight that a purely thermodynamic model like the discontinuity approximation is not able to characterize properly the phase transition into liquid due to the kinetic aspects involved in this phenomenon (Wegener; Mack, 1958; Korpela, 2012).

Karagiannis (2020) assessed steam non equilibrium condensation inside resistojet micronozzles for small satelites' propulsion. Karagiannis (2020) evaluated his CFD model with the experimental data provided by Moore et al. (1973) and, then carried out simulations in micronozzles with a depth of 100 mm, for the latest geometries stagnation pressure and temperature at the inlet ranged from 1 up 5 bar and 473 to 673 K, respectively.

2.2.2 Gas-kinetics

2.2.2.1 Theoretical studies

The following paragraphs mention works related to theories involving nucleation, droplet growth laws, and gas-dynamic relaxation processes in homogeneous condensation.

Oswatisch (1942) identified two processes in homogeneous condensation. The first process is associated to nucleation and the second one refers to droplet droplet growth. However, taking into account the classical nucleation and droplet growth theories, Oswatisch (1942) proposed the first mathematical statements to characterize the phase transition process in wind tunnels.

Wegener (1954) presented a review of the earliest investigations in this field. Wegener & Mack (1958) determined the rate production of droplets in supersonic condensing flow and discussed other kinetic aspects involved in spontaneous condensation, such as the characterization of liquid clusters' critical size and droplet growth laws. He mentioned that a purely thermodynamic method could not characterize spontaneous condensation properly due to non-equilibrium conditions involved.

Stepchkov (1960) studied spontaneous condensation of moist air in supersonic wind tunnels. His study approached relevant aspects such as dependence of relative pressure, Mach number, and supersaturation at the onset of condensation. Stepchkov (1960) analyzed the effects of air humidity, concluding that lower air humidity implies higher supersaturation.

Pouring (1965) presented an analytic model for non-equilibrium condensation in moist-air expansions by employing one-dimensional equations. He suggests that the onset of condensation

could be used to test theories of homogeneous nucleation. Blythe & Shih (1976) analyzed the conditions for the supersaturated state by a condensation shock. They also studied the droplet production in the growth region and proposed scaling laws to characterize its structure.

Hill (1966) examined corrections applied to the nucleation theory due to gasification effects and uncertainties associated with cluster surface energy. He concluded that the classical nucleation theory satisfactorily characterized the incidence of condensation in steam without taking into account gasification concepts and surface tension's corrections due to capillarity. Further, Hill's paper presented a mathematical expression to relate the droplet's growth rate during the nucleation process in both steam and moist air expansions.

Droplets' growth models for steam homogeneous condensation have also been presented by Gyarmathy (1962) and Young (1980). Gyarmathy (1962) considered transport phenomena in molecular scales during condensation, proposing a growth rate model termed by the Knudsen number. Young (1980), on the other hand, reviewed and corrected the models proposed by Hill (1966) and Gyarmathy (1962) to achieve accuracy with experimental data of steam and to cover high-pressure ranges. Young (1988) also applied corrections to the nucleation theory due to non-isothermal effects involved.

According to theories to determine the nucleation rate in spontaneous condensation, Feder et al. (1966) reviewed the theory of homogeneous nucleation in metastable vapors and reported a new kinetic treatment. His kinetic treatment assumed the heating of the growing clusters provoked due to the heat released in condensation. Feder's study also discussed unsteady nucleation and gave a simple estimation for the transition to a steady nucleation regime. Bakhtar et al. (2005), on the other hand, applied corrections to the Becker-Döring theory and included other modifications proposed by Kantrowitz (1951) and Courtney (1961). However, Bakhtar et al. (2005) presented a novel model to predict the nucleation rate in steam condensing flows, which has been widely employed in CFD numerical simulations for both low and high pressures expansions.

Other works have focused on the characterization of the relaxation processes involved during homogeneous nucleation and expansions of two-phase flows. Young & Guha (1991) studied the structure of pure substances' two-phase flow and the interaction of the droplets with vapor. They identified three relaxation processes related to the droplet's thermal equilibrium, velocity slip at the interface, and equilibrium of the droplets-vapor system. Guha (1994) employed the relaxation times proposed by Young & Guha (1991) to describe the condensing flow behavior in converging-diverging nozzles.

2.2.2.2 Numerical works

This brief section presents numerical studies of non-equilibrium condensation in steam, carbon dioxide, and other substances.

Dykas (2001) performed numerical calculation for steam condensing flows under low-pressure conditions by employing the IAPWS-IF97 EoS in a 3D and 2D Euler models. He analyzed the effects of both homogeneous and heterogeneous condensation. Dykas (2001) validated his

results with the experimental and the nozzle geometry provided by Barschdorff (1971). He also highlighted that the 2D model is a significant simplification and the high non-ideal behavior of steam in such conditions.

Yang & Shen (2009) evaluated spontaneous condensation of steam in low pressures by employing the virial EoS presented by Young (1988). They used the nozzle geometry of Moore et al. (1973) and revealed flow characteristics at the onset of condensation. Yang & Shen (2009) reported the peak of the nucleation rate with a value of 4.8 10^{21} m^{-3} s^{-1}, a subcooling of 38.31 K at the Wilson point location, and a wetness fraction of 0.06 at the nozzle's outlet.

Fakhari (2010) evaluated the viscous and unsteady effects in homogeneous steam condensation under both low-pressure and high conditions by using the IAPWS-IF97 EoS in a 2D and 3D flow model. He validated the numerical results with the experimental data of Moore et al. (1973). Fakhari (2010) also reported values of the droplet's mean radius that were in the order of 10^{-8} m.

Dykas & Wróblewski (2011) evaluated two models to describe the behavior of steam low-pressures condensation shocks. The first model assumed that the liquid and vapor phases behaved as one fluid. The second one established conservation equations for both-phases and also considered the drag force effects on the droplets. However, both models lied in agreement with the experimental results reported by Barschdorff (1971).

Dykas & Wróblewski (2012) carried out numerical simulations of steam in high and low pressures in a 3D model. Their model consisted of separated conservation equations for each fluid's phase. The numerical results of Dykas & Wróblewski (2012) results for low-pressure conditions had a very good agreement with the experiments performed by Moses & Stein (1978). Conversely, in high pressures, their reported pressure distributions obtained high deviations concerning the experimental measurements provided by Gyarmathy (2005). According to droplets' size, the values obtained by Dykas & Wróblewski (2012) were 2.5 greater than the experimental ones.

Blondel et al. (2015) performed numerical simulations for homogeneous condensation of steam in the nozzle geometries of Barschdorff (1971) and Moore et al. (1973). He implemented a monodispersed model and the polydispersed MoM in quasi-one-dimensional Euler flow. In respect to pressure distributions, the polydispersed model had a better agreement with the experimental values. However, both models predicted the droplets' mean radius, which was in the order of 10^{-8} m. It was also appreciated in Blondel's study that the effects of evaporation were neglected.

Grübel et al. (2014) compared the droplet growth models developed by Gyarmathy (1962) and Young (1980) in an axisymmetric Euler flow model in the nozzle geometry of Moses & Stein (1978). Regarding their predicted pressure profiles, calibration parameters in both droplet growth models allowed the obtention of low deviations with the experimental data, which also occurred with their reported droplet size distribution.

Pandey (2014) employed the improved Peng-Robinson equation with the Strjek-Vera modification (iPRSV) to compute condensation shocks of steam under low-pressure conditions. His work assume mono-dispersion of droplets in a quasi-one-dimensional Euler flow model. The numerical

results of Pandey (2014) presented low deviations in respect to the pressure measurements reported by Barschdorff (1971) and Moore et al. (1973). Further, some of the nucleation rates reported at the onset of condensation were in the range between 10^{17} and 10^{22} m^{-3} s^{-1}

Heinze (2015) carried out simulations for two-phase flows in steam injectors. He focused on the implementation of a one-dimensional numerical model for condensing flows in convergent-divergent nozzles. His model considered the pressure and temperature gradient in the Knudsen layer and also separated conservation equations for the vapor and liquid phases. However, the implemented homogeneous model was unable to predict the pressure profile accurately according to the experimental data provided by Gyarmathy (2005).

Farag (2015) evaluated the effects of turbulence in an axisymmetric model for steam condensation in nozzle flows. Their study employed the droplet growth theory developed by Hill (1966) and revealed some characteristics of the flow behavior. At the onset of nucleation, Farag (2015) achieved nucleation rate values in the magnitude of 10 ^{23} m^{-3} s^{-1} and a Mach number of about 1.2.

Sova et al. (2017) focused on the modelling of steam non-equilibrium condensation by employed the droplet growth models in the papers of Young (1980) and Gyarmathy (1962). The applied correction factors to the surface tension equation, Knudsen numbers, and other parameters in the nucleation rate expression. Those modifications allowed them to achieve low deviations with the experiments of Moore et al. (1973) and Moses & Stein (1978). Their droplets' mean radius distributions showed magnitudes of 0-50 10^{-9} m.

Azzini & Pini (2017) focused on steam non-equilibrium condensation under high pressure conditions. They implemented the MoM in a quasi-one-dimensional Euler flow model. The droplets' size distribution obtained by Azzini & Pini (2017) presented a good agreement with experimental measurements of Gyarmathy (2005). Nevertheless, their predicted pressure distribution had high deviations in respect to the profiles reported by the experimental data under high pressures.

Senguttuvan & Lee (2019) studied the condensation process that occurs in the final stages of low pressure-steam turbines by employing the nozzles geometries of Moore et al. (1973). Senguttuvan & Lee (2019) used an axisymmetric Euler flow model with a mono-dispersed approach. In this paper, the virial coefficient Young (1988) EoS and Hill's droplet growth law were utilized to compute steam properties and to characterize the growth of liquid. Senguttuvan & Lee (2019) observed that by increasing the stagnation temperature at constant pressure at the nozzle's inlet, the condensation shock moved downstream of the nozzle's throat and intensified as the area ratio increased.

In respect to theoretical and numerical studies involving carbon dioxide, it is necessary to mention the works carried out by Bier et al. (1990b), Paxson (2016), Azzini (2019), and Restrepo et al. (2019).

Bier et al. (1990a) analyzed the spontaneous condensation of CO_2- air mixtures (CO_2 mole fractions between 5 and 75%) in convergent-divergent nozzles. For mole fractions ranging between 50 and 75 %, Bier et al. (1990a) observed that the addition of air does not have effects

on the supersaturation at carbon dioxide's Wilson point. In mole fractions lower than 50%, they noticed that the presence of air stimulates the condensation of CO_2. Their paper reported a peak nucleation rate value in the magnitude of 10^{19} cm^3 s^{-1}.

Paxson (2016) evaluated the Span & Wagner (1996) (SW) EoS to predict carbon dioxide's metastable properties. He found high deviations between the predicted densities and those obtained from interferometry measurements close to the fluid's critical point. However, he recommended the use of the SW equation in thermodynamic states far from the fluid's critical condition.

Azzini (2019) carried out a numerical simulation of CO_2 condensation in the nozzle geometry of Lettieri et al. (2017). Azzini's study used the MoM in a quasi-one-dimensional Euler model. Her results presented a good agreement with the experimental data in the isentropic flow expansion; nevertheless, high discrepancies occurred downstream of the onset of condensation.

Brinckman et al. (2019) performed a series of simulations to in order to reproduce the operating conditions of carbon dioxide supercritical compressors, it should be highlighted that in these works interpolation methods of properties based on Span & Wagner (1996) EoS were implemented.

Restrepo et al. (2019) obtained theoretically carbon dioxide's Wilson curve in a range between 85 a 98 of the critical pressure. They employed the SW EoS and the nucleation rate model presented by Bakhtar et al. (2005). Their results had low deviations with the experimental data (Bier et al., 1990b) (Lettieri et al., 2017) in a range between 85 and 91 of the fluid's reduced pressure.

Other authors such as Lamanna (2000), Sidin (2009), and Sinha et al. (2009) investigated spontaneous condensation in other substances. Lamanna (2000) carried out simulations in Laval Nozzles with a mixture of nitrogen and water as a working fluid. She tested different growth, nucleation models, and correlations for surface tension in a quasi-one-dimensional model. Sidin (2009) employed the MoM to evaluate multi-component condensing flows in methanol-propanol mixtures. And Sinha et al. (2009) developed a poly-dispersed steady-state one-dimensional model to examine the growth of liquid phase in heavy water nozzle flows. It

Some of the existing and most recent studies regarding non-equilibrium condensation have been listed by the previous paragraphs. Although, the implementation of an accurate thermodynamic model concerning thermodynamic properties has been problematic in CFD investigations (Dykas, 2001). By consequence, aiming to solve such a problem, some authors have adopted viral formulations and others have implemented interpolations methods from accurate EoS data (Young; Guha, 1991; Dykas, 2001), these facts make the model's operating range limited and as far as the author know there is no a CFD that employs the EoS that the present study uses (Span & Wagner (1996) and Wagner & Pruß (2002) EoS)

Tab. 2.2 summarizes some of the information presented in the previous paragraphs related to inlet conditions, droplet mean radius, nucleation rate J values at the onset of condensation, and EoS.

Table 2.2 – Numerical studies on condensation in nozzle flows

Author	Fluid	Po (bar)	To (K)	$\bar{r}$ (10^{-8}m)	J (m^{-3} s^{-1})	EoS
Bier et al. (1990a)	Air-CO_2	3.14-28.76	239-262	NR[1]	10^{-13}	E. Bender
Lamanna (2000)	N_2O/H_2O	0.867	296.6	25-65	10^{22}	NR
Dykas (2001)	Steam	0.785	373.15-380.55	2-8	10^{22}	IAPWS-IF97
Sinha et al. (2009)	D_2O	0.3, 0.6	298,308	0.2-1	10^{12}	Ideal
Yang & Shen (2009)	Steam	0.25	354.6	NR	4.8 10^{21}	Young (1988)
Sidin (2009)	Ethanol/Propanol	NR	260	5000	NR	Perfect-gas
Fakhari (2010)	Steam	0.2-0.3	350-358	0.005-7	10^{23}	IAPWS-IF97
Dykas & Wróblewski (2011)	Steam	0.7839	380.55, 373.17	1-5	10^{23}	IAPWS-IF97
Dykas & Wróblewski (2012)	Steam	40-108, 0.7839	575-619	0.2-10	NR	IAPWS-IF97
Blondel et al. (2015)	Steam	0.25,0.7839	356-380	0.9-5	10^{24}	IAPWS-IF97
Grübel et al. (2014)	Steam	0.3-0.7	354-377	2-8	NR	NR
Pandey (2014)	Steam	0.25, 0.7839	356-380	8, 40	10^{17}-10^{22}	iPRSV
Heinze (2015)	Steam	0.7839-101	380-662	0-12	10^{20} [2]	IAPWS-IF97
Farag (2015)	Steam	NR	NR	NR	10 ^{23}	Young (1988)
Sova et al. (2017)	Steam	0.25-0.68	358.1-378	0-5	NR	NR
Azzini & Pini (2017)	Steam	101	615.2-638	2-8	NR	NR
Senguttuvan & Lee (2019)	Steam	0.2-0.3	356-380	NR	10 ^{24}	Young (1988)
Azzini (2019)	CO_2	63.9	311.87	NR	10^{17} [2]	NR
Brinckman et al. (2019)	CO_2	58-85	311-315	NR	NR	Span and Wagner (1996)

[1] Not reported value.
[2] $kg^{-1}s^{-1}$.

3 CONCEPTS AND THEORY

3.1 Equations-of-State

The operating conditions of supersonic nozzles differ from ideal gas behavior as condensation occurs under non-equilibrium conditions. The condensation phenomenon takes place somewhere in the metastable vapor region between the spinodal and binodal curves, as displayed in Fig 3.1. Therefore, the EoS must properly access the thermodynamic metastable state.

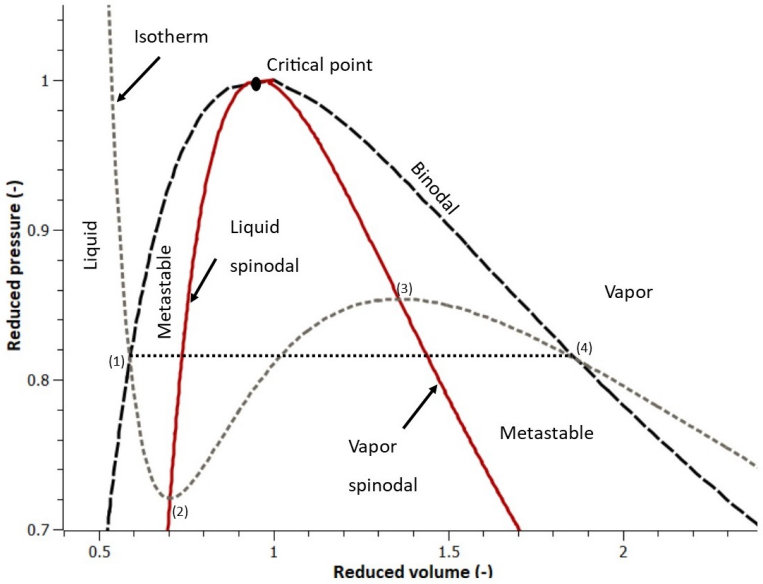

Figure 3.1 – Regions in a reduced P-v diagram.
Font: Pandey (2014) (adapted).

It has been observed in Tab 2.2 that the most of EoS employed for modelling condensing steam flows are the formulation IAPWS-IF97 proposed by the International Association for the Properties of Water and Steam (IAPWS), the correlation presented by Young (1988) and the Peng-Robinson equation with the Stryjek-Vera modification (iPRSV) proposed by Van der Stelt et al. (2012).

The IAPWS-IF97 EoS replaces the older IFC-65 formulation, sets of equations to compute steam properties at specific operating regions composes the IAPWS-IF97 EoS, this fact makes this model appropriate for fast numerical calculations required by the CFD field (Wagner et al., 2000). Nevertheless, it has deviations within 1% in all properties, except close to the critical point in comparison to the IAPWS-95 formulation. Hence, the IAPWS-95 model is quite more accurate than the IAPWS-IF97, as the IAPWS reports. However, both formulations compute steam properties from the triple point up to pressures of 100 MPa.

Besides, Young (1988) presented a virial coefficient EoS specifically for turbomachinery

applications, aiming to guarantying fast and accurate calculations of steam properties in comparison to the IFC-95 equation. However, Yang & Shen (2009), and Senguttuvan & Lee (2019) implemented this model for numerical simulations of non-equilibrium condensation of steam under low-pressure conditions and no implementation for high-pressures features on the reviewed literature.

Also, Pandey (2014) used the iPRSV for modelling steam condensing flows at total inlet pressures between 0.2 and 0.7 bar, and he reports that the iPRSV equation estimates steam properties in the metastable vapor region accurately. However, Van der Stelt et al. (2012), affirm that this EoS has a deviation within 1.5 % in the calculation of the saturation pressure.

Regarding carbon dioxide, on the other hand, the SW EoS predicts with accuracy the fluid properties in the metastable region as reported by Paxson (2016). Thus, it is adequate to be implemented in simulations for non-equilibrium condensation of CO_2.

Consequently, the current study employs the IAPWS-95 and SW EoS; these Helmoltz free energy based equations are available as an opensource thermodynamic library developed by Bell et al. (2014). And the iPRSV EoS, in contrast, arouses interest due to its cubic formulation, which can be implemented from the knowledge of the residual properties and departure function theories.

3.1.1 Helmoltz based EoS

Wagner & Pruß (2002), and Span & Wagner (1996) respectively proposed the IAPWS-95 and SW EoS, who formulated these equations in terms of a fundamental equation explicit in the Helmholtz free energy. According to the departure function theory, for a non-ideal EoS, an ideal and residual part determines any thermodynamic property (Smith et al., 2018). These equations, therefore, fit the residual component of the Helmholtz free energy to experimental data in terms of (Wagner; Pruß, 2002; Span; Wagner, 1996):

- Pressure P, density ρ and temperature T of the single-phase regions.
- Properties of the binodal or saturation curve determined from Maxwell's criteria.
- Specific isochoric c_v and isobaric c_p heat capacities.
- Speed of sound w.
- Specific enthalpy h, internal energy, and the Joule-Thompson coefficient.

$$\frac{\boldsymbol{A}(\rho, T)}{RT} = \phi(\delta, \tau) = \phi^o(\delta, \tau) + \phi^r(\delta, \tau) \tag{3.1}$$

Eq. (3.1) thus represents the structure of the IAPWS-95 and SW EoS, the left hand side term of that expression corresponds to the dimensionless form of the Helmholtz free energy, same as $\phi(\delta, \tau)$. R denotes the specific gas constant, $\phi^o(\delta, \tau)$ and $\phi^r(\delta, \tau)$ respectively determine ideal and residual parts of the dimensionless Helmholtz property.

$$\delta = \frac{\rho}{\rho_c} \tag{3.2}$$

$$\tau = \frac{T_c}{T} \tag{3.3}$$

Eqs. (3.2), and (3.3) define the terms δ and τ in Eq. (3.1), and Tab. 3.1 lists the critical point properties of steam and carbon dioxide including the ρ_c and T_c terms.

Table 3.1 – Critical point properties

Fluid	Pressure P_c (bar)	Density ρ_c (kg/m^3)	Temperature T_c (K)
Steam	220.64	322	647.096
Carbon dioxide	73.773	467.6	304.12

Moreover, the purpose of this section is to present definitions of thermodynamic properties approached from the Helmholtz EoS. Eqs. (3.4), (3.5), and (3.6) respectively determine the enthalpy h, entropy s, and speed of sound w regarding the IAPWS-95 and the SW formulations.

$$\frac{h\left(\delta,\tau\right)}{RT} = 1 + \tau\left(\phi^o_\tau + \phi^r_\tau\right) + \delta\phi^r_\delta \tag{3.4}$$

$$\frac{s\left(\delta,\tau\right)}{R} = \tau\left(\phi^o_\tau + \phi^r_\tau\right) - \phi^o - \phi^r \tag{3.5}$$

$$\frac{w^2\left(\delta,\tau\right)}{RT} = 1 + 2\delta\phi^r_\delta + \delta^2\phi^r_{\delta\delta} - \frac{\left(1 + \delta\phi^r_\delta - \delta\tau\phi^r_{\delta\tau}\right)}{\tau^2\left(\phi^o_{\tau\tau} + \phi^r_{\tau\tau}\right)} \tag{3.6}$$

Here, the subscripts τ, δ, $\delta\delta$, $\tau\tau$, $\delta\tau$ are derivatives from the ideal (ϕ^o) or residual (ϕ^r) form of the dimensionless Helmoltz free energy. Refer to Wagner & Pruß (2002), and Span & Wagner (1996) for detailed information about the calculation of these derivative expressions.

3.1.2 iPRSV EoS

The current study implements the iPRSV EoS for modelling the condensation process of steam under low pressure conditions. This equation is a modification from the original Peng-Robison formulation. By consequence, as any cubic EoS, it can be written as (Smith et al., 2018):

$$P = \frac{RT}{v - b} - \frac{a}{\left(v + \epsilon b\right)\left(v + \varrho b\right)} \tag{3.7}$$

Where, P and v respectively refer to the fluid pressure and molar volume, a is a fluid parameter, Eq. (3.8) determines b, and Eq. (3.9) defines the terms ϵ and ϱ.

$$b = 0.7796\frac{RT_c}{P_c} \tag{3.8}$$

Here, P_c refers to the pressure of the fluid's critical point.

$$\epsilon = \sqrt{2} \quad \varrho = \sqrt{-2}. \tag{3.9}$$

The definition of the term a in Eq. (3.10), approached from the iPRSV equation, evidences the modification made to the original Peng-Robinson EoS (Van der Stelt et al., 2012).

$$a = a_c \chi \tag{3.10}$$

With:

$$a_c = 0.457235 \frac{R^2 T_c^2}{P_c} \tag{3.11}$$

$$\chi = \left[1 + k\left(1 - \sqrt{T_r}\right)\right]^2 \tag{3.12}$$

The coefficient k depends on the acentric factor of the molecule and $T_r = T/T_c$ refers to the reduced temperature of the fluid.

$$\begin{aligned} k = k_0 + k_1\{\sqrt{\left[1.1 - 1.2\left(T_r + 0.25\right)\right]^2 + 0.01} + \\ + 1.1 - 1.2\left(T_r + 0.25\right)\}\sqrt{T_r + 0.2} \end{aligned} \tag{3.13}$$

With:

$$k_0 = 0.37464 + 1.54226\omega - 0.26692\omega^2 \tag{3.14}$$

Here, ω represents the acentric factor of the molecule, and k_1 is a fluid specific parameter that is equal to -0.06635 for steam (Van der Stelt et al., 2012). On the other hand, according to the departure function theory, any thermodynamic property may be written as (Smith et al., 2018):

$$M = M^o + M^r \tag{3.15}$$

Where M represents the molar value of a thermodynamic property; M^r and M^o define residual and ideal gas properties. Consequently, Eqs. (3.16) and (3.17) respectively determine residual enthalpy and entropy valid for any EoS (Smith et al., 2018)

$$\frac{h^r}{RT} = -T \int_0^P \left(\frac{\partial Z}{\partial T}\right)_P \frac{dP}{P} \quad (T \text{ constant}) \tag{3.16}$$

$$\frac{s^r}{R} = -T \int_0^P \left(\frac{\partial Z}{\partial T}\right)_P \frac{dP}{P} - \int_0^P \left(Z - 1\right) \frac{dP}{P} \quad (T \text{ constant}) \tag{3.17}$$

In Eqs. (3.16) and (3.17), the terms h^r and s^r refer residual enthalpy and entropy, Z corresponds to the compressibility factor determined by Eq. (3.18).

$$Z = \frac{Pv}{RT} \tag{3.18}$$

Reynolds & Colonna (2018) give explicit expressions for the iPRSV's residual enthalpy and entropy in Eqs.(3.19), and (3.19).

$$h^r = RT(Z - 1) + \frac{T\frac{da}{dT} - a}{2\sqrt{2}b} \ln\left[\frac{Z + \left(1 + \sqrt{2}\right)\Psi}{Z + \left(1 - \sqrt{2}\right)\Psi}\right] \tag{3.19}$$

$$s^r = R\ln\left(Z - \Psi\right) + \frac{\frac{da}{dT}}{2\sqrt{2}b} \ln\left[\frac{Z + \left(1 + \sqrt{2}\right)\Psi}{Z + \left(1 - \sqrt{2}\right)\Psi}\right] \tag{3.20}$$

Eqs. (3.21) and (3.22) respectively define the terms Ψ and da/dT in Eqs. (3.19) and (3.20).

$$\Psi = \frac{bP}{RT} \tag{3.21}$$

$$\frac{da}{dT} = 2a_c\left(1+\tau_1 k\right)\left(\tau_1\frac{dk}{dT} - \frac{k}{2\tau_2}\right) \tag{3.22}$$

Here, the coefficients τ_1 and τ_2 are determined by Eq. (3.23), and Eq. (3.24) computes the term dk/dT.

$$\begin{aligned}\tau_1 &= 1-\sqrt{T_r}\\ \tau_2 &= \sqrt{T_c T}\end{aligned} \tag{3.23}$$

$$\frac{dk}{dT} = \frac{k_1\left(T_x+T_y\right)}{T_c}\left[\frac{1}{2T_z} - \frac{T_z\left(\Psi-1\right)}{T_y}\right] \tag{3.24}$$

Where:

$$\begin{aligned}T_x &= 1.1 - 1.2\left(T_r+0.25\right)\\ T_y &= \sqrt{T_x^2+0.01}\\ T_z &= \sqrt{T_r+0.2}\end{aligned} \tag{3.25}$$

Eqs. (3.26) and (3.27) define the actual values of the enthalpy h and entropy s according to Eq. (3.15) and iPRSV's residual properties determined from Eqs. (3.19) and (3.20).

$$h = h^o + h^r = \int_{T_{\text{ref}}}^{T} c_p^o\, dT + h^r \tag{3.26}$$

$$s = s^o + s^r = \int_{T_{\text{ref}}}^{T} c_p^o\frac{dT}{T} - R\ln\left(\frac{P}{P_{\text{ref}}}\right) + s^r \tag{3.27}$$

Here, c_p^o represents the ideal behavior of the isobaric heat capacity and it is calculated from Eq. (3.28). The current study assumes 298 K and 1 bar as the reference temperature T_{ref} and pressure P_{ref} for steam calculations.

$$c_p^o = \mathrm{C}_1 + \mathrm{C}_2 T + \mathrm{C}_3 T^2 + \mathrm{C}_4 T^3 \tag{3.28}$$

Tab. 3.2 lists the value of the coefficients C_1, C_2, C_3 C_4 in Eq. (3.28). They have been adopted from Elliott & Lira (2012).

Table 3.2 – Isobaric heat capacity coefficients for steam.

Coefficient	Value
C_1	32.24
C_2	0.001924
C_3	1.055e-05
C_4	-3.596e-09

Furthermore, the calculation of the speed of sound is a relevant topic for modelling

compressible flow; Eq. (3.29) determines its classical definition (Anderson, 2003).

$$w = \sqrt{\left(\frac{\partial P}{\partial \rho}\right)_s} \tag{3.29}$$

However, Eq. (3.29) carries difficulties to obtain the derivative term in parentheses from a non-ideal EoS approach. Alternatively, Pratt (2001) and, Reynolds & Colonna (2018) present an alternative expression for computing the speed of sound in Eq. (3.30).

$$w = v\sqrt{-\frac{c_p}{c_v}\left(\frac{\partial P}{\partial v}\right)_T} \tag{3.30}$$

Eq. (3.31) defines the term $(\partial P/\partial v)_T$ taking into account the formulation of the iPRSV EoS in Eq. (3.7). Reynolds & Colonna (2018), on the other hand, present expressions to obtain the actual values of the isobaric c_p and isochoric c_v heat capacities in derived from the iPRSV equation. Like any other thermodynamic property, the calculation of c_p and c_v capacities requires knowledge of their ideal and residual contributions and derivatives from the EoS's formulation. Therefore, Annex B.1 reports these mathematical expressions.

$$\left(\frac{\partial P}{\partial v}\right)_T = -\frac{RT}{(v-b)^2} + \frac{2a\,(v+b)}{\left(v^2+2bv-b^2\right)^2} \tag{3.31}$$

Another important aspect for modelling phase-change in nozzle flows is the estimation of the saturation curve. In contrast to the Helmholtz based EoS, the implemented iPRSV uses the iso-fugacity condition (between the vapor and liquid phases) instead of Maxwell's criteria, to establish equilibrium between vapor and liquid phases.

$$\ln \varnothing_\pi = \int_0^P (Z_\pi - 1)\,\frac{dP}{P} \quad T \text{ constant} \tag{3.32}$$

Eq. (3.32) corresponds to the definition of the fugacity coefficient $\varnothing$ valid for any EoS, which it's formulation is explicit in the volume (Smith et al., 2018). The subscript π denotes the fluid's phase and Eq. (3.33) defines the fugacity coefficient in term of the pressure and fugacity f.

$$\varnothing_\pi = \frac{f_\pi}{P} \tag{3.33}$$

Reynolds & Colonna (2018) give Eq. (3.34) to estimate the phase's fugacity according to the iPRSV EoS. However, if a fluid's thermodynamic state satisfies Eqs. (3.35) and (3.34), the highest and lowest specific volumes belong to the vapor and liquid saturation curves.

$$\ln\left(\frac{f_\pi}{P}\right) = Z_\pi - 1 - \ln\left(Z_\pi - \Psi\right) - \left(\frac{a}{2\sqrt{2}bRT}\right)\ln\left(\frac{Z_\pi + \left(1+\sqrt{2}\right)\Psi}{Z_\pi + \left(1-\sqrt{2}\right)\Psi}\right) \tag{3.34}$$

$$f_l = f_v \tag{3.35}$$

Eq. (3.35) represents the iso-fugacity condition, the subscripts v and l respectively denote vapor and liquid phase.

3.2 Compressible flow behavior

3.2.1 Mach number and governing equations

The ratio between the local flow speed u and the local speed of sound defines the Mach number Ma in Eq. (3.36) (Thompson, 1988).

$$Ma = \frac{u}{w} \tag{3.36}$$

Subsonic flows up to $Ma = 0.3$ can be treated as incompressible. Therefore, corrections applied to the incompressibility theory characterize compressible flows up to $Ma = 0.75$. In supersonic flows $Ma > 1$, phenomena such as oblique, normal, and condensation shock waves occur. (Thompson, 1988). However, in nozzle flows, there is a transition from subsonic to supersonic speeds due to the flow expansion in the convergent and divergent sections of the nozzle.

Compressible flow can be treated from different levels of difficulty due to its complex nature (Thompson, 1988). Hence, approximations to a quasi-one-dimensional flow are sufficient to describe the flow behavior in rocket engines, wind tunnels, and de Laval nozzles as Anderson (2003) reports. Quasi-one-dimensional models assume an averaged value of the velocity component, and all properties are uniform in a cross-section of the flow. By consequence, changes in the cross-sectional area modify the flow properties.

Consider a de Laval nozzle sketched in Fig. 3.2, as the flow moves downstream in the nozzle axis x, the cross-sectional area of the duct varies $A = A(x)$; this implies that $P = P(x)$, $\rho = \rho(x)$, and the steady-state flow assumption in a quasi-one-dimensional model yields that $u = u(x)$ (Anderson, 2003).

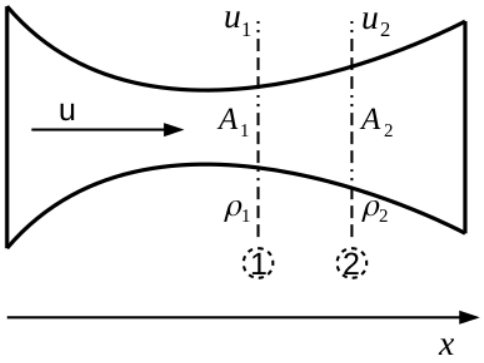

Figure 3.2 – Finite control volume for quasi-one-dimensional flow
Font: Author.

Fig. 3.2 also displays a control volume with different cross-sectional areas delimited by points 1 and 2. Eqs. (3.37 - 3.39) determine the algebraic form of the conservations equations for compressible flow applied to the mentioned control volume (Anderson, 2003).

$$\rho_1 u_1 A_1 = \rho_2 u_2 A_2 \tag{3.37}$$

$$\left(P_1 + \rho_1 u_1^2\right) A_1 + \int_{A_1}^{A_2} P dA = \left(P_2 + \rho_1 u_2^2\right) A_2 \tag{3.38}$$

$$h_1 + \frac{1}{2}u_1^2 = h_2 + \frac{1}{2}u_2^2 \tag{3.39}$$

$$s_2 \geqslant s_1 \tag{3.40}$$

Eqs. (3.37), (3.38) and (3.39) respectively define the mass, momentum and energy conservation equations. Refer to Anderson (2003) for detailed information about the mathematical procedure for their derivation. As observed in Eq. (3.38), the momentum equation is not rigorously an algebraic equation due to the integral term, which refers to the pressure force on the sides of the control surface displayed in Fig. 3.2 (Anderson, 2003).

Eq. (3.40) determines the restriction of the second law of thermodynamics applied to the conservation equations for compressible flow. Where, $s_2 = s_1$ is satisfied by an isentropic expansion. If a normal or condensation shock occurs, the condition $s_2 > s_1$ must be satisfied.

On the other hand, the stagnation or total properties are obtained from a hypothetical steady isentropic deceleration to $u = 0$ (Thompson, 1988). These properties denoted by the subscript o serve as a reference state to characterize the flow behavior in converging -diverging nozzles. They remain constant during an isentropic expansion and vary with entropy generation. Consequently, Eqs. (3.41) and (3.42), respectively define the stagnation enthalpy h_o and entropy s_o.

$$h_o = h_1 + \frac{1}{2}u_1^2 = h_2 + \frac{1}{2}u_2^2 \tag{3.41}$$

$$s_o = s_1 = s_2. \tag{3.42}$$

Furthermore, for steady inviscid flow the stagnation enthalpy becomes (Anderson, 2003):

$$h_o = h + \frac{1}{2}u^2 = \text{constant} \tag{3.43}$$

3.2.2 Area-velocity relation

The area-velocity relation defined by Eq. (3.44) characterizes the flow behavior as a function of the cross-sectional area and Mach number. Refer to annex B.2 for detailed information about the mathematical procedure for its derivation.

$$\frac{dA}{A} = \left(Ma^2 - 1\right)\frac{du}{u} \tag{3.44}$$

Subsonic flow:

For subsonic flow, $0 < Ma < 1$. The right-hand side of Eq. (3.44) remains negative; whereas, the term dA/A is positive and vice versa. An increase is associated with a decrease in velocity, and negative variations of dA/A increase the flow velocity du/u (Anderson, 2003). In terms of

pressure, diverging channels $dA/A > 0$ are related to drops in pressure $dP < 0$, and converging channels leads to $dP > 0$ (Thompson, 1988).

Tab. 3.3 presents the subsonic flow behavior in converging diverging channels and also includes information about temperature variation dT.

Table 3.3 – Subsonic flow behavior, $0 < Ma < 1$.

Type of Channel	Velocity	dP	dT	dA/A
Converging	Increases	< 0	< 0	< 0
Diverging	Decreases	> 0	> 0	> 0

Supersonic flow:

For supersonic flow, $Ma > 1$. An increase in area dA/A implies an increase in velocity and vice versa (Anderson, 2003). Diverging channels $dA > 0$ are linked to drops in pressure $dP < 0$ and converging channels implies that $dP > 0$ (Thompson, 1988).

Tab. 3.4 table summarizes the previous information and also reports temperature variations depending on the type of channel.

Table 3.4 – Supersonic flow behavior, $Ma > 1$.

Type of Channel	Velocity	dP	dT	dA/A
Converging	Decreases	> 0	> 0	< 0
Diverging	Increases	< 0	< 0	> 0

Sonic condition:

For the sonic condition, $M = 1$. The term $dA/A = 0$ corresponds to a mathematical maximum or minimum according to the area distribution (Anderson, 2003).

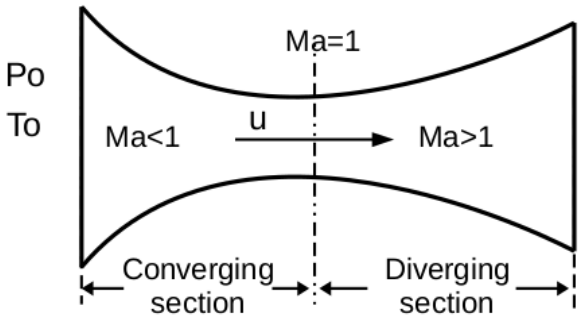

Figure 3.3 – Flow in a convergent-divergent nozzle
Font: Anderson (2003) (adapted).

Consequently, the area-velocity equation characterizes the flow behavior in a converging -diverging nozzle sketched in Fig. 3.3. As the flow expands in the nozzle's convergent section,

it moves under subsonic conditions, it accelerates and decreases the pressure due to $dA/A < 0$. The flow attains the sonic state in the throat where $dA/A = 0$. In the nozzle's divergent section, the flow achieves the supersonic condition, it maintains increasing its velocity and dropping the pressure due to positive changes in the area distribution ($dA > 0$) until a condensation or normal shock wave occur.

It should be stressed that the nozzle's mass flow rate must guarantee the sonic state in the throat. This condition is also known as choked flow. If it is not satisfied, the fluid can not achieve the supersonic state. (Anderson, 2003).

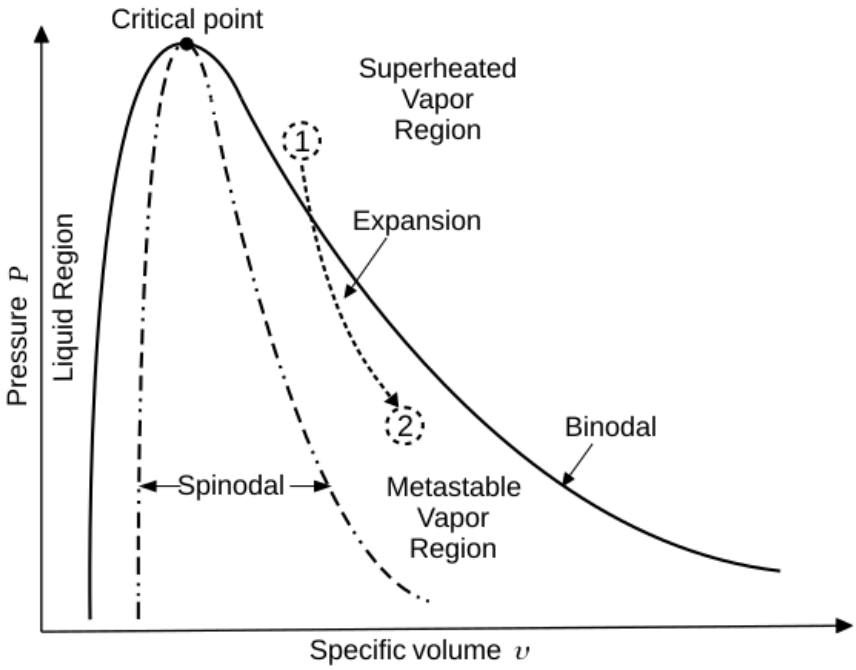

Figure 3.4 – Sketch of a gas expansion in supersonic nozzles.
Font: Pandey (2014) (adapted).

Fig. 3.4 illustrates a nozzle flow expansion in a P-v diagram; the flow departs from the thermodynamic state 1. To lead to condensation, it must attain the condition represented by point 2 in the metastable region between the vapor binodal and spinodal curves. This state is known as the Wilson point and it is reached under supersonic conditions in the nozzle's divergent section. Downstream of the Wilson state, the liquid-phase forms. However, the localization of this point involves thermodynamic and gas-kinetic aspects discussed in section 3.4.

3.3 Detonation-Deflagration Theory

The Detonation-Deflagration Theory (DDT) approaches combustion processes to establish a relation between the properties of the reactants upstream and products downstream of a combustion shock wave (Turns, 2012). The ignition of premixed gases thus causes a propagating wave at subsonic or supersonic speed. Supersonic and subsonic combustion waves are respectively known as detonations and deflagrations (Kuo, 2005). As discussed, the current theory is based

on and mostly applied to combustion models. Nevertheless, it also characterizes phase change phenomena such as adiabatic evaporating waves (Simões-Moreira J. R., 1994; Simões-Moreira; Shepherd, 1999) and condensation processes in high speed nozzle flows (Thompson, 1988).

From the gas-dynamic viewpoint, "A shock wave is a relatively thin region of rapid state variation across which there is a flow of matter" (Thompson, 1988). Hence, condensation shocks become discontinuities in space, because the phase transition into liquid takes place in a very thin region.

In terms of normal shock waves, upstream and downstream properties of condensation shocks are similar; however, the downstream velocity in condensation shocks is always supersonic, whereas in normal shock waves it is subsonic (Wegener; Mack, 1958).

Fig. 3.5 provides a representation of the condensation process in a supersonic nozzle in concordance with the DDT. Point 1 represents the Wilson point that corresponds to the state upstream of the condensation shock. Point 2 represents the two-phase flow conditions downstream of the discontinuity. The static pressure decreases considerably until the single-phase flow reaches point 1. The condensation then makes the pressure increase from 1 to 2. In turn, the two-phase flow expands isentropically, and the static pressure drops between location 2 and the nozzle outlet (Wegener; Mack, 1958).

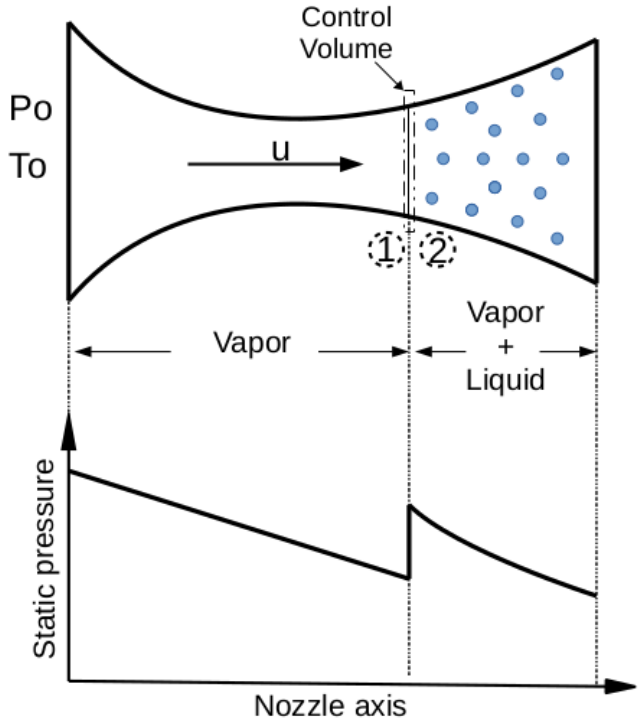

Figure 3.5 – Sketch of a condensation shock in a supersonic nozzle
Font: Author.

It has been also assumed that the wet expansion is in thermodynamic equilibrium (Wegener; Mack, 1958). However, this DDT approach is not able to locate the Wilson point due to kinetic features involved on reaching this purpose (Korpela, 2012). If the localization of the onset of

condensation implies that the flow crosses the spinodal curve instead of the Wilson point, it carries inaccuracies due to the Wilson point location from a thermodynamic perspective. In case of steam, the Wilson state is located close to the binodal curve, in a vapor quality of 0.96 as Korpela (2012) reports.

$$\rho_1 u_1 = \rho_2 u_2 \tag{3.45}$$

$$P_1 + \rho_1 u_1^2 = P_2 + \rho_1 u_2^2 \tag{3.46}$$

$$q + h_1 + \frac{1}{2}u_1^2 = h_2 + \frac{1}{2}u_2^2 \tag{3.47}$$

$$s_2 > s_1 \tag{3.48}$$

Eqs. (3.45), (3.46) and (3.47) determine the jump conditions from the vapor metastable condition 1 to the two-phase equilibrium state 2 in Fig. 3.5, assuming that the flow condenses spontaneously in a thin region where the area variation is negligible $A_1 = A_2$ (Korpela, 2012).

Eqs. (3.45), (3.46), and (3.47) respectively define the mass, momentum and energy conservation equations across a condensation shock. The term q refers to heat added or subtracted per unit mass. Heybey & Reed (1955), Wegener & Mack (1958), Blythe & Shih (1976) and Thompson (1988) considered that q has positive values due to heat released in condensation. Other authors such as Guha (1994) and Korpela (2012) assumed that q equals zero. In fact, there is a heat exchange between the liquid and vapor phases, but it does not occur in respect to the flow surroundings such as the nozzle walls. Therefore, the current study neglects the value of q, taking into account the control volume sketched by Fig. 3.5.

Eq. (3.48), on the other hand, corresponds to the second law of thermodynamics applied to the conservation equations, which implies an increase of entropy between the downstream and upstream states due to condensation.

As the downstream state of the shock is in equilibrium, the properties of the two-phase mixture can be expressed in terms of vapor quality and equilibrium properties of vapor and liquid:

$$\frac{1}{\rho_2} = \frac{X}{\rho_v} + \frac{1-X}{\rho_l} \tag{3.49}$$

$$h_2 = X h_v + (1-X) h_l \tag{3.50}$$

$$s_2 = X s_v + (1-X) s_l \tag{3.51}$$

Eqs. (3.3), (3.50) and (3.51) determine the density ρ_2, enthalpy h_2, and entropy s_2 of the two-phase flow downstream of the shock. The term X denotes vapor quality.

When the upstream state of the shock is known, Eqs. (3.45-3.47) have multiple solutions;

thus, the DDT analyzes them based on the intersections between the Rayleigh and Hugoniot curves. The following section describes these curves' calculation.

3.3.1 Rayleigh and Hugoniot curves

The Rayleigh and Hugoniot equations emerge from the combination of conservation requirements determined in Eqs. (3.45), (3.46) (3.47). These curves have great importance because they allow a phenomenon's graphical analysis in a pressure-specific volume diagram. They establish relations between the upstream and downstream states of a gas-dynamic discontinuity.

The mass flux **J** across a discontinuity such as a condensation shock can be expressed as:

$$\mathbf{J} = \rho u \tag{3.52}$$

Applying Eq. (3.52) to Eq. (3.46), we obtain:

$$\mathbf{J}_1 = \mathbf{J}_2 = \mathbf{J} \tag{3.53}$$

Substituting Eq. (3.53) into Eq. (3.46) yields:

$$P_1 + \frac{\mathbf{J}^2}{\rho_1} = P_2 + \frac{\mathbf{J}^2}{\rho_2} \tag{3.54}$$

Rearranging Eq. (3.54) leads to:

$$\mathbf{J}^2 = -\frac{P_2 - P_1}{1/\rho_2 - 1/\rho_1} \tag{3.55}$$

Eq. (3.55) defines the Rayleigh line, that has a negative slope since the mass flux is positive (Kuo, 2005). Therefore, the Rayleigh curve is a straight line that satisfies the momentum and the mass conservation requirements. It is worth mentioning that the square of the mass flux is proportional to Rayleigh's slopes. Consequently, as the mass flow rate increases, the Rayleigh's slope also increases.

The momentum relation in Eq. (3.46), on the other hand, can be written as:

$$P_1 - P_2 = \rho_2 u_2^2 - \rho_1 u_1^2 \tag{3.56}$$

Extracting the term **J** from the right-hand-side of Eq. (3.46), we obtain:

$$P_1 - P_2 = \mathbf{J}\,(u_2 - u_1) \tag{3.57}$$

Multiplying Eq. (3.57) by $(u_1 + u_2)/\mathbf{J}$, yields:

$$u_2^2 - u_1^2 = (P_1 - P_2)\left(\frac{1}{\rho_1} + \frac{1}{\rho_2}\right) \tag{3.58}$$

The relation beetween the enthalpies from the energy conservation Eq. (3.47) may be written as:

$$h_1 - h_2 = \frac{1}{2}(u_2^2 - u_1^2) \tag{3.59}$$

Substituting Eq. (3.58) into Eq. (3.59) leads to the Hugoniot expression Eq. (3.60)(Kuo, 2005).

$$h_1 - h_2 = \frac{1}{2}(P_1 - P_2)\left(\frac{1}{\rho_1} + \frac{1}{\rho_2}\right) \tag{3.60}$$

For phase-change into liquid, Eqs. (3.50) and (3.3) define the enthalpy h_2 and density ρ_2 in Eqs. (3.60) and (3.55) .

3.3.2 Condensation as a weak detonation

The following analysis outlines how the DDT establishes a relation between condensation shocks and those chemical processes in which reactions occur across sharply defined fronts (in this research the exothermic character has been neglected). The flow upstream of the shock respectively represent the unburnt gas and, the vapor and droplets in the downstream state become the burnt gas; the shock itself is represented as a stationary detonation (Wegener; Mack, 1958).

It follows that Fig. 3.6 displays several Rayleigh and Hugoniot curves for an upstream or initial state represented by point 1. Consequently, intersections on these lines are categorized in the following regions:

- Deflagrations: points F1, F2, CJ_F
- Detonations: points D1, D2, CJ_D
- Impossible solutions: points A and B.

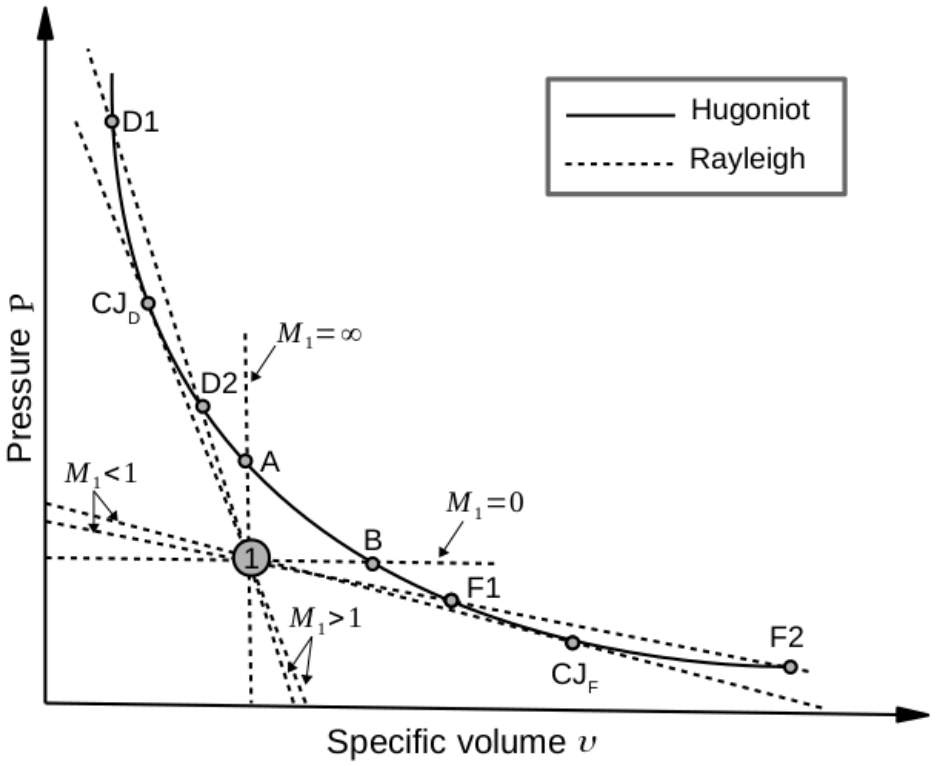

Figure 3.6 – Rayleigh and Hugoniot curves
Font: Wegener & Mack (1958) (adapted).

In the deflagration region, the upstream state is subsonic and has three possible solutions for the final or downstream state represented by F1, F2, and CJ_F in Fig. 3.6.

For a Rayleigh line, which is tangent to the Hugoniot curve in this region, the downstream state corresponds to point CJ_F. The CJ_F state is known as the lower Chapman-Jouguet point and represents the maximum state of entropy (Kuo, 2005). It is worth mentioning that the flow conditions in the lower Chapman-Jouguet state are sonic in respect to the shock wave front (Thompson, 1988).

Therefore other Rayleigh lines intersect the Hugoniot curve on points represented by F1 and F2, which are respectively known as weak and strong deflagrations. The flow velocity in weak deflagrations is subsonic, whereas in strong deflagrations, it is supersonic (Wegener; Mack, 1958).

However, deflagrations are unimportant to the current work because they occur when the initial state is subsonic, whereas, in condensation shocks, it is supersonic (Wegener; Mack, 1958). They characterize other phase-change phenomena such as evaporating waves (Simões-Moreira J. R., 1994; Simões-Moreira; Shepherd, 1999).

Tab. 3.5 summarizes the flow conditions in the upstream and downstream states according to the information provided by the previous paragraphs.

Table 3.5 – Upstream and downstream flow conditions for deflagrations.

Condition	Upstream state (1)	Downstream state (2)
Lower Chapman-Jouguet	$0 < Ma_1 < 1$	$Ma_2 = 1$
Strong deflagration	$0 < Ma_1 < 1$	$Ma_2 > 1$
weak deflagration	$0 < Ma_1 < 1$	$Ma_2 < 1$

Similarly to deflagrations, the detonation region presents three possible solutions for a final state represented by points D1, D2, and CJ_D in Fig. 3.6. It should be mentioned that the initial state is supersonic in this region.

The CJ_D is known as the upper Chapman-Jouguet point. It is the state of minimum entropy, and the flow conditions are similar in comparison to the lower Chapman-Jouguet state (Kuo, 2005).

The points D1 and D2, on the other hand, represent strong and weak detonations. The flow conditions in strong detonations are subsonic; they, thus, represent the solution for two-phase normal shock waves (Wegener; Mack, 1958). Conversely in weak detonations, the flow velocity is supersonic; by consequence, they establish the solution for condensation shocks as Wegener & Mack (1958) report.

Tab. 3.6 details the Mach number behavior in the upstream and downstream states for detonations.

Table 3.6 – Upstream and downstream flow conditions for detonations

Condition	Upstream state (1)	Downstream state (2)
Upper Chapman-Jouguet	$Ma_1 > 1$	$Ma_2 = 1$
Strong detonation	$Ma_1 > 1$	$Ma_1 < 1$
Weak detonation	$Ma_1 > 1$	$Ma_1 > 1$

Points A and B are impossible conditions due to the flow velocity in the initial state, where $Ma_1 = \infty$ or $Ma_1 = 0$. However, there is no solution in the zone between these locations, because any positive slope on the Rayleigh line implies an increase of pressure and specific volume at the same time, an ocurrence which is not physically possible.

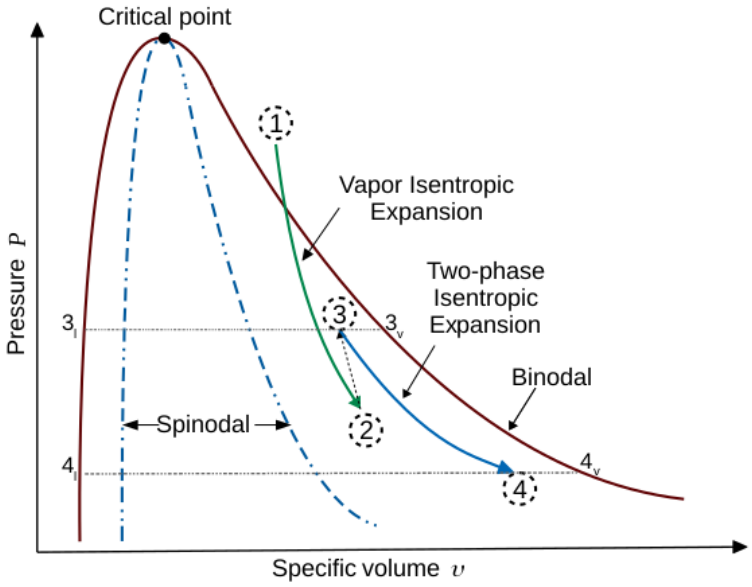

(a)

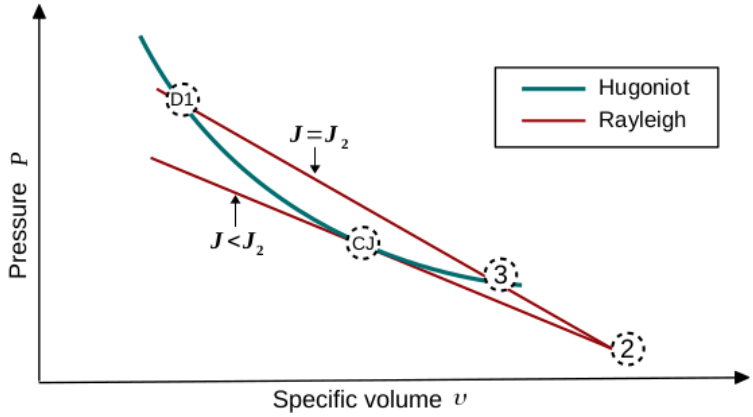

(b)

Figure 3.7 – (a) Expansion with condensation in nozzle flows, (b) Solutions for a condensation shock.

Font: Author.

Finally, Fig. 3.7 displays the processes in nozzle flows approached from DDT. It occurs in

three steps, as observed in a P-v diagram presented by this figure:

- Single-phase isentropic expansion (points 1 and 2)
- Compression due to the condensation shock (points 2 and 3)
- Wet and isentropic expansion under equilibrium (points 3 and 4)(Wegener; Mack, 1958).

Fig. 3.7b displays the possible solutions for the Wilson state (point 2). As mentioned, the downstream condition of the shock is a weak detonation (point 3), because the mass flux is equal to that of the upstream state $\mathbf{J} = \mathbf{J}_2$. However, the mass flux of the upper Chapman-Jouguet $\mathbf{J}_{\mathrm{CJ}}$ point is generally lower than $\mathbf{J}_2$, which means that it does not satisfy the mass conservation requirement. Conversely, in some cases, the mass flux of both upper Chapman-Jouguet and Wilson states may be equal. Consequently, only for this condition $\mathbf{J}_{\mathrm{CJ}} = \mathbf{J}_2$, the Chapman-Jouguet point state may also represent the solution for a condensation shock.

3.4 Homogeneous nucleation

The gas-dynamic discontinuity approach for condensation shocks poorly provides information about the molecular and kinetic aspects that lead to condensation, and also the assumption of a thin region where the droplets form is not always suitable due to the thickness of the condensation shock reported by the experimental measurements. Hence, thermodynamic- kinetic models involving concepts from the Classical Nucleation Theory (CNT) and Droplet Growth Theory (DGT) define and describe condensation processes involving homogeneous nucleation.

These models establish relations from macroscopic properties to determine microscopic ones such as the radius of the liquid embryos (Heinze, 2015). As stated, the flow does not condense immediately it crosses the saturation curve; instead, the condensation delays due to the molecular fluctuations within the vapor that causes liquid clusters to agglomerate and collapse (Lamanna, 2000). The flow then continues expanding in the mestastable region, thus, becoming supersaturated. Undercooled or subcooled are terms that also define this non-equilibrium state (Korpela, 2012).

The single-phase flow consequently becomes sufficiently supersaturated so as to break a critical energy barrier ΔG^*, and the formation of clusters occurs. This state is the previously mentioned Wilson point, downstream of this location, new droplets form and grow; because of the heat and mass transfer between the vapor and droplets, the two-phase flow searches the way back to equilibrium (Lamanna, 2000). The droplets keep growing, and new ones stop forming while the two-phase mixture continues expanding close to equilibrium conditions (Korpela, 2012).

To make it clear. Fig. 3.8 illustrates the mentioned processes in a sketched de Laval nozzle:

- Isentropic expansion, between points 1 and 3.
- Condensation shock or rapid condensation region, between points 3 and 4.
- Two-phase expansion, between points 4 and 5.

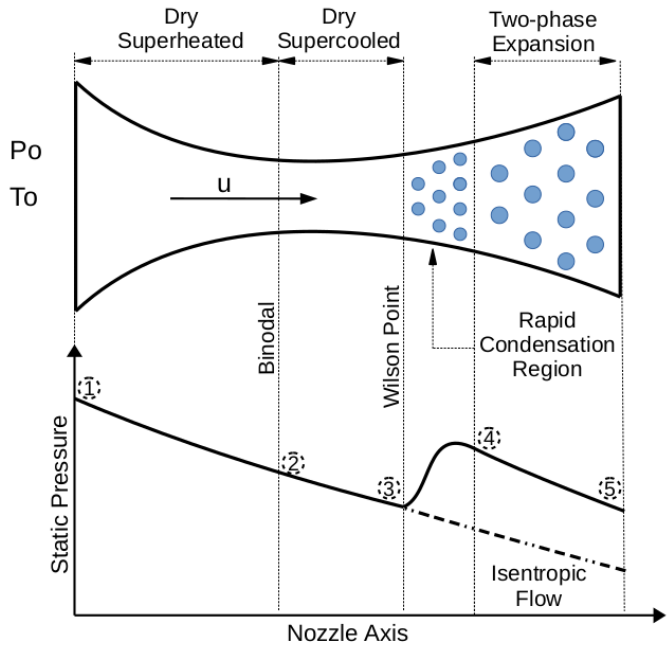

Figure 3.8 – Sketch of homogeneous condensation in a Laval nozzle
Font: Pandey (2014)(adapted).

The vapor departs from the total stagnation conditions at the inlet and attains the saturation curve at location 2. From points 2-3, it then becomes sub-cooled and reaches the Wilson state at point 3. The flow pressure and temperature decrease due to the expansion effects explained by the area-velocity equation for subsonic and supersonic flow. It is also important to highlight that at the Wilson point, the nucleation rate achieves its maximum value (Bakhtar et al., 2005). Therefore, section 3.4.2 discusses topics related to nucleation theory.

The region between points 3 and 4 denotes the rapid condensation or condensation shock region, where the formation of droplets takes place due to mass and heat transfer processes between the liquid and vapor phases. This process makes the flow pressure and temperature increase; however, the flow speed is reduced but the supersonic conditions is maintained.

From points 4 to 5, the two-phase mixture expands close to the equilibrium. Further, the two-phase flow must obey the compressible behavior describe by section 3.44. By consequence, the flow accelerates, and both temperature and pressure decrease. It should be stressed that during this process, droplet growth laws makes droplets increase their size, and no formation of new ones occurs.

3.4.1 Droplet formation mechanism

Yellott (1933) characterizes supersaturation S as the ratio between the pressure of the flow and the saturation pressure at the local vapor temperature. Other authors such as Pandey (2014) define this term as "the inability of fluids to condense in the metastable region". However, the supersaturation ratio and the amount of subcooling ΔT are indicators that determine how far the flow conditions are from the saturated equilibrium. Supersaturation establishes a relation in

respect to the pressure and the subcooling to the temperature.

$$S = \frac{P_v}{P_{\text{sat}}(T_v)} \tag{3.61}$$

$$\Delta T = T_{\text{sat}}(P_v) - T_v \tag{3.62}$$

Eqs. (3.61) and (3.62) respectively define the supersaturation ratio and the amount of subcooling, where the subscript "sat" denotes the saturation state.

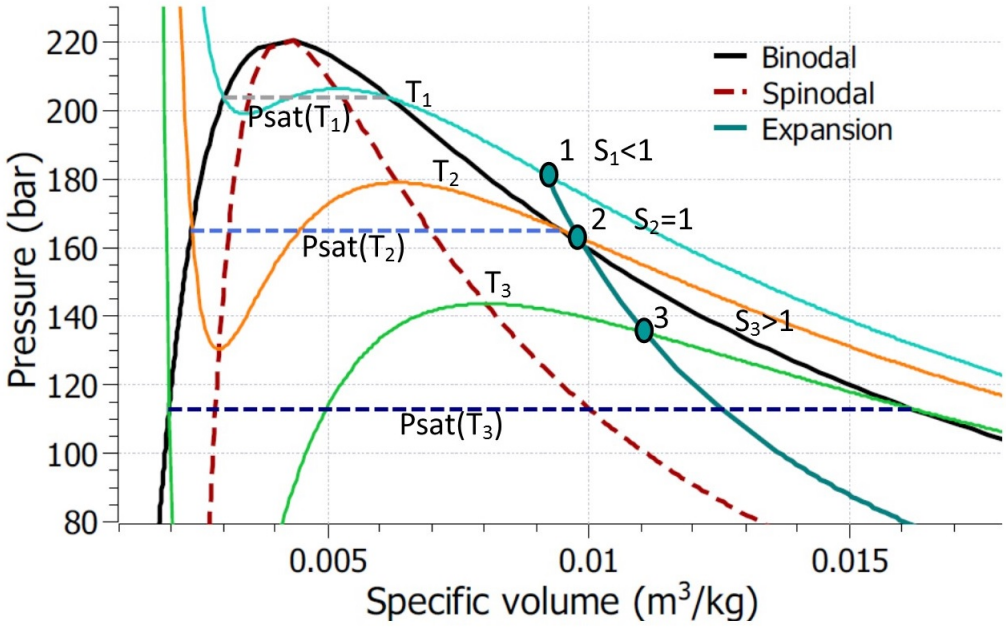

Figure 3.9 – Schematic representation of vapor expansion and the supersaturation ratio.
Font: Author.

The supersaturation ratio also provides information about the flow characteristics. Fig. 3.9 displays an isentropic expansion and the behavior of the supersaturation ratio:

- At the departure point 1, the pressure of the vapor is lower than the saturation pressure; hence, for the superheated vapor region, the supersaturation ratio has values lower than 1.
- At point 2, the flow is the saturation curve, where the supersaturation ratio is equal to 1.
- At point 3, we observe that the pressure of the vapor is higher than the local saturation pressure; thus, for the metastable region, $S > 1$

Similarly, positive and negative values of subcooling respectively determine that the flow is in the metastable and superheated vapor region, and zero values of ΔT mean that it is in the saturation line.

Tab. 3.7 summarizes the values of the subcooling and the supersaturation ratio according to the vapor region.

Table 3.7 – Subcooling and Supersaturation ratio behavior.

Vapor region	Subcooling ΔT (K)	Supersaturation ratio S (-)
Superheated	< 0	$0 < S < 1$
Saturation	$= 0$	$= 1$
Metastable	> 0	> 1

Although, upstream of the Wilson point, where the vapor expands isentropically; either the subcooling or the supersaturation ratio characterizes flow conditions, because the isentropic condition links the pressure and temperature to make them dependent properties. Conversely, downstream of the Wilson point, pressure and temperature become independent due to the effects of the droplet growth that lead to entropy generation; thus, both the supersaturation ratio and the subcooling are required to determine how far the two-phase flow is from saturated equilibrium.

The amount of subcooling and the supersaturation ratio influence processes such as the nucleation rate, the droplet formation mechanisms, and droplet growth laws. Wegener (1954) describes the Gibbs' free energy variation ΔG in the mechanism of droplet formation. It consists of five steps that assume that the clusters have a spherical shape:

- Step-1: n molecules flow into the metastable region to serve as a primary nucleus for the liquid embryos. This process does not contribute to the Gibbs' free energy variation. Thus:

$$\Delta G_1 = 0 \tag{3.63}$$

- Step-2: there is an isothermal expansion of the n molecules from the vapor pressure P_v to the local saturation one P_{sat}. By consequence, Eq. (3.64) determines the work related to this process.

$$\Delta G_2 = \frac{4}{3}\pi r^3 \rho_l \int_P^{P_{\text{sat}}} \frac{1}{\rho_v} dP = -\frac{4}{3}\pi r^3 \rho_l R T_v \ln(S) \tag{3.64}$$

- Step-3: the n molecules condense isothermally at the saturation pressure P_{sat}, forming a flat surface at which the chemical potential is equal for the liquid and vapor phases; consequently, the Gibbs' free energy is unaffected by this process.

$$\Delta G_3 = 0 \tag{3.65}$$

- Step-4: the molecules become spherical clusters with radius r, hence:

$$\Delta G_4 = 4\pi r^2 \sigma \tag{3.66}$$

  Here, σ denotes the surface tension.

- Step-5: isothermal compression of the clusters occurs between the saturation pressure to the vapor pressure. Eq. (3.67) defines the work associated with this process.

$$\Delta G_5 = \frac{4}{3}\pi \left[P_v - P_{sat}(T_v)\right] \tag{3.67}$$

The contribution of the previous step Eq. (3.67) to the total variation of ΔG is negligible compared to the other steps, as Bakhtar et al. (2005) report. Then, Eq. (3.68) denotes the total Gibbs' free energy variation.

$$\Delta G = 4\pi r^2\sigma - \frac{4}{3}\pi r^3 \rho_l R T_v \ln(S) \tag{3.68}$$

The Kelvin-Helmoltz or critical radius r^* defined by Eq. (3.70) results from applying Eq. (3.69) to Eq. (3.68) (Bakhtar et al., 2005).

$$\left(\frac{\partial(\Delta G)}{\partial r}\right)_{r=r*} = 0 \tag{3.69}$$

$$r* = \frac{2\sigma}{\rho_l R T_v \ln S} \tag{3.70}$$

The critical radius represents the barrier that the flow must exceed to trigger condensation. Thus, Eq. (3.71) determines that barrier in terms of the Gibbs' free energy, (Bakhtar et al., 2005):

$$\Delta G^* = \frac{4}{3}\pi r^{*2}\sigma = \frac{16\pi\sigma^3}{3\left(\rho_l R T_v \ln S\right)^2} \tag{3.71}$$

As observed in Eqs. (3.70) and (3.71), if the flow is not subcooled (S<1), the values of the energy barrier and the critical radius are high and they impede the flow from condensing. In contrast, if S>1, those values diminish. Therefore, by increasing the supersaturation ratio, the probability that any cluster exceeds the energy barrier increases (Lamanna, 2000).

3.4.2 Nucleation theory

The calculation of the nucleation rate J constitutes the basis of homogeneous nucleation theory (Pandey, 2014). Models based on statistical mechanics and models regarding thermodynamic-kinetic concepts have historically focused on reaching this purpose. The statistical models tend to eliminate the uncertainties of the classical ones; nevertheless, their results are controversial (Bakhtar et al., 2005), and their implementation requires a high computational cost (Azzini; Pini, 2017). On the other hand, thermodynamic-kinetic models establish their fundamentals on the CNT and the Becker-Döring theory, which determine the rate of cluster formation per unit of volume (Lamanna, 2000).

Eq. (3.72) determines the nucleation rate in terms of molecular values (Bakhtar et al., 2005).

$$\frac{\partial f_g}{\partial t} = -\frac{\partial I_g}{\partial g} = \frac{\partial}{\partial g}\left[C_g n_g \frac{\partial}{\partial g}\left(\frac{f_g}{n_g}\right)\right] \tag{3.72}$$

In Eq. (3.72), g denotes g-mers which are clusters that comprise several liquid molecules. n_g and f_g respectively denote the number of g-mers per unit of volume and the concentration of g-mers. The term C_g is the rate at which a cluster acquires a molecule and I_g refers to the nucleation current(Pandey, 2014).

The solution of the kinetic expression Eq. (3.72), yields the mathematical statement that determines the nucleation rate J. In fact, Eq. (3.72) has a transient and steady state solution,

the kinetic expression Eq. (3.73) represent the steady behavior of Eq. (3.72).

$$J = \left[\int_{g=1}^{\infty} \frac{dg}{C_g n_g}\right]^{-1} \tag{3.73}$$

The solution of Eq. (3.73); leads to the steady form of the nucleation rate J reported by the CNT:

$$J_{CNT} = q_c \frac{\rho_v^2}{\rho_l} \sqrt{\frac{2\sigma}{\pi m_m^3}} \exp\left(-\frac{\Delta G^*}{k_B T_v}\right) \tag{3.74}$$

Here, q_c defines the condensation coefficient, m_m denotes the molecular mass of the fluid and k_B is Boltzmann constant. Refer to Bakhtar et al. (2005) for detailed information about the derivation of Eq. (3.74) from Eq. (3.73).

Tab. 3.8 lists the values of the molecular mass of steam and carbon dioxide.

Table 3.8 – Fluids' molecular mass

Fluid	molecular mass m_m (10^{-26} kg)
Steam	2.99046
Carbon dioxide	7.30803

Eq. (3.74) presents discrepancies with experimental measurements. Thus, several investigations have focused on modifying this expression by adding correction factors or by adopting other kinetic approaches. However, any model about steady nucleation rate J has the form of (Lamanna, 2000):

$$J = \kappa \exp\left(-\frac{\Delta G^*}{k_B T_v}\right) \tag{3.75}$$

Here, κ determines a kinetic factor that depends on kinetic theories employed (Lamanna, 2000). Nevertheless, this study focuses on the modifications made to the classical approach.

Courtney (1961) made the first modification to Eq. (3.74) by including the supersaturation ratio in the kinetic factor. Eq. (3.74) takes the temperature of the vapor and the droplets to be equal. Consequently, Kantrowitz (1951) proposed a correction term C to take into account the non-isothermal effects of the nucleation process. The condensation coefficient q_c was also the prime focus of several investigations; according to Bakhtar et al. (2005) it has values between 0.1 and 1 for steam; Bier et al. (1990b) on the other hand, reported that it is equal to 0.1 for pure carbon dioxide. Eq. (3.76) determines the nucleation rate after applying the previous corrections to Eq. (3.74)(Bakhtar et al., 2005).

$$J_{CL} = \frac{q_c}{C} \frac{\rho_v^2}{\rho_l} \sqrt{\frac{2\sigma}{\pi m_m^3}} \exp\left(-\frac{\Delta G^*}{k_B T_v}\right) \tag{3.76}$$

$$C = 1 + 2\frac{\gamma - 1}{\gamma + 1} \frac{h_v - h_l}{R T_v} \left(\frac{h_v - h_l}{R T_v} - \frac{1}{2}\right) \tag{3.77}$$

Where γ denotes the specific heat ratio of the vapor.

Other authors such as Dykas (2001), Grübel et al. (2014) and Sova et al. (2017) added the

calibration factor ξ in the exponential term in Eq. (3.74) which leads to the equation used in the present study:

$$J_{CL} = \frac{q_c}{C}\frac{\rho_v^2}{\rho_l}\sqrt{\frac{2\sigma}{\pi m_m^3}}\exp\left(-\xi\frac{\Delta G^*}{k_B T_v}\right) \tag{3.78}$$

As discussed, It has been chosen models based on the steady-state behavior of equation Eq. (3.72), which means that the change of the term J remains constant and independent of the cluster size (Lamanna, 2000). Wegener & Mack (1958) proposed a characteristic time τ^* determined by Eq. (3.79) to analyze the validity of that assumption.

$$\tau^* = \frac{\sigma}{RP\ln(S)}\sqrt{\frac{8\pi R}{T_v}} \tag{3.79}$$

The steady-state solution is suitable when that characteristic time varies between 10^{-7} and 10^{-6} s. Consequently, the typical cooling rate for nozzle flows is about 0.2 to 0.8 K/μs, which indicates that the variation of temperature in nucleation is insignificant (Lamanna, 2000). Besides, for unsteady nozzle flows, the scale of τ^* is in the order of 10 $^{-3}$ s (Fakhari, 2010). These facts suggest that the steady-state assumption has good approximations for both steady and unsteady behaviors as Lamanna (2000) reports.

As mentioned, the thermodynamic-kinetic models establish relations from properties at macroscopic scales to then predict molecular ones. The surface tension has consequently been the focal point of several discussions due to its effects on both the energy barrier and nucleation rate (Heinze, 2015). Capillary surface tension is different from that of flat surfaces in a bulk liquid as Pandey (2014) reports. By consequence, authors such as Bakhtar et al. (2005) and Heinze (2015) report that it has suffered several corrections yielding contradicting results and limiting, even more, the range of applicability of those nucleation models.

However, the present study employs the correlation developed by Vargaftik et al. (1983) Eq. (3.80) for steam in low pressures calculations, which is recommended by the IAPWS and covers operating temperatures up to 647 K. For carbon dioxide simulations, the current work uses the correlation presented by Mulero & Cachadiña (2014), which is widely employed and suggested in open source and commercial thermodynamic libraries such as CoolProp (Bell et al., 2014) and REFPROP (Lemmon et al., 2018).

$$\sigma = 0.2358\left(\frac{T_c - T_v}{T_c}\right)^{1.256}\left[1 - 0.625\left(\frac{T_c - T_v}{T_c}\right)\right] \tag{3.80}$$

3.4.3 Droplet Growth Theory

Droplet growth is a dynamic process that involves the heat and mass transported between the droplet and surrounding vapor, the net max flux in regard to the droplet, and the latent heat released to the vapor phase (Lamanna, 2000).

Homogeneous nucleation produces small critical clusters (from 10^{-10} to 10^{-9}m) that impedes from modelling these molecules' growth from a macroscopic continuum mechanics viewpoint (Fakhari, 2010). Hence, a general model has to take into account the simultaneous heat and mass transfer processes at the continuum and molecular scales.

Kinetic theories assume a region between the droplet surface and continuum. This region is known as the Knudsen layer, where mass and heat transfer occurs without collisions (Heinze, 2015). Concepts such as the Knudsen number Kn and the mean free path $\widetilde{l}$ of the vapor molecules thus characterize the transport phenomena involved.

$$Kn = \frac{\widetilde{l}}{2r} \tag{3.81}$$

$$\widetilde{l} = \frac{1.5\mu}{P}\sqrt{RT_v} \tag{3.82}$$

Eqs. (3.81) and (3.82) respectively define the Knudsen number and the mean free path, μ denotes the dynamic viscosity of the vapor (Gyarmathy, 1962).

For values of the Knudsen number:

- $Kn \ll 1$, continuum conditions govern.
- $Kn \gg 1$, a gas-kinetic regime such as the collisions of vapor molecules on liquid clusters prevails.

Investigations aim for a universal model able to characterize clusters' growth rate in wide ranges of Knudsen numbers, as well as the transitions between kinetic and molecular regimes. Unfortunately, such a universal model is not yet available, and the existing models have acceptable agreements regarding certain operating conditions and fluids, with steam being one of the most studied substances in this field. These growth rate theories are founded on the Langmuir model, this being a suitable method that approximates the continuum and gas-kinetic mechanisms (Lamanna, 2000). This model identifies the delimited zones of the continuum region, the Knudsen layer at which rarefied gas effects prevails, and the droplet perimeter, as sketched in Fig. 3.10. Furthermore, it is necessary to mention the studies developed by Gyarmathy (1962), Hill (1966) and Young (1980) who established the features of the growth theory employed in the current work.

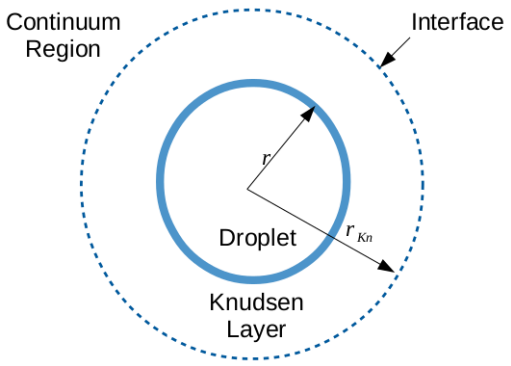

Figure 3.10 – Langmuir model
Font: Lamanna (2000)(adapted).

Following the procedure developed by Dykas (2001), Fakhari (2010) and Pandey (2014). The

energy balance of a spherical cluster may be written as:

$$\dot{Q} = 4\pi r^2 \alpha \left(T_d - T_v\right) \tag{3.83}$$

Eq. (3.83) determines the heat transferred from the droplet to the vapor phase. In terms of the latent heat released, $\dot{Q}$ can be expressed as (Dykas, 2001):

$$\dot{Q} = h_{lv} \frac{dm_c}{dt} = 4\pi r^2 \alpha \left(T_d - T_v\right) \tag{3.84}$$

Eq. (3.84) determines the net heat transfer involving the droplet and the surrounding vapor, dm_c/dt and T_d respectively denote the growth rate and temperature of the droplet, $h_{lv} = h_v - h_l$ is the latent heat of vaporization and α is a transport coefficient. The mass growth rate dm_c/dt for a spherical droplet is then determined from:

$$\frac{dm_c}{dt} = 4\pi r^2 \rho_l \frac{dr}{dt} \tag{3.85}$$

Combining and rearranging Eq. (3.85) and Eq. (3.84) leads to:

$$\frac{dr}{dt} = \frac{\alpha}{\rho_l} \left(\frac{T_d - T_v}{h_{lv}}\right) \tag{3.86}$$

Assuming that $T_d \approx T_{sat}\left(P\right)$, Eq. (3.86) then becomes:

$$\frac{dr}{dt} = \alpha \frac{1}{\rho_l} \left(\frac{\Delta T}{h_{lv}}\right) \tag{3.87}$$

Eq. (3.87) determines a general form of growth rate models, as appreciated in this equation, the droplet growth rate is a function of macroscopic terms such as the subcooling. However, the prime focus is the transport term α that must consider the continuum and molecular regimes as a function of the Knudsen number.

$$\frac{dr}{dt} = \left[\frac{\lambda_v \left(r - r^*\right)}{r^2 \left(1 + 3.18Kn\right)}\right] \frac{1}{\rho_l} \left(\frac{\Delta T}{h_{lv}}\right) \tag{3.88}$$

Here λ_v denotes the thermal conductivity of the vapor.

Gyarmathy (1962) proposed the droplet model defined in Eq. (3.88). This model considers the diffusion of vapor molecules, heat and mass transfer in liquid and vapor phases, and capillarity influence as well (Dykas; Wróblewski, 2012). Gyarmathy's growth model is employed by Sova et al. (2017) for condensation of steam under low pressures and Dykas & Wróblewski (2012) for high pressure conditions.

Young (1980) modified Gyarmathy's model by including the Prandtl number in the formulation of the droplet growth equation defined by Eq. (3.91). It should be stressed that Young's growth equation has been employed by CFD simulations for steam spontaneous condensation under low pressures conditions such as the works carried out by Blondel et al. (2015), Grübel et al. (2014) and Sova et al. (2017) to mention a few.

$$\frac{dr}{dt} = \left\{\frac{\lambda_v \left(r - r^*\right)}{r^2 \left[1 + \left(1 - \varsigma\right)\frac{3.78Kn}{Pr}\right]}\right\} \frac{1}{\rho_l} \left(\frac{\Delta T}{h_{lv}}\right) \tag{3.89}$$

Below, Pr is the Prandtl number of the vapor determined by Eq. (3.90) and Eq. (3.91) defines

the term ς.

$$Pr = \frac{c_p \mu}{\lambda_v} \tag{3.90}$$

$$\varsigma = \frac{RT_{sat}}{h_{lv}} \left[\psi - \frac{1}{2} - \frac{1}{2} \left(\frac{\gamma + 1}{2\gamma} \right) \left(\frac{c_p T_{\text{sat}}}{h_{lv}} \right) \right] \tag{3.91}$$

The term ψ represents a calibration parameter and $T_{\text{sat}} = T_{\text{sat}}(P)$. Hill (1966) proposed the growth rate model determined by Eq. (3.92). This model is considered an exception to the common rate models because it does not consider the Knudsen number to determine the droplet growth behavior, as observed in Eq. (3.92). It has been widely used in the MoM as Blondel et al. (2015) and Azzini (2019) report. However, Hill's growth model has suffered some modifications concerning the droplet temperature T_d.

$$\frac{dr}{dt} = \frac{P}{h_{lv} \rho_l \sqrt{2\pi R T_v}} \left(\frac{\gamma + 1}{2\gamma} \right) c_p \left(T_d - T_v \right) \tag{3.92}$$

Yang & Shen (2009) assumed that Eq. (3.93) defines the value of T_d in the Hill's droplet growth equation, achieving good agreements with the experimental data reported by Moore et al. (1973).

$$T_d = T_{\text{sat}} - \frac{2\sigma T_{\text{sat}}}{\rho_l} R h_{lv} \tag{3.93}$$

Alternative expressions for the temperature of the droplets have been also proposed by Gyarmathy (1962):

$$T_d = T_{\text{sat}}(P) - \Delta T \frac{r^*}{r} \tag{3.94}$$

Eq. (3.94) is used employed in the studies developed Dykas (2001), Fakhari (2010) and Dykas & Wróblewski (2012). Other droplet growth laws do not consider non-isothermal effects ($T_d = T_v$), which leads to inaccuracies with experimental data, as noticed by Lamanna (2000).

Finally, Tab. (3.9) summarizes the existing droplet growth rate models, it reports the CFD numerical works and the substances where those models were used.

Table 3.9 – Summary of droplet growth rate models.

Reference	Model	Substances	Implemented works
Gyarmathy (1962)	$\frac{dr}{dt} = \left[\frac{\lambda_v(r-r^*)}{r^2(1+3.18Kn)}\right]\frac{1}{\rho_l}\left(\frac{\Delta T}{h_{lv}}\right)$	Steam	Dykas & Wróblewski (2011) Dykas & Wróblewski (2012) Sova et al. (2017)
Young (1980)	$\frac{dr}{dt} = \left\{\frac{\lambda_v(r-r^*)}{r^2\left[1+(1-\varsigma)\frac{3.78Kn}{Pr}\right]}\right\}\frac{1}{\rho_l}\left(\frac{\Delta T}{h_{lv}}\right)$	Steam	Dykas (2001) Fakhari (2010) Grübel et al. (2014) Blondel et al. (2015) Sova et al. (2017) Karagiannis (2020)
Hill (1966)	$\frac{dr}{dt} = \frac{P}{h_{lv}\rho_l\sqrt{2\pi RT_v}}\left(\frac{\gamma+1}{2\gamma}\right)c_p\left(T_d - T_v\right)$	Steam CO_2	Yang & Shen (2009) Farag (2015) Azzini & Pini (2017) Senguttuvan & Lee (2019) Azzini (2019) Brinckman et al. (2019)

3.4.4 Droplet growth and two-phase thermodynamic properties

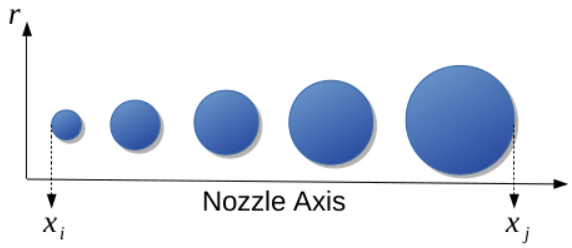

Figure 3.11 – Droplet growing.
Font: Author.

The following paragraphs briefly describe the relationship between the droplet growth models and the thermodynamics properties of a two-phase mixture. This analysis is based on a one-dimensional mesh approach that features in the reviewed literature.

As displayed by Fig. 3.11, Eq. (3.95) determines the radius of a cluster that formed at location x_i, considering a one-dimensional mesh with k elements that have size Δx (Sinha et al., 2009).

$$r_{(x_j;x_i)} = r_i^* + \sum_{k=i+1}^{j} \Delta r_k \tag{3.95}$$

Here, r_i* denotes the critical radius of the cluster at location x_i, the second term on the right-hand side of Eq. (3.95) represents the variation of the cluster size until location x_j and $r_{(x_j;x_i)}$ defines the actual radius at x_j. Therefore, Eq. (3.96) determines the term Δr_k.

$$\Delta r_k = \left(\frac{dr}{dt}\right) t \tag{3.96}$$

Where $\frac{dr}{dt}$ depends on the adopted droplet growth model, and t characterizes the time of the droplet growth at each Δx, as defined by Eq. (3.97).

$$t = \frac{\Delta x}{u} \tag{3.97}$$

It is necessary to establish a relation between droplet growth laws and wetness mass fraction y. Eq. (3.98) then determines the variation of the number of droplets per mass of flow $N_{(x_i)}$ at Δx (Sinha et al., 2009).

$$\Delta N_{(x_i)} = \frac{J_{(x_i)} \Delta x}{\rho u} \tag{3.98}$$

The term $J_{(x_i)}$ represents the volumetric nucleation rate defined by Eq. (3.74) or Eq. (3.78). Therefore, the superposition of the clusters formed upstream of location x_j and regarding Eq. (3.96), yields to (Sinha et al., 2009):

$$y_{(x_j)} = \frac{4\pi\rho_l}{3} \sum_{i=1}^{j} r_{(x_j;x_i)}^3 \Delta N_{(x_i)} \tag{3.99}$$

Eq. (3.99) determines the wetness mass fraction $y_{(x_j)}$ at any location x_j in a one-dimensional mesh; the summation term in this correlation involves the number and sizes of the droplets

formed upstream of location x_j (Sinha et al., 2009). For simplicity of notation, we assume $y = y_{(x_j)}$.

When the wetness mass fraction y is known, thermodynamic properties of the two-phase mixture, such as density, can be determined from:

$$\frac{1}{\tilde{\rho}} = \frac{1-y}{\rho_v} + \frac{y}{\rho_l} \tag{3.100}$$

Here, $\tilde{\rho}$ denotes the density of the two-phase mixture. It is worth mentioning that the vapor density is in metastable condition. The value of the second term of the right-hand side of Eq. (3.100) is negligible due to high values of liquid density in respect to wetness fraction's ones; hence the density of the mixture becomes:

$$\tilde{\rho} \approx \frac{\rho_v}{1-y} \tag{3.101}$$

Likewise, other thermodynamic properties of the two phase-flow, such as entropy and enthalpy, can be obtained from the wetness fraction y and the properties of the liquid and metastable vapor:

$$\tilde{h} = h_v(1-y) + yh_l \tag{3.102}$$

$$\tilde{s} = s_v(1-y) + ys_l \tag{3.103}$$

Eqs. (3.102) and (3.103) respectively define the enthalpy $\tilde{h}$ and entropy $\tilde{s}$ of the two-phase mixture.

3.4.5 Single Fluid Model

Sections 3.4.2 and 3.4.3 respectively presented concepts related to nucleation and droplet growth processes. Section 3.4.4, on the other hand, discussed relationships between two-phase mixture's averaged thermodynamic properties and growth the liquid phase. The following paragraphs present assumptions and concepts related to the implemented gas-kinetic model.

As mentioned in Chapter 1, the present study focuses on the SFM. This approximation treats the vapor and liquid phases as a homogeneous mixture or fictitious fluid. Under this consideration, the assumptions of the model are listed below:

- There is no slip between the droplets and vapor. Consequently, the velocity is equal for both phases (Dykas; Wróblewski, 2011; Sinha et al., 2009).
- Interactions of the droplets not considered (Sinha et al., 2009).
- Interactions between the liquid phase and surrounding nozzle walls are also omitted. This assumption makes impossible to model the liquid film at the nozzle walls (Smołka et al., 2016).
- Both phases are governed by the same pressure (Young, 1992). Subsequently, the specific

total energy of the mixture $\tilde{e}$ must obey (Dykas; Wróblewski, 2012):

$$\tilde{e} - (1-y)\, h_v\left(P, \rho_v\right) - y h_l\left(P, \rho_l\right) + \frac{P}{\tilde{\rho}} - \frac{1}{2}u^2 = 0 \tag{3.104}$$

It is worth noting that the assumption of equal pressure for liquid and vapor phases features on the existing gas-kinetic models (including TFM and MoM besides of SFM). As noticed in the studies carried out by Young (1992), Dykas & Wróblewski (2012), Blondel et al. (2015), Azzini (2019) and Pandey (2014), to mention a few.

While droplet growth is active and the two-phase mixture is not in thermodynamic equilibrium. There are relaxation processes associated to momentum, mass, and energy exchanges at the interface. Young & Guha (1991) distinguished three relaxation times: the first one is related the velocity slip at the surface, the second relaxation time is associated to thermal equilibrium of the droplets, and the third one refers to the thermal state of the whole medium. According to the first relaxation time, the momentum transfer reaches faster its equilibrium condition if droplets are small ($r < 10^{-6}$ m), there is no difference between the velocities of the liquid and vapor phases under this situation. The second relaxation time, which is the fastest one, implies that the temperature of the droplet attains its equilibrium condition. Lastly, the third relaxation time occurs slowly as the vapor reaches equilibrium, thus this process can be considered as frozen.

It should be pointed out that the analysis in respect to the first relaxation time justifies the SFM assumptions according to no-slip between vapor and liquid phases; since droplets' sizes produced by spontaneous condensation are lower than 10^{-7} m, as reported by the literature. The second relaxation time yields another simplification for the calculation of droplets' temperature where $T_l = T_{\text{sat}}(P)$. This assumption have been also considered in the numerical works developed by Blondel et al. (2015) and Pandey (2014).

A SFM approximation consists of solving compressible flow conservation equations for the two-phase fictitious fluid, and two other additional equations related to nucleation effects and conservation of the formed liquid clusters.

$$\frac{\partial \tilde{\rho} y}{\partial t} + \frac{\partial \tilde{\rho} u y}{\partial x} = \frac{4}{3}\pi \rho_l J r^{*3} + 4\pi \rho_l r^2 \frac{dr}{dt} \tag{3.105}$$

$$\frac{\partial \tilde{\rho} N}{\partial t} + \frac{\partial \tilde{\rho} u N}{\partial x} = J \tag{3.106}$$

Eqs. (3.105) and (3.106) respectively determine the partial differential equations for conservation of the liquid phase and number of droplets per unit mass N. As appreciated in such equations, the total number of droplets have a radius r and thus, monodispersion is assumed. However, the present study considers polydispersion of droplets by solving Eqs. (3.98) and (3.99) (instead of Eqs. (3.105) and (3.106)) in conjuction with algebraic conservation equations for compressible flow. Section 4.2.3, therefore, discusses this topic in detail.

4 MODEL IMPLEMENTATION

Chapter 3 presented the theoretical background and concepts involved in terms of EoS, compressible flow, and approaches for solving condensation shocks from a gas-dynamic discontinuity and kinetic perspectives. Consequently, the following paragraphs in this chapter describe the implementation of thermodynamic libraries and compressible flow solvers in a code program. This chapter also discusses considerations and procedures carried out in the implemented algorithms.

The present study employs the high-level programming language Python (Van Rossum, 1995) and also computational tools from packages such as NumPy (Oliphant, 2006) and SciPy (Virtanen et al., 2020) to solve equations that allows obtaining thermodynamic properties and conditions of the flow.

Fig. 4.1 displays the implemented algorithm for solving the previously mentioned equations. It consists in searching for an interval in the domain of a function $f(x)$ at which the range changes of sign. The current algorithm also implements a simple multiprocessing technique for searching the mentioned interval faster. As observed in Fig. 4.1, this technique assigns segments of the domain of $f(x)$ for several CPU processes that run simultaneously.

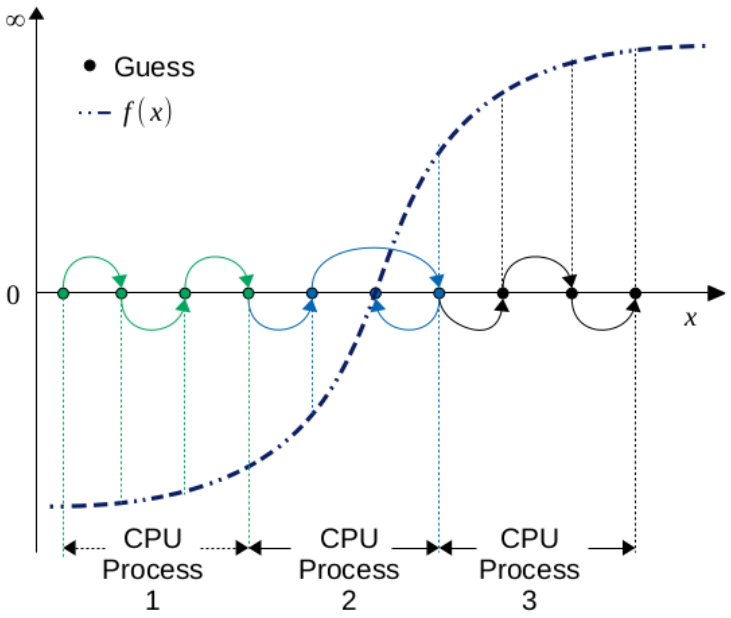

Figure 4.1 – Algorithm for root-finding.
Font: Author.

$$[f(x_{i-1})]\,[f(x_i)] < 0 \tag{4.1}$$

Here, the subscript i and $i-1$ respectively refer to the actual and previous iterations. When the algorithm finds an interval in the domain of $f(x)$ that satisfies Eq. (4.1), it then invokes the

fsolve function to obtain a root of $f(x)$.

fsolve from SciPy packages is a wrapper around minpack's hybrd and hybrdj algorithms (Virtanen et al., 2020), they use Powell's method (Powell, 1964) with some modifications for finding a root and multiple ones in non linear equations. Refer to Virtanen et al. (2020) for a detailed description about these algorithms' procedures.

On the other hand, it is also important to mention that the current work assumes an acepted error level Err less than 1.4e-08 to achieve convergence in the root-finding algorithm.

4.1 Thermodynamic property libraries

As discussed in section 3.1, the current work implements SW and IAPWS-95 EoS from the open source thermodynamic library developed by Bell et al. (2014). The iPRSV equation, on the other hand, has been implemented from the departure function theory. Three solvers compose iPRSV's thermodynamic library program:

- Pressure-temperature solver: pressure and temperature as input pairs.
- Pressure-specific entropy solver: pressure and specific entropy as input pairs.
- Specific enthalpy-entropy solver: specific enthalpy and entropy as input pairs.

It is worth mentioning that the pressure-specific solver computes fluid's properties in a isentropic expansion and the specific enthalpy-entropy solver obtains the stagnation conditions of the flow.

Pressure-temperature solver

The pressure-temperature solver is the most important one because it contains the residual properties and speed of sound calculation. It should be stressed that the current algorithm uses the polynomial form of the compressibility factor to obtain the fluid's volume from the pressure and temperature as input pairs.

$$Z^3 + \mathrm{Co}_1 Z^2 + \mathrm{Co}_2 Z + \mathrm{Co}_3 = 0 \tag{4.2}$$

With:

$$\begin{aligned} \mathrm{Co}_1 &= \Psi - 1 \\ \mathrm{Co}_2 &= \Upsilon - 3\Psi^2 - 2\Psi \\ \mathrm{Co}_3 &= \Psi^3 + \Psi^2 - \Upsilon\Psi \end{aligned} \tag{4.3}$$

Eq. (4.2) thus represents the iPRSV's polynomial form in terms of the compressibility factor Z (Van der Stelt et al., 2012), the term Ψ has been previously defined by Eq. (3.21), and the variable Eq. (4.4) is determined from:

$$\Upsilon = \frac{bP}{RT} \tag{4.4}$$

As observed in Eq. (4.2), the polynomial form of the iPRSV EoS has three possible solutions in the two-phase region where the reduced pressure and temperature are lower than one ($P_r < 1$ and $T_r < 1$). These solutions are easily obtained by the computational function *roots* from NumPy's packages. The pressure-temperature solver selects the highest value of Z that corresponds to vapor's compressibility factor during a single-phase isentropic expansion. This solver also choose both highest and lowest solutions to compute properties in the binodal curve. Eq. (4.5) defines the volume for any thermodynamic state determined by P and T.

$$v = \frac{ZRT}{P} \tag{4.5}$$

Further, the current code program obtains the especific enthalpy, entropy and speed of sound according to Eqs. (3.26), (3.27) and (3.30)

Pressure-specific entropy solver

The pressure-specific entropy solver works by iterating with the pressure-temperature solver in order to satisfy the input pairs requirements. Fig. 4.2 represents the algorithm employed by the this solver to obtain fluid properties.

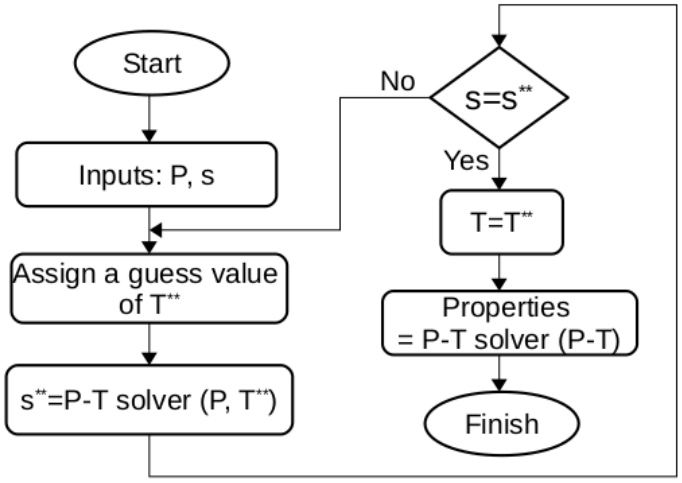

Figure 4.2 – Pressure-specific entropy algorithm.
Font: Author

Once the pressure-specific entropy function receives its input pairs, it starts iterating with the pressure-temperature solver to obtain a fictitious entropy s^{**} from a guess value of temperature T^{**} in order to satisfy the equality between the input entropy s and a fictitious value s^{**}.

However, in terms of computational calculations; it is impossible to satisfy an equality between two variables. Therefore, an admitted error must be defined to satisfy the mentioned requirement.

$$|s - s^{**}| \leqslant Err \tag{4.6}$$

Eq. (4.6) determines a error value Err in respect to the s and s^{**} variables. By consequence, the current study admits an admitted error value of $Err < 1.4\text{e}-08$ to satisfy the equality condition as discussed at the beginning of the current chapter.

Specific enthalpy-entropy solver

The specific entropy-enthalpy solver, on the other hand, works similar to the algorithm displayed by Fig. 4.2, but iterating with the pressure-specific entropy solver as shown by Fig. 4.3.

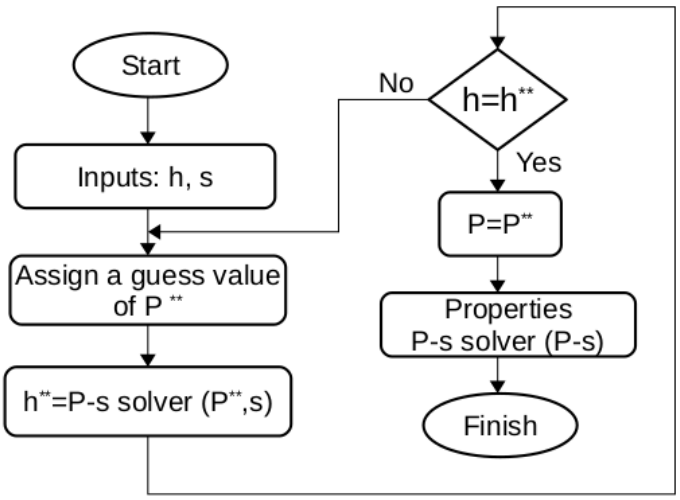

Figure 4.3 – Pressure-specific entropy algorithm.
Font: Author

4.2 Compressible flow solvers

4.2.1 Single-phase flow procedures

For vapor expansions with no occurrence of discontinuities such as normal shock waves and condensation shocks, the flow can be assumed as isentropic (Thompson, 1988). Therefore, the present study solves the mass, energy conservation requirements and the isentropic condition between two nozzle locations in order to characterize the single-phase flow. Three functions composes the single-phase flow code program:

- The first or throat function obtains the flow condition at the nozzle throat when the flow properties at the inlet are known.
- The second or stagnation function iterates with the first function to compute the flow properties at the throat and inlet from the stagnation conditions.
- The third or isentrotipc function obtains the flow conditions at any nozzle location from a reference location such as the nozzle throat.

For a better understanding of how the previously mentioned functions work, Fig. 4.4 presents the nomenclature of the nozzle principal locations. P_o and T_o respectively refer to the total or stagnation pressure and temperature at the nozzle inlet. The terms 1, 2, and j correspond to the inlet, throat, and arbitrary location of the nozzle.

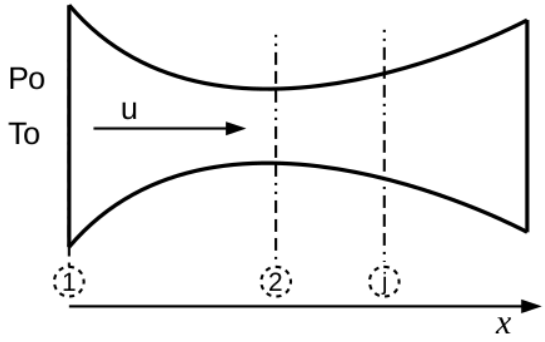

Figure 4.4 – Locations of the nozzle.
Font: Author

Throat function

When the properties at the nozzle inlet are known, the first function computes the flow conditions at the throat and the velocity at the inlet by employing the isentropic and sonic condition at the throat. Consequently, Fig. 4.5 presents this function's algorithm.

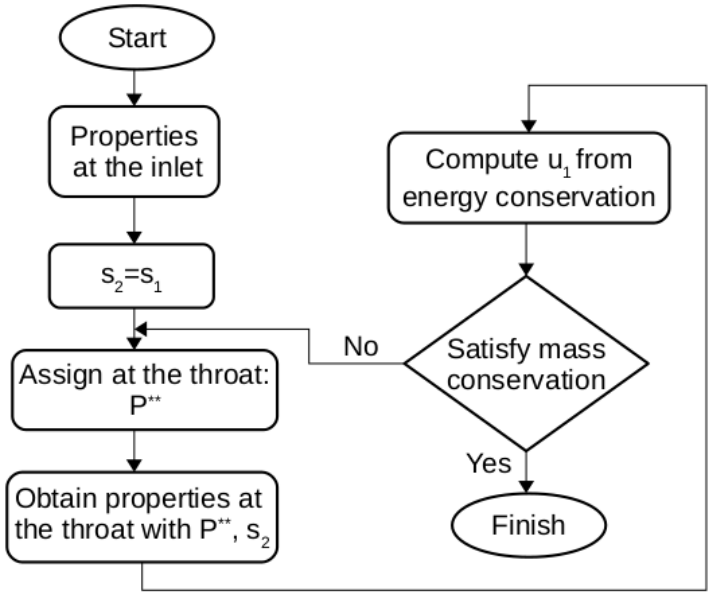

Figure 4.5 – Algorithm for finding the flow conditions at the nozzle throat.
Font: Author

As observed in Fig. 4.5, the throat function's procedure iterates by assigning a guess value of pressure at the nozzle throat until Eqs. (3.45), (3.39), (3.40) are satisfied. First, the algorithm establishes the isentropic condition between the inlet and throat locations defined by Eq. (4.7). Then, it assigns a guess value of pressure P^{**} at the throat.

$$s_2 = s_1 \tag{4.7}$$

With P^{**} and s_2, thermodynamic properties can be computed at location 2. The flow velocity at the throat corresponds to the speed of sound due to the sonic condition according to Eq. (3.44).

Consequently, the velocity at the inlet u_1 can be estimated by applying energy conservation between both locations.

Finally, the current procedure verifies the mass conservation requirement. If it is not satisfied, a new guess value of pressure must be assigned; otherwise, P^{**} corresponds to the actual pressure at the throat ($P_2 = P^{**}$), and thermodynamic properties can be computed with the input pairs P_2 and s_2.

It is also important to highlight that the throat function only obtains the sonic flow conditions if the thermodynamic properties at the inlet are known. However, this fact is not always suitable because stagnation properties such as pressure P_o and temperature T_o are always the initial conditions of the problem.

Stagnation function

The stagnation function obtains the flow conditions at the nozzle inlet and throat by iterating with the throat algorithm, with the purpose of satisfying the definition of total enthalpy determined from Eq. (3.41).

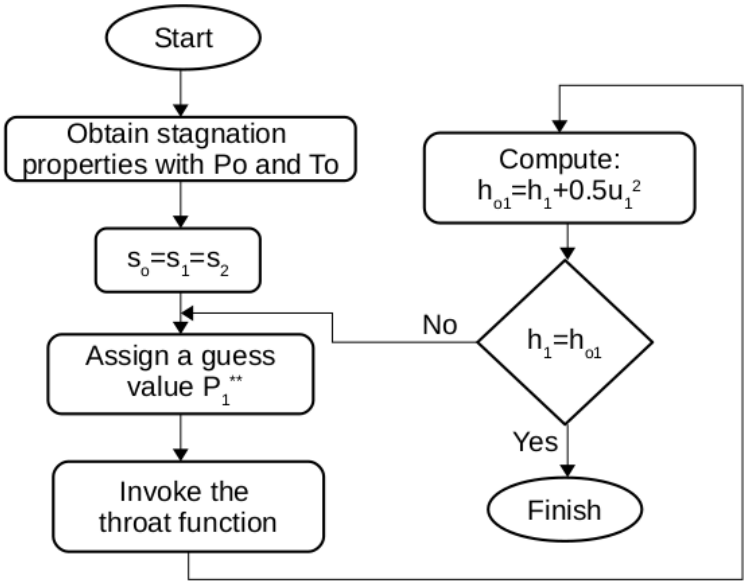

Figure 4.6 – Algorithm for finding the flow conditions at the nozzle's throat and inlet from stagnation properties.

Font: Author

The procedure displayed by Fig. 4.6 employs the following steps to achieve flow conditions at the mentioned locations:

- Obtain the stagnation properties from P_o and T_o.
- Apply the definition of stagnation entropy determined by Eq. (3.42) to the inlet and throat locations.
- Assign a guess value of pressure P_1^{**} at the inlet location.

- Invoke the throat function to obtain the flow conditions at the inlet and throat by employing P_1^{**} and s_1.
- Compare the stagnation enthalpy computed from P_1^{**} and s_1 to the actual stagnation enthalpy $h_o(P_o, T_o)$. If both values are equal then $P_1 = P_1^{**}$ and the flow conditions at the inlet and throat corresponds to the return values of the throat function. If not, define a new value of P_1^{**} and recall the throat function.

Isentropic function

The implemented first and second functions allows obtaining the flow conditions at the nozzle inlet and throat. However, the isentropic function computes the flow conditions at an arbitrary location x_j either in the convergent or divergent section of the nozzle. As appreciated in Fig. 4.7, this procedure function works similarly to the throat function's algorithm. Therefore, when the flow conditions at a reference location are known, the isentropic function assigns a guess value of pressure at x_j and determines Eq. (4.8) between the x_j and reference locations. The algorithm calculates flow properties at x_j with $P_{x_j}^{**}$ and s_{x_j}; it then obtains the velocity u_{x_j} from the energy conservation and verifies the mass conservation requirement between both locations. If the algorithm satisfies this condition, $P_{x_j}^{**}$ corresponds to the actual value of P_{x_j}. Otherwise, it remains iterating with $P_{x_j}^{**}$ until the mass conservation requirement is satisfied.

$$s_{x_j} = s_{\text{ref}} \tag{4.8}$$

Here, the subscript *ref* denotes a reference nozzle location. The current code program assumes the throat as the reference. It should be stressed that the isentropic function computes flow property and velocity distributions in a vapor isentropic expansion.

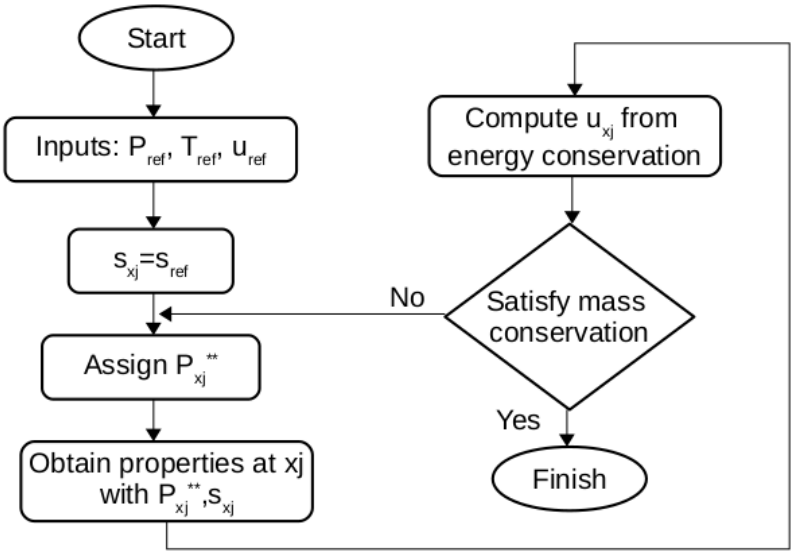

Figure 4.7 – Algorithm for finding the flow conditions at any location of the nozzle.
Font: Author.

In order to summarize and to clarify the interaction within the previous solvers (stagnation,

throat and isentropic functions), Fig. 4.8 displays the outputs of the stagnation function, whose inputs are the stagnation pressure and temperature at the nozzle inlet. Such a function iterates with the throat function to obtain the temperature, pressure and velocity in both inlet and throat locations of the nozzle. As previously mentioned when these locations are known, the isentropic function is used to obtain the flow properties in the convergent and divergent sections of the nozzle (as long as the vapor flow is isentropic).

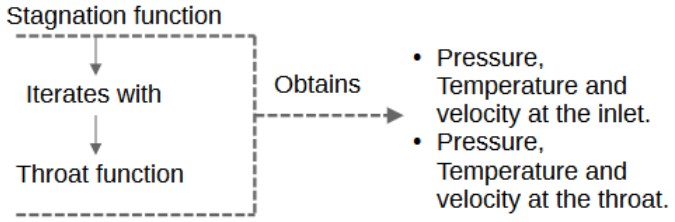

Figure 4.8 – Interaction diagram of the stagnation and throat functions.
Font: Author

4.2.2 Two-phase flow procedures

On the other hand, for a two-phase expansion in which thermodynamic equilibrium exists, the entropy of the mixture must be constant as Wegener & Mack (1958) report. Consequently, the algorithm presented by Fig. 4.9 is valid to solve a two-phase equilibrium expansion taking into account the properties of vapor and liquid calculated at $P_{\text{sat}}(T)$ and the vapor quality. The procedure displayed in Fig. 4.9 is described bellow:

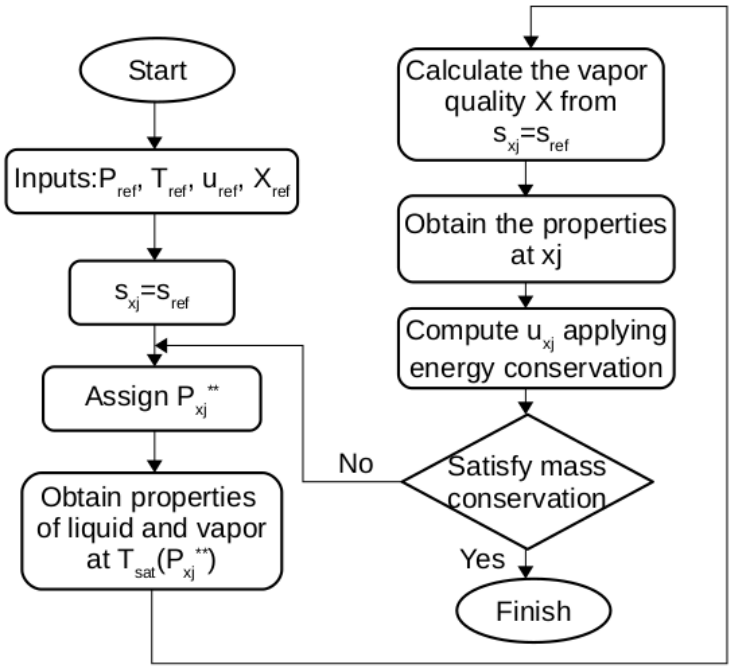

Figure 4.9 – Algorithm for finding the flow conditions during a two-phase expansion in thermodynamic equilibrium.
Font: Author.

- Obtain properties of the two-phase flow at a reference nozzle location.
- Assign a guess value of pressure $P_{x_j}^{**}$ at the location that one needs to solve.
- Compute equilibrium properties of vapor and liquid phases at the pressure $P_{x_j}^{**}$.
- Calculate the vapor quality by applying the isentropic condition between the x_j and reference location.
- Compute the properties of the two-phase flow and obtain the velocity by applying energy conservation between both locations.
- Verify if the mass conservation requirement is satisfied. If this condition is satisfied $P_{x_j}^{**}$ corresponds to the actual pressure at x_j, same as the properties and velocity obtained from this variable. Otherwise, assign a new guess values of $P_{x_j}^{**}$.

It is worth mentioning that the position of the weak detonation solution corresponds to the reference location for the two-phase expansion algorithm.

4.2.3 Droplet growth procedures

Sec. 3.4.4 briefly introduced the relationship between droplet growth processes and the thermodynamic properties of the two-phase mixture flow. This section clarifies aspects in respect to the discretization of droplet growth model and the implemented algorithm to solve a discretized element by applying conservation requirements and the restriction of the second law of thermodynamics.

As the flow moves downstream of x_i assuming a quasi-one-dimensional model, displayed by Fig. 4.10. Homogeneous nucleation produces the formation of new liquid particles ΔN_i at each Δx determined by Eq. (3.98). At each step, there is a superposition of groups of droplets formed at upstream locations defined by Eq. (4.9), this process is known as monomer addition (Sinha et al., 2009). Therefore, N becomes a conserved quantity in downstream intervals Δx, and contributing to the growth of the wetness fraction y.

$$N = \sum_{i}^{j} \Delta N_{(x_j;x_i)} \tag{4.9}$$

In Eq. (4.9), N determines to the total number of droplets per mass of flow at any location x_j and the summation term refers to the number of droplets formed upstream of x_j.

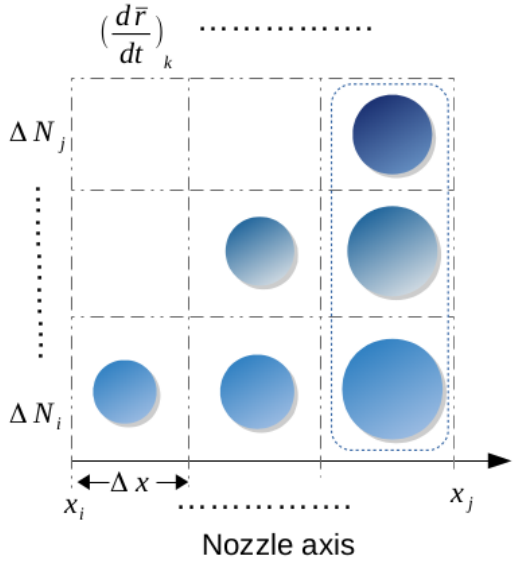

Figure 4.10 – Droplet growth discretization.
Font: Author.

Works such as the developed by Sinha et al. (2009), Heinze (2015), and Farag (2015), assume that each group of droplets have different and these droplets' initial size corresponds to the critical radius r^*. Consequently, the current study updates the droplets' sizes according to Eq. (3.95).

At each step, the growth of all groups of droplets are affected by a mean growth rate $d\bar{r}/dt$ defined by Eqs. (3.88), (3.89), or (3.92).

It is also important to mention that at each Δx, the implemented algorithm obtains thermodynamic properties and the velocity of the two-phase flow. By consequence, values of P, $\tilde{h}$, $\tilde{\rho}$ and u must satisfy the mass, momentum and energy conservation requirement for compressible flow behavior previously defined by Eqs. (3.37), (3.38) and (3.39).

Special interest arouses around the term I defined by Eq. (4.10) that corresponds to the integral quantity in the momentum conservation equation. The current study assumes a linear variation of the pressure distribution in respect to the area for small values of Δx. Under this assumption the value of I can be easily computed.

$$I = \int_{A_1}^{A_2} P dA \tag{4.10}$$

Here, the subscripts 1 and 2, which refer two arbitrary nozzle locations, they can be replaced by x_j and x_{j-1} according to the discretization model displayed by Fig. 4.10.

On the other hand, the algorithm must describe in such a manner the evaporation process of liquid clusters, which do not exceed the energy barrier upstream of the Wilson point state in concordance with the nucleation theory.

Bier et al. (1990b) implemented the droplet growth model as the flow crosses the saturation curve. Therefore, the Wilson point location is imposed by both the nucleation rate and droplet

growth processes.

Heinze (2015) initialized the droplet growth rate model downstream of the Wilson point by assuming a critical value of the nucleation rate $J = 10^{20}$ kg $^{-1}$ s^{-1}. However, nucleation rate values at the Wilson point are different, as observed in the reviewed literature.

Sinha et al. (2009) activated the droplet growth algorithm downstream of the nozzle's throat. This occurrence is just possible if the throat's flow conditions are metastable, but it does not often occur. Metastable flow can be achieved either in nozzle convergent or divergent sections. However, the Wilson point state must be located in the nozzle divergent section as discussed in Chapter 3.

The implemented droplet growth model in the current work initializes at x_i, when the flow encounters a favorable metastable state where the nucleation rate has positive values. It is necessary to mention that the current algorithm is not able to take into account evaporation effects and there are no contributions of the first groups of droplets to the wetness faction due to low nucleation rate values upstream of the Wilson point.

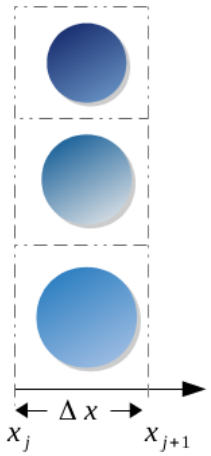

Figure 4.11 – Discretized element.
Font: Author.

Taking into consideration a discretized element displayed by Fig. 4.11 and the information provided by the previous paragraphs, Fig 4.12 presents the implemented algorithm to obtain flow conditions at x_{j+1} from the known location x_j.

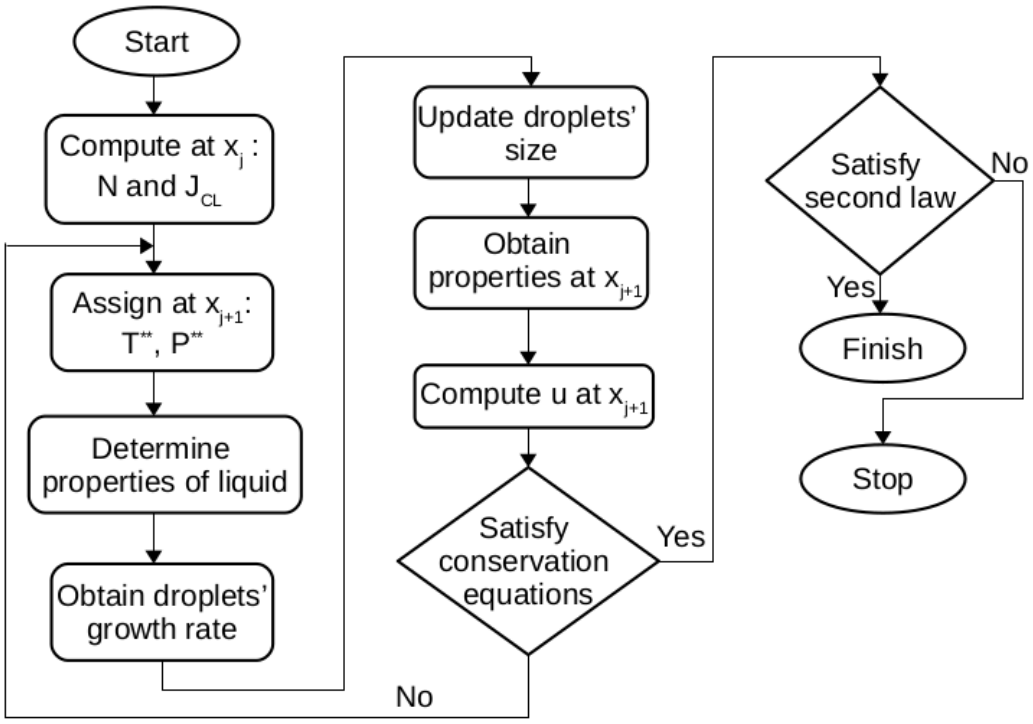

Figure 4.12 – Algorithm to solve a discretized element.
Font: Author.

The following steps describe the algorithm displayed by Fig. 4.12:

- Step 1: compute the nucleation rate and the number of droplets according to the flow conditions at x_j.
- Step 2: determine two guess values of thermodynamic properties such as the vapor temperature and pressure at x_{j+1} .
- Step 3: calculate the droplet's properties at $T_{sat}(P)$.
- Step 4: obtain the mean droplet growth rate $d\bar{r}/dt$ and calculate the local increase of the droplets' radius Δr.
- Step 5: update the radius of droplets according to Eq. (3.95).
- Step 6: compute the wetness fraction from Eq. (3.99) and obtain properties such as $\tilde{h}$ and $\tilde{\rho}$ at x_{j+1}.
- Step 7: calculate the velocity from the energy conservation Eq. (3.38) and verify if the mass, energy and momentum conservation requirements are satisfied. If it does not occur, repeat from step 2 with a pair of new guess values.
- Step 8: verify the second law of thermodynamics between x_j and x_{j+1} locations:

$$\tilde{s}_{x_{j+1}} \geqslant \tilde{s}_{x_j} \tag{4.11}$$

As appreciated, the convergence of the algorithm depends on the pair of guess values at x_{j+1}; therefore, a multidimensional root-finding algorithm for two variables is required to obtain the two-phase flow conditions at x_{j+1}. It is also important to mention that the guess values must be appropriate; otherwise, no convergence is achieved. Finally, steps 1 to 8 are solved until the nozzle geometry is completed.

4.3 Solution procedure

In order to implement the gas-dynamic discontinuity and kinetic approaches for solving condensation shocks, the geometric parameters of the nozzle and boundary conditions such as the total pressure and temperature at the inlet must be known. As mentioned in chapter 3, the gas discontinuity method is not able to predict the Wilson point location. Therefore, the solution from the gas kinetic approach must be obtained first to provide the location of this location.

The current work implements following steps obtains the solution from gas-kinetic theories:

1. Compute the conditions of the flow at the nozzle's inlet, throat and during the isentropic expansion by employing the algorithms described in section 4.2.1.
2. Calculate the supersaturation ratio S determined by Eq. (3.61) during the vapor isentropic expansion.
3. Obtain the nucleation rate determined by Eq. (3.76) when $S > 1$.
4. If the nucleation rate has positive values, initialize the droplet growth algorithm presented by section 4.2.3.

Taking into account the information contained in the previous steps, the flowchart displayed by Fig. 4.13 describes the interactions of flow solvers' procedures to obtain the gas-kinetic solution.

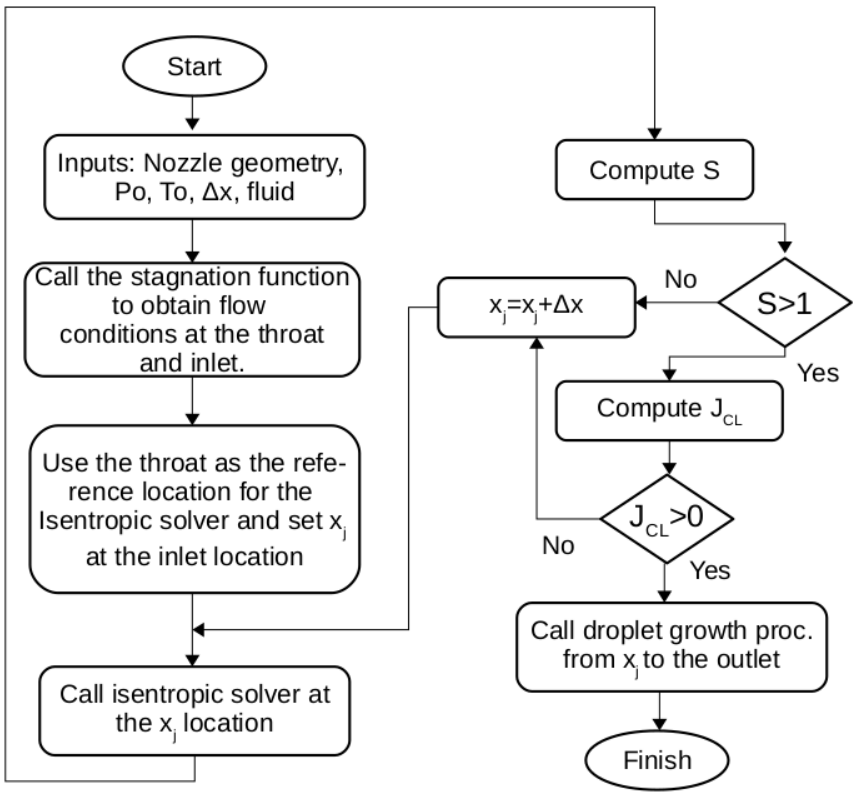

Figure 4.13 – Solution procedure for the gas-kinetic approach.
Font: Author.

With the Wilson point location x_W provided by the previous gas-kinetic solution, the present study obtains the solution from the gas-dynamic discontinuity approach according to the following procedure:

1. Compute the conditions of the flow at the nozzle's inlet, throat and during the isentropic expansion by employing the algorithms described in section 4.2.1.
2. Obtain the upstream conditions of the condensation shock when the flow achieves the Wilson point location.
3. Solve Eqs. (3.55) and (3.60), and chose the weak detonation solution as the downstream state of the condensation shock.
4. Verify the second law of thermodynamics for the jump conditions determined in the previous step.
5. Compute the flow conditions during an equilibrium two-phase expansion according to the procedure described by section 4.2.2.

The flowchart presented by Fig. 4.14 summarizes the information provided by the previous steps. It also describes the execution sequence of the compressible flow algorithms to obtain a solution assuming a condensation shock as a discontinuity.

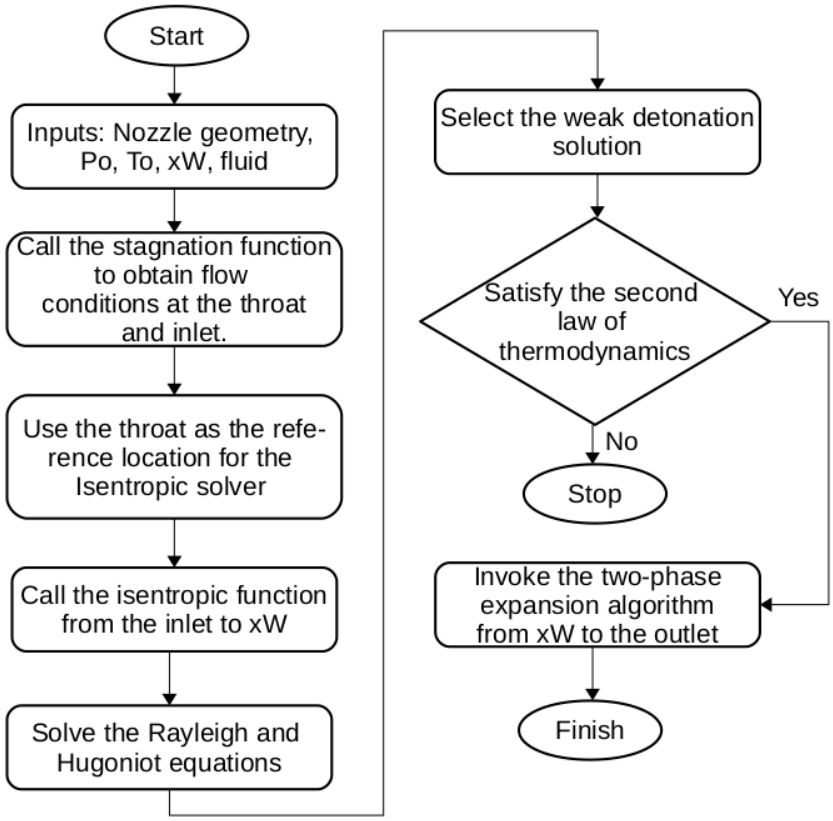

Figure 4.14 – Solution procedure for a gas-discontinuity approach.
Font: Author.

It should mentioned that the implemented code is available on: <https://github.com/AFBA1993/CondensationShocksNozzles>

5 RESULTS AND DISCUSSION

In order to asses the implemented models for characterizing condensation shocks in nozzle flows, Tab. 5.1 presents the used geometries, the fluids as well as the stagnation conditions at the nozzle inlet. It should be stressed that equations-of-state based on the Helmholtz free energy were employed in all cases, since they are the most accurate thermodynamic models for describing fluid properties of carbon dioxide and steam. Further, the iPRSV formulation was used to perform simulations for steam's non-equilibrium condensation under low pressure conditions. The simulated nozzle geometries listed in Tab. 5.1 pretend to evaluate and validate the implemented models with different fluids and flow conditions.

Table 5.1 – Assessed geometries and fluid conditions

Fluid	Reference	Geometry / Experiment	To (K)	Po (bar)
Steam	Moore et al. (1973)	Nozzle B	358.11	0.25
	Moses & Stein (1978)	exp. 410	377.15	0.70727
		exp. 417	308.50	0.70020
		exp. 428	303.32	0.54702
		exp. 434	373.15	0.41356
	Gyarmathy (2005)	Nozzle 4/B	638.68	100.7
			615.35	100.7
CO_2	Bier et al. (1992)	Nozzle B	300.12	45
	Arina (2001)	-	-	72

5.1 Helmholtz based EoS

5.1.1 Steam in low pressures

5.1.1.1 Moore's nozzle

The first simulation of non-equilibrium condensation of steam under low-pressure conditions was carried out in the nozzle geometry B of Moore et al. (1973). The stagnation conditions at the inlet were 25 kPa and 358.11 K. It was observed in section 4.2.3, that the implemented gas-kinetic approach depends on a discretized model. Therefore, it was necessary to analyze the predicted solution as a function of the number of elements in a one-dimensional mesh.

Fig. 5.1 displays the pressure ratio profile in the condensation shock region (from 0.03 to 0.038 m in the nozzle axis) for 100 to 10000 elements-mesh by using the droplet growth model defined in Eq. (3.88). As observed in this figure, the pressure ratio profile (in respect to the stagnation pressure P_o) predicted by a 100-element mesh was lower than the others. The solutions presented discrepancies from 100 to 1000 intervals. Conversely, from 4000 to 10000 discretized elements, there were no differences in the predicted pressure ratio distributions. Consequently, a 4000 element-mesh was capable of properly access the flow behavior, saving computational-time

calculation in respect to the other higher-number-cell meshes.

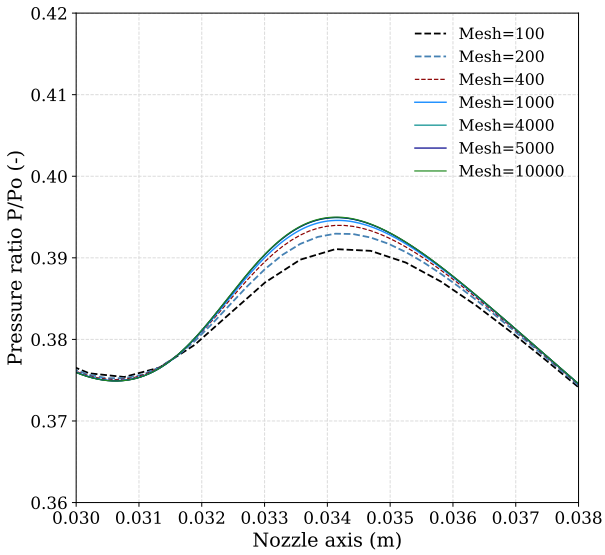

Figure 5.1 – Mesh analysis on the geometry of Moore et al. (1973).

Fig. 5.2 presents the main results for the gas-kinetic droplet growth models of Gyarmathy (1962) and Young (1980) (respectively defined by Eqs. (3.88) and (3.89)) and the discontinuity approach for condensation shocks. Fig. 5.2a reports the pressure ratio distribution from the throat location at 0.2 m to 0.6 m in the nozzle axis. Fig. 5.2b presents the strong, weak detonation and the Chapman-Jouguet conditions for the discontinuity approach. Fig. 5.2c and 5.2d respectively show the nucleation rate distribution for the gas-kinetic solutions and the mean radius of droplets downstream of the Wilson point location.

As mentioned, the gas-kinetic solutions must be obtained first to provide the Wilson point location for the discontinuity approach. During the isentropic expansion with Young and Gyarmathy's growth models, the flow crossed the binodal curve at 0.067 m in the nozzle axis. As the flow continued expanding in the metastable region, the kinetic growth models reported a peak in the nucleation rate at 0.267 and 0.2841 m as shown in Fig. 5.2c. Tab. 5.2 lists the exact values of the nucleation rate at the Wilson point location predicted by the implemented droplet growth approaches.

Table 5.2 – Location and nucleation rate of the Wilson point state for Moore's case.

Growth Model	Location (m)	Peak nucleation rate J_{CL} 10^{20} $(m^{-3}s^{-1})$
Young (1980)	0.26946	1.194
Gyarmathy (1962)	0.2841	7.876

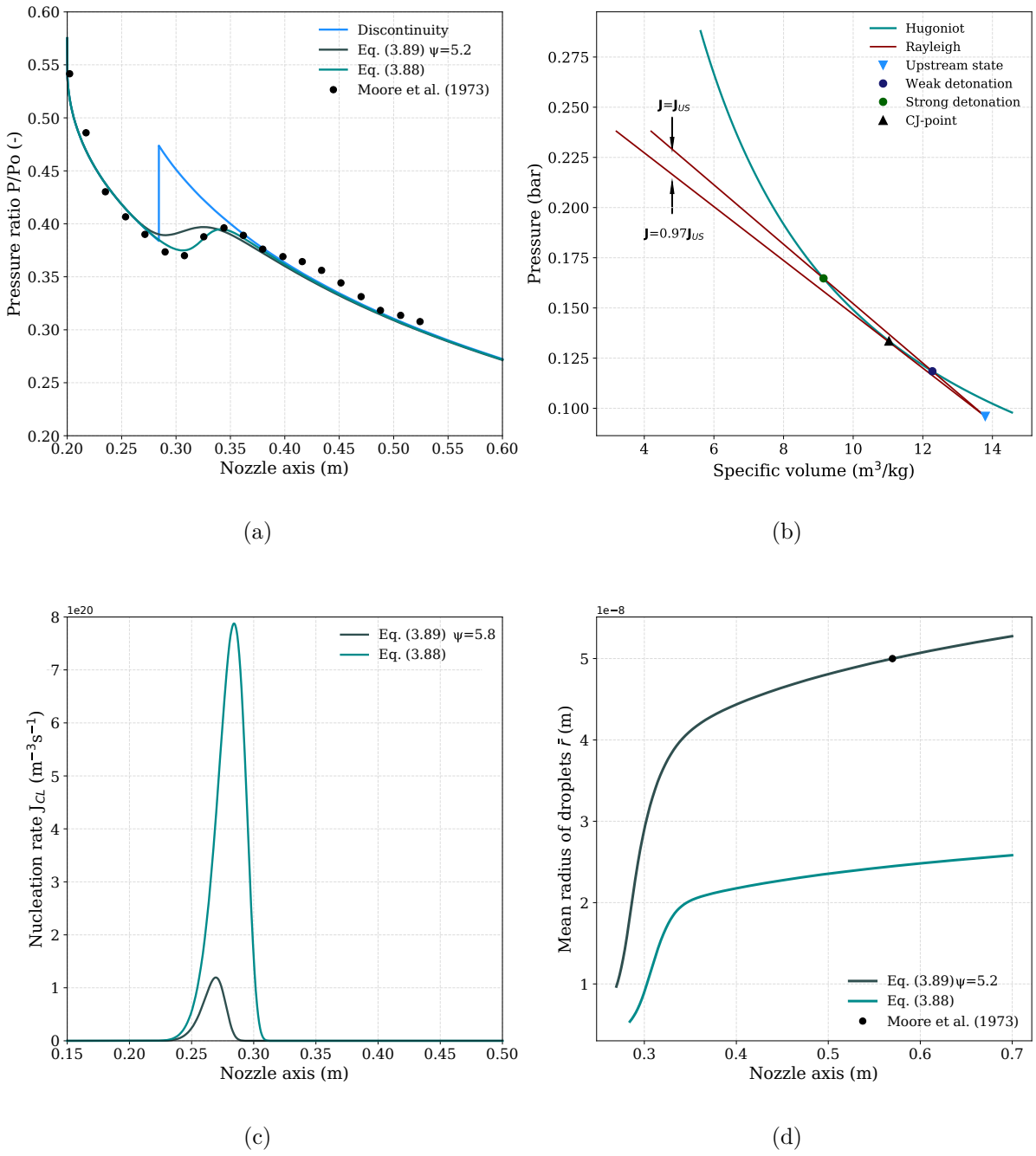

Figure 5.2 – Results for the nozzle geometry of Moore et al. (1973): (a) pressure ratio profile P/P_o, (b) intersections on the Rayleigh and Hugoniot curves, (c) nucleation rate profiles J_{CL} and (d) mean radius of droplets $\bar{r}$ (P_o = 25 kPa, T_o = 358.11 K.)

The difference on the predicted location and maximum nucleation rate value, occurred due to the maximum of supersaturation (or subcooling) achieved by the adopted model. Young's model attained a maximum subcooling of 25 K, whereas, Gyarmathy's model reached a value of 28 K. Downstream of the Wilson point location, the nucleation rate diminished due to heat released in the liquid phase and the mass transfer between the vapor and liquid phases. This occurrences increased the pressure and temperature of vapor as observed in Fig. 5.2c.

The location for the condensation shock in the discontinuity model was adopted from that of predicted by Gyarmathy's growth model. At this location, the isentropic expansion of the discontinuity model attained a velocity of 530.6 m/s, pressure of 9.597 kPa and a temperature of 290 K corresponding to the upstream conditions of the shock. Fig. 5.2b displays the possible states for the downstream condition and also the Rayleigh and Hugoniot curves. Tab. 5.3 reports the specific volume, pressure and mass flux rate for the upstream state, Chapman-Jouguet point, strong and weak detonations.

Table 5.3 – Characteristics of flow solutions for a condensation shock assumed as a discontinuity.

State	Sp. volume (m^3 kg^{-1})	Pressure (kPa)	Mass flux (kg s^{-1} m^{-2})
Upstream	13.793	9.597	38.474
Weak detonation	12.274	11.845	38.474
Strong detonation	9.14	16.473	38.474
Chapman-Jouguet	11.02	13.352	37.319

The mass flux of the upstream state, weak and high detonations have the same value satisfying the mass conservation requirement. The weak detonation state determined the solution for the condensation shock discontinuity, which resulted in a fluid compression and pressure rise of 1.519 m^3 kg^{-1} and 2.248 kPa in respect to the upstream state. The mass flux obtained from the Chapman-Jouguet point corresponded to 97 % of the value of the upstream state, which implied a lower Rayleigh's slope respecting the detonation curves illustrated in Fig. 5.2b.

It can be observed from Fig. 5.2a that the pressure ratio profile obtained from Gyarmathy's growth model had the best agreement (in respect to the other solutions) with the experimental data of Moore et al. (1973). From the nozzle throat location to 0.269 m, the predicted profiles by the gas-kinetic and discontinuity approaches had low deviations with the experimental data, presenting a minimum error of 1.5 % at 0.269 m and maximum discrepancy of 3.5 % at 0.21 m. The solutions presented the same error values because the flow is isentropic in this region.

In the condensation shock region, between 0.27 to 0.37 m. The pressure profile predicted by Young's droplet growth model and the discontinuity approach respectively had a maximum deviation of 6.2 and 24 % with the measurements. In case of the discontinuity model, it presented such deviations in this region, because, this model is not able to track the pressure profile in the condensation shock region due to the assumption that the phase-change process occurs instantaneously in the same cross-sectional area of the nozzle. The pressure ratio obtained from Gyarmathy's droplet growth model presented a discrepancy of 1.85 % at 0.29 m.

Downstream of 0.37 m, the three solutions attained similar values in the predicted pressure ratio, this occurred because of the heat and mass transfer processes involved in the condensation shock region that drove the pressure of the gas-kinetic approaches to an equilibrium pressure state, which, is also predicted by the discontinuity model. As the flow expanded downstream of the condensation shock region, both solutions had deviations about 4 % with the experimental values located between 0.42 and 0.45 m. Those discrepancies in respect to the available experimental data, in the isentropic and two-phase mixture expansions occurred because the implemented

quasi-one-dimensional model is not able to capture the effects of turbulence and boundary layer detachment, which is confirmed by the works of Senguttuvan & Lee (2019) and Sova et al. (2017).

Finally, in concordance with the doplets' mean radius distribution displayed by Fig. 5.2d. Both kinetic approaches predicted values in the order of 10^{-8} m. Young's model attained the reported experimental measurement. Gyarmathy's growth rate model under-estimated the mean radius value. However, the latter result had a low deviation with the experimental data due to the uncertainty involved at this scales.

5.1.1.2 Moses and Stein's nozzle

In order to evaluate the generality of the implemented algorithm for both gas-kinetic and discontinuity approaches under low-pressure conditions of steam. The current study performed several simulations in the nozzle geometry of Moses & Stein (1978). Firstly, a mesh analysis was carried out by employing the conditions reported by Moses and Stein's experiment 410 in order to determine the number of elements in an uniform mesh that were able to describe phenomena without waste of computational calculation time. The total conditions at the inlet were 70.727 kPa and 377.15 K (that correspond to 530.5 torr and 104 ^{o}C as mentioned in Moses & Stein (1978)). Fig 5.3, therefore, displays the pressure ratio distribution in the condensation shock region obtained from 100 to 10000 uniform-element meshes.

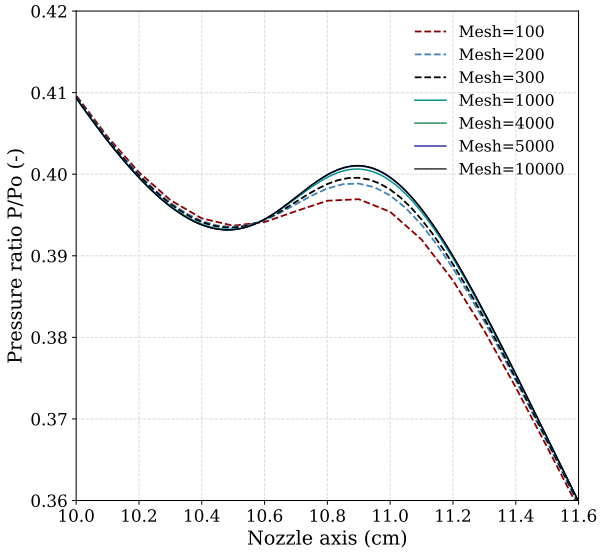

Figure 5.3 – Mesh analysis on the geometry of Moses & Stein (1978).

It can be appreciated from Fig. 5.3 that there is no variation in the pressure ratio profiles predicted by a 4000 to 10000 element mesh. Consequently a 4000 uniform interval-grid could describe the condensation phenomena with accuracy, the other meshes with less number of elements under predicted the pressure ratio distribution.

The tests evaluated in this geometry and their stagnation conditions at the inlet are listed

by Tab. 5.4.

Table 5.4 – Stagnation condition at the inlet for Moses and Stein's experiments

Experiment	Total temperature (K)	Total pressure (kPa)
410	377.15	70.727
417	308.5	70.020
428	303.32	54.702
434	373.15	41.356

For each test, the gas kinetic-approach with Gyarmathy's growth model obtained the Wilson point location and its nucleation rate reported by Tab. 5.5 and the condensation shock's upstream conditions (from the discontinuity model) in such location are listed in Tab. 5.6.

Table 5.5 – Location and nucleation rate obtained at the Wilson point by the gas-kinetic approach in Moses and stein's cases.

Experiment	Location (cm)	Peak nucleation rate (10^{22} m^{-3} s^{-1})
410	10.02	6.28
417	10.26	6.97
428	10.34	11.46
434	11.22	33.84

Table 5.6 – Upstream conditions for a condensation shock from the discontinuity model in Moses and Stein's nozzle.

Experiment	Pressure (kPa)	Temperature (K)	Velocity (m/s)
410	28.760	309.7	528.5
417	27.283	308.49	541.08
428	21.114	303.32	539.49
434	13.578	293.89	578.92

Fig. 5.4 displays the pressure ratio profiles obtained from the implemented algorithms in Moses and Stein's 410, 417, 428, and 434 experiments. Fig. 5.5, on the other hand, presents the jump conditions across the discontinuity condensation shock in a P-v diagram for each evaluated test.

As observed in Fig. 5.4, the gas-kinetic approach with Gyarmathy's droplet growth model was able to describe the pressure ratio profile with a good agreement with the experimental data, obtaining deviations within 1.3 % in all cases. It demonstrated that a quasi-one-dimensional inviscid flow approximation is sufficient to capture non-equilibrium condensation phenomena for this particular geometry and flow conditions. The discontinuity solution had also a good agreement with both experimental and gas-kinetic pressure ratio profiles except in the condensation shock region.

In concordance with Fig. 5.5, the jump conditions for the discontinuity for experiment 410 aroused interest. For this particular case, as shown by Fig. 5.5a, the Rayleigh lines of weak and strong detonations coincided with the Raleigh line that was tangent on the Hugoniot curve. Consequently, the Chapman-Jouguet state condition determined the solution for the downstream state of the condensation shock, just for this particular situation.

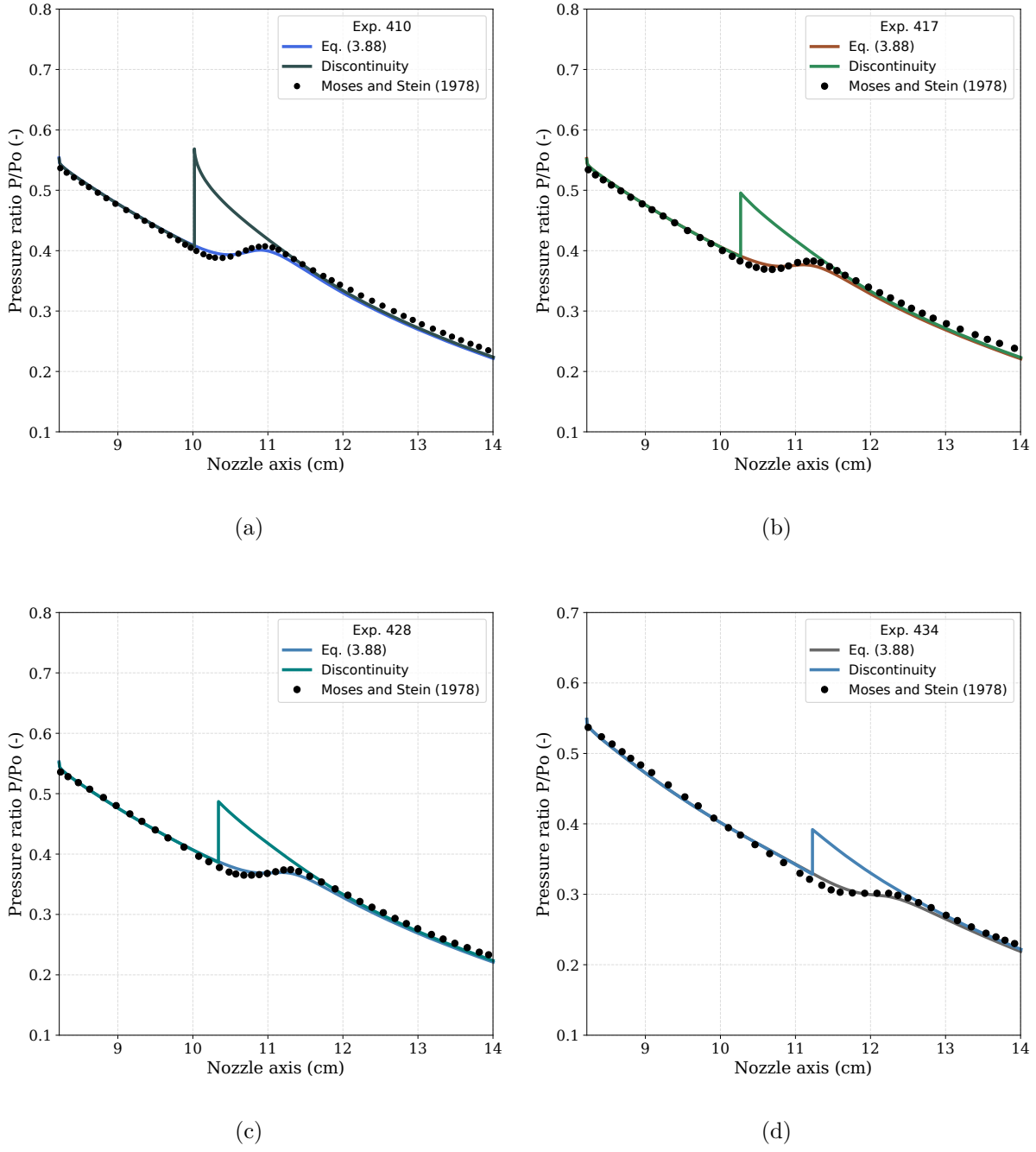

Figure 5.4 – Pressure ratio profiles for Moses and Stein's nozzle: experiments (a) 410, (b) 417, (c) 428 and (d) 434.

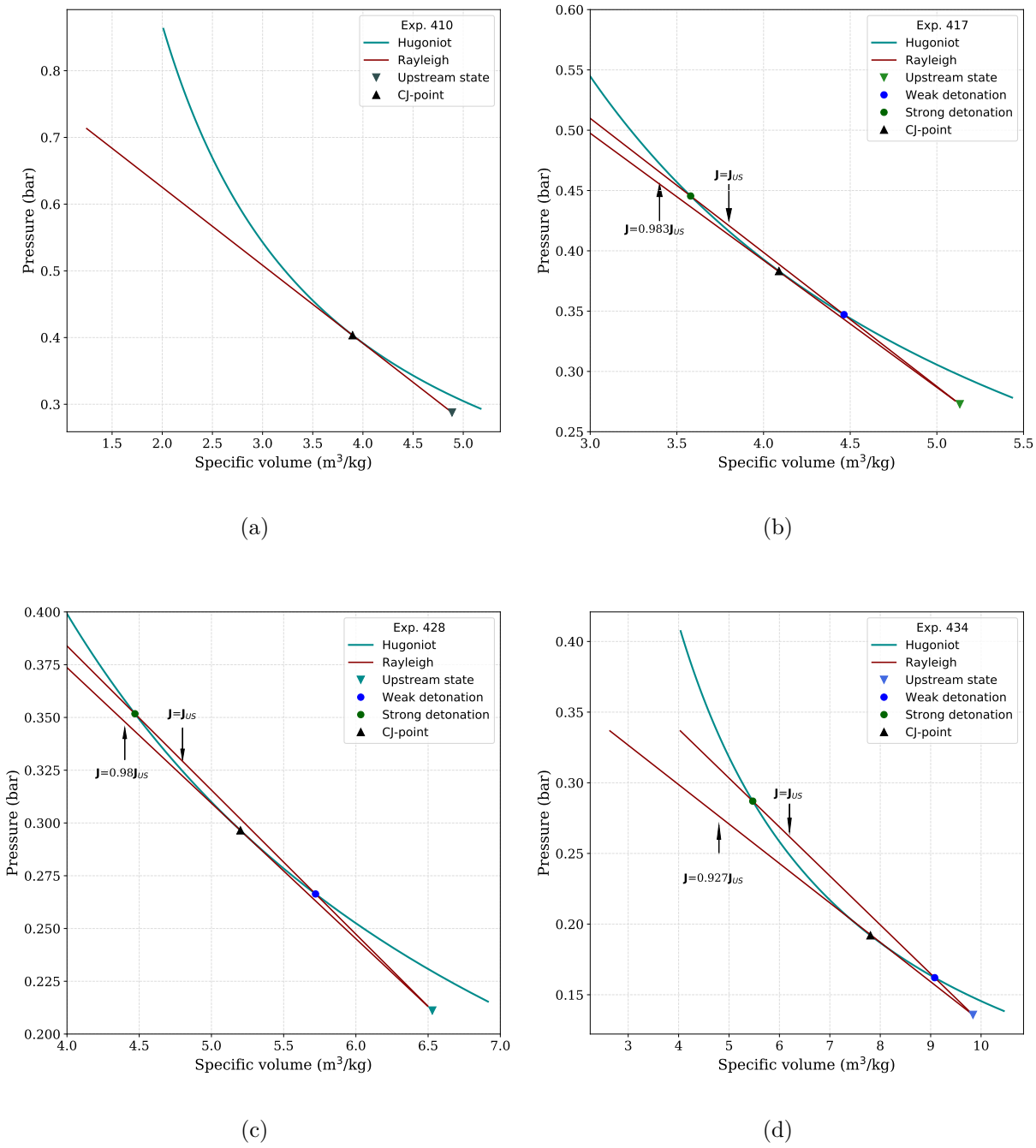

Figure 5.5 – Rayleigh and Hugoniot curves for Moses and Stein's nozzle: experiments (a) 410, (b) 417, (c) 428 and (d) 434.

5.1.2 Steam in high pressures

The current study also evaluates non-equilibrium condensation of steam in high pressures by employing the nozzle geometry and experimental data of Gyarmathy (2005). Following the methodology implemented under low pressure conditions, a mesh analysis was carried out first. Fig 5.6, therefore, displays the predicted pressure distribution in the condensation shock region for several one-dimensional meshes. The boundary conditions for the mesh test were determined

by the flow state at the throat reported by experiment 18c in Gyarmathy (2005), a pressure of 63.66 bar, and an entropy of 5.886 kJ/kg-K (stagnation entropy at the inlet obtained from 100.7 bar and 615.15 K) since the flow is isentropic during the single-phase vapor expansion from the inlet to the throat.

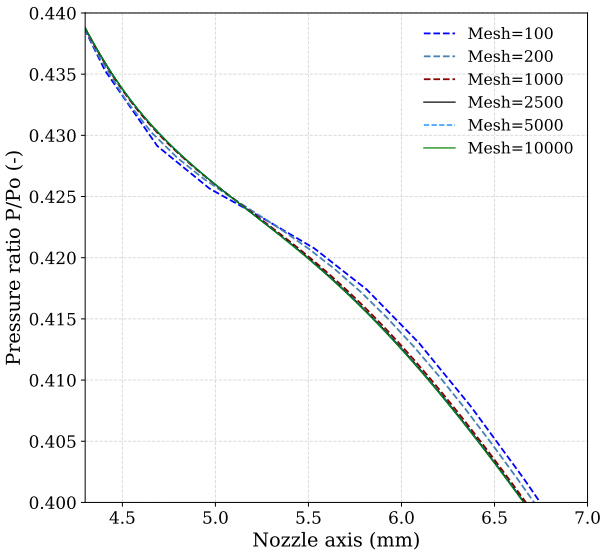

Figure 5.6 – Mesh analysis on the geometry of Gyarmathy (2005).

As depicted in Fig.5.6, a 100-element mesh over-estimated the pressure ratio distribution regarding the other meshes. As the number of elements was increased, the pressure ratio profile diminished. From 2500 to 10000 cells, there was no variation in the solution. Thus, a 2500 element uniformly spaced mesh was appropriate and sufficient to describe the flow conditions during condensation.

5.1.2.1 Test 18c

The first simulation under steam high-pressure conditions with both non-equilibrium approaches was carried out in the nozzle geometry 4/B of Gyarmathy (2005) with the boundary conditions of his 18c experiment. Consequently, Fig. 5.7 displays the main results for the first high-pressure case. Figs 5.7a, c and d respectively present the pressure ratio, nucleation rate, and radius profiles downstream of the throat location (at x =0 mm in the nozzle axis). Fig, 5.7b on the other hand, presents the intersections on the Rayleigh and Hugoniot curves for the discontinuity approach.

During the flow expansion, the implemented Gyarmathy's droplet growth rate model revealed that the flow crossed the vapor saturation curve at 0.6 mm from the throat location. The flow conditions at the throat being in the super-heated vapor state, whereas in low-pressure cases, they were in the metastable region. The flow attained the Wilson point at 4.3275 mm in the nozzle axis, and Tab. 5.7 reports some characteristics about that state. The maximum supersaturation

ratio and subcooling achieved corresponded to that of the Wilson state are also listed in the mentioned table.

Table 5.7 – Characteristics of the Wilson point state (simulation test: exp. 18c (Gyarmathy, 2005)).

Growth Model	Location (mm)	J_{CL} 10^{24} $(m^{-3}s^{-1})$	S (-)	ΔT (K)
Gyarmathy (1962)	4.327	3.577	1.275	14.33

With the location of the Wilson point reveled by the gas-kinetic model, the discontinuity approach was initialized and the condensation shock was placed at 4.32754 mm from the throat. At this location the flow attained a pressure of 44.01 bar, temperature of 514 K, and velocity of 622.05 m/s corresponding to the state upstream of the shock. Fig. 5.7b displays the possible downstream states for the condensation shock, and Tab. 5.8 provides detailed information about those solutions.

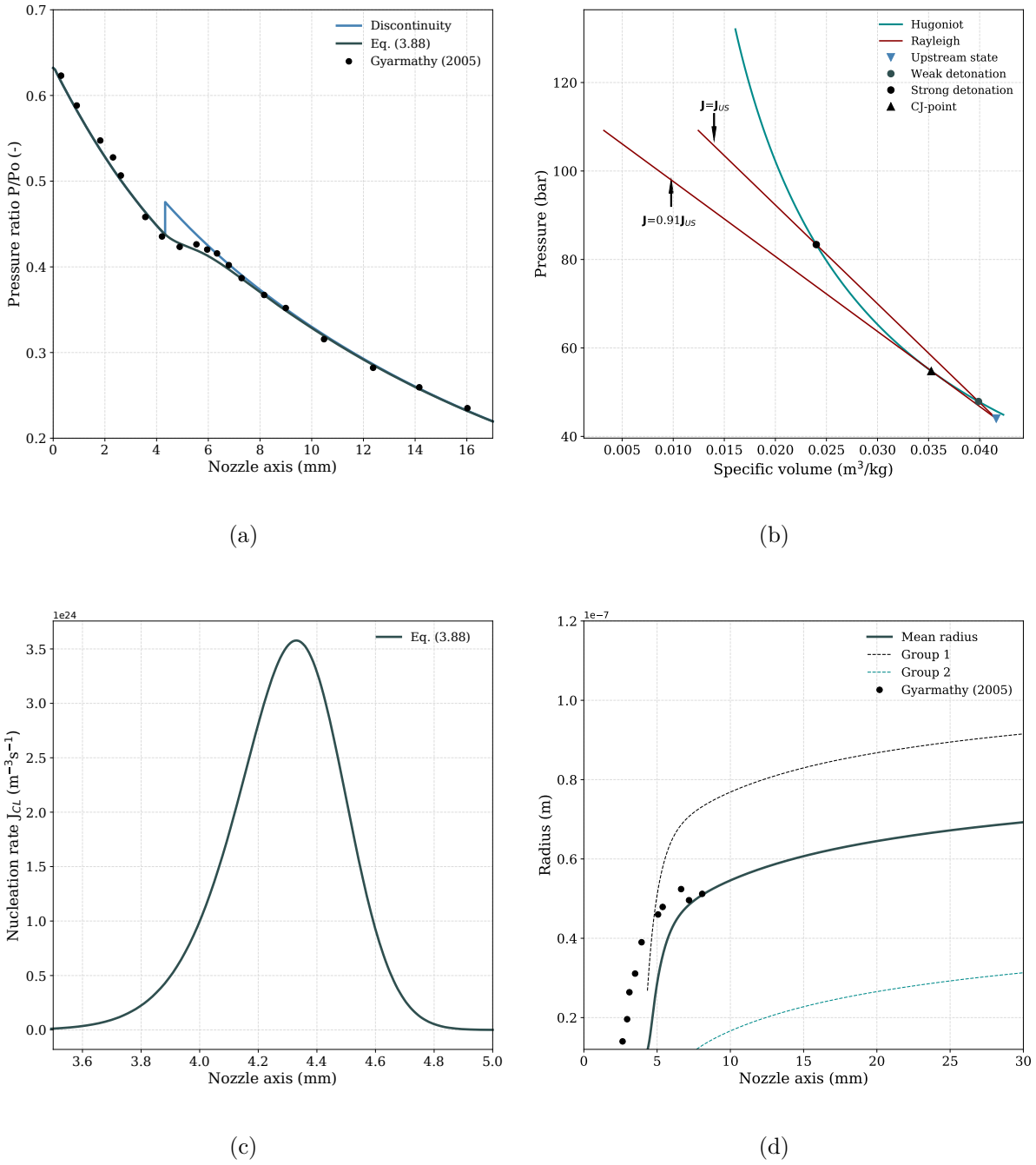

Figure 5.7 – Results for the test 18c of Gyarmathy (2005): (a) pressure ratio profile P/P_o, (b) intersections on the Rayleigh and Hugoniot curves, (c) nucleation rate profiles J_{CL} and (d) radius of droplets $\bar{r}$.

Table 5.8 – Characteristics of upstream and downstream states for a condensation shock assumed as a discontinuity (test 18c).

State	Sp. volume (m^3 kg^{-1})	Pressure (bar)	Mass flux (kg s^{-1} m^{-2})
Upstream	0.041	44.01	14944
Weak detonation	0.039	47.89	14944
Strong detonation	0.024	83.36	14944
Chapman-Jouguet	0.035	54.77	13599

It can be appreciated from Tab. 5.8 that for steam under high-pressures conditions the mass flux is higher than the computed in low-pressures cases. This is simply justified by the fluid density under the current states. The weak detonation solution for the downstream state of the shock resulted in a fluid compression and pressure rise of 0.002 m^3/kg and 3.88 bar (1.08 times the pressure of the initial state). Such a pressure increment across the shock was lower than the reported one in low pressures. It occurred because the Wilson point state is located close to the binodal curve achieving small values of supersaturation and subcooling in these states.

As shown in Fig. 5.7a, the predicted pressure ratio distribution from the gas-kinetic approach had low discrepancies with the experimental data. During the single-phase isentropic expansion from the throat to the Wilson point location, it had a maximum deviation of 2 percent. In the condensation shock region, downstream of the Wilson point location to approximately 8 mm, it presented a disagreement within 1.7 %. And downstream of the condensation shock region, the droplet growth model had a good adherence to the experimental data achieving deviations within 1%. The discontinuity approach, on the other hand, attained similar values with exception in the condensation shock region. The assumption of a condensation shock without thickness led to high discrepancies with the experimental data just in this portion of the nozzle. However, downstream of the condensation shock zone, it reported pressure ratio values equal to those attained by the implemented growth model and achieving consequently, small discrepancies with the experimental measurements.

Finally, in respect to the radius of droplets obtained from the kinetic model, Fig. 5.7d displays the profile of the mean radius and the size of two arbitrary groups of droplets formed downstream of the Wilson point state, demonstrating the ability of the algorithm to take into account a simple polydispersion behavior. In this figure, it is also observed that the magnitude of the predicted mean radius is in the order of 10^{-8} m having a good agreement with the last two measurements reported by the literature.

5.1.2.2 Test 18b

A second test was performed in the 4/B nozzle geometry of Gyarmathy (2005). The condensing flow expansion was carried out downstream of the nozzle throat by imposing a pressure of 66.36 bar (reported by Gyarmathy (2005)) and entropy of 6.033 kJ/kg-K (computed from the total pressure and temperature of 100.7 bar and 638.68 K). Fig. 5.8 presents the results for this case.

According to the implemented droplet growth model, the Wilson point state was located at 9.32 mm from the throat achieving a nucleation rate value of 2.95 10^{24} $m^{-3}s^{-1}$ as displayed in Fig. 5.8c. At this location, the discontinuity model revealed that the flow attained a velocity, pressure, and temperature of 752.8 m/s, 30 bar, and 491.67 K, corresponding to the upstream conditions of the shock. Fig. 5.8b, therefore, establishes the possible solutions for that state based on the intersections on the Rayleigh and Hugoniot curves. Tab. 5.9 includes other information about the specific volume and mass flux in those states.

Table 5.9 – Characteristics of upstream and downstream states for a condensation shock assumed as a discontinuity (test 18b).

State	Sp. volume (m^3 kg^{-1})	Pressure (bar)	Mass flux (kg s^{-1} m^{-2})
Upstream	0.060	30.519	12405
Weak detonation	0.059	32.50	12405
Strong detonation	0.025	85.10	12405
Chapman-Jouguet	0.051	38.14	10048

As observed in the table, the weak, strong detonations and the Chapman-Jouguet condition reported a pressure rise respectively of 1.98, 54.58, and 7.62 bar. The mass flux of the Chapman-Jouguet point represented 81% of the reported one by the upstream state of the shock. Since this solution did not satisfy the mass conservation requirement, the weak detonation state determined the flow conditions downstream of the shock, leading to a fluid compression of 0.001 m^3/kg for this case.

In concordance with Fig. 5.8a, from the throat to the Wilson point location, the predicted pressure ratio profiles predicted by both gas-kinetic and discontinuity models presented a deviation within 4 % in respect to the experimental data provided by Gyarmathy (2005). In the condensation shock region, the discontinuity approach had discrepancies in the order of 10 %, whereas the implemented growth model had deviations within 3.5 %. However, from 12.5 mm to the outlet, both solutions presented a good agreement with the experimental measurements, reporting deviation values lower than 1.5 %.

Fig. 5.8d, on the other hand, displays the radius of two arbitrary groups of droplets formed downstream of the Wilson point location and the mean radius as well. As appreciated, the predicted droplets' mean radius by the implemented Gyarmathy's growth model presented an agreement with the measurements from 12 mm to the nozzle outlet.

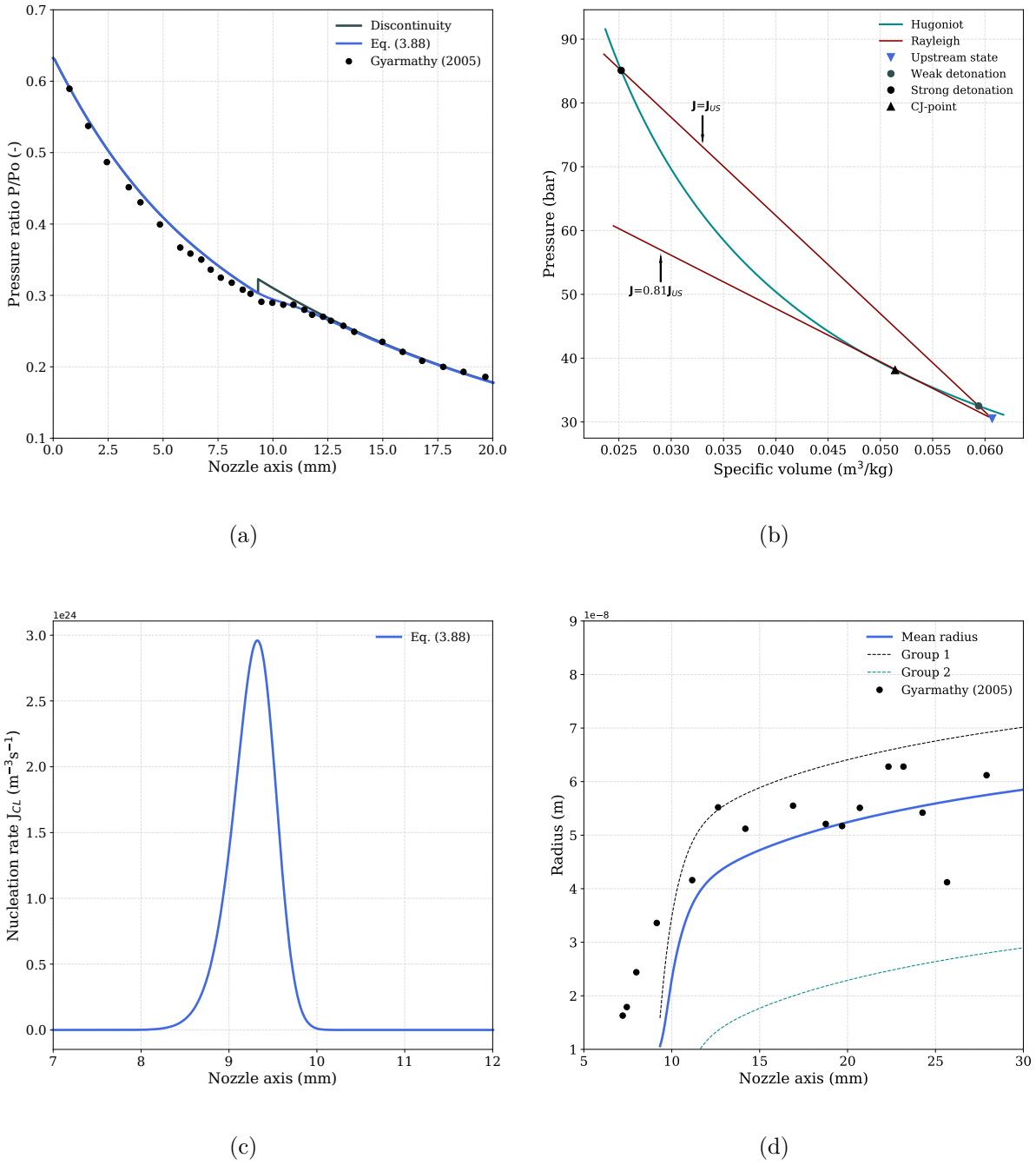

Figure 5.8 – Results for the test 18b of Gyarmathy (2005): (a) pressure ratio profile P/P_o, (b) intersections on the Rayleigh and Hugoniot curves, (c) nucleation rate profiles J_{CL} and (d) radius of droplets $\bar{r}$.

Further, other works had higher discrepancies on the droplets' mean radius prediction than the current. Dykas & Wróblewski (2012) obtained a calculation in the order of 10 $^{-7}$ m, Heinze (2015) presented similar deviations in both tests 18c and 18b, and Azzini (2019) added empirical correction factors to the surface tension calculation in her implemented model that resulted in low disagreement with the mean radius measurements in those tests.

5.1.3 Carbon Dioxide

5.1.3.1 Bier's nozzle

Both implemented approaches were also tested in carbon dioxide condensation shocks by employing the B2 nozzle geometry of Bier et al. (1990b). First, a mesh analysis was realized as displayed by 5.9. The total conditions at the inlet were set at 45 bar and 300.05 K. It is necessary to mention the present study computed the nucleation rate and growth rate of droplets according to Eqs. 3.88 and 3.76; since a purely carbon dioxide's kinetic model did not feature in the reviewed literature.

It can be appreciated from Fig. 5.9 that the predicted pressure ratio profile diminished as the number of elements of a uniform mesh was increased. A 100 cells grid presented high deviations regarding other meshes with a higher number of elements. However, the pressure ratio solutions did not have variations by employing a mesh with 2500 or higher number of intervals. Therefore, 2500 elements were sufficient to characterize the condensation phenomena in this nozzle geometry.

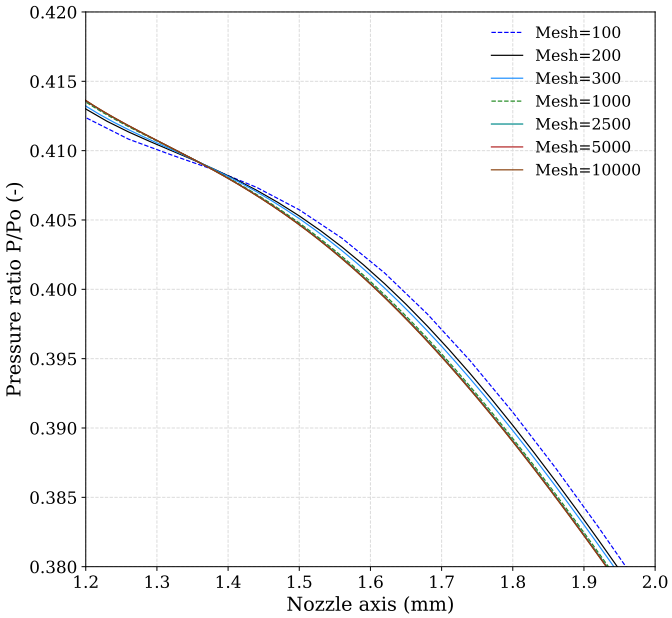

Figure 5.9 – Mesh analysis on the B2 nozzle geometry of Bier et al. (1990b).

The figure presents the results for carbon dioxide's evaluated test in the divergent section of the nozzle (the throat was placed at x =0 mm). The gas-kinetic approach reported that the Wilson point located 1.11 mm from the throat, achieving a peak nucleation rate of 7.8 10^{24} $m^{-3}s^{-1}$ as displayed by Fig. 5.10c. Tab. 5.10 lists other characteristics of the Wilson point state concerning the supersaturation ratio and subcooling at this state.

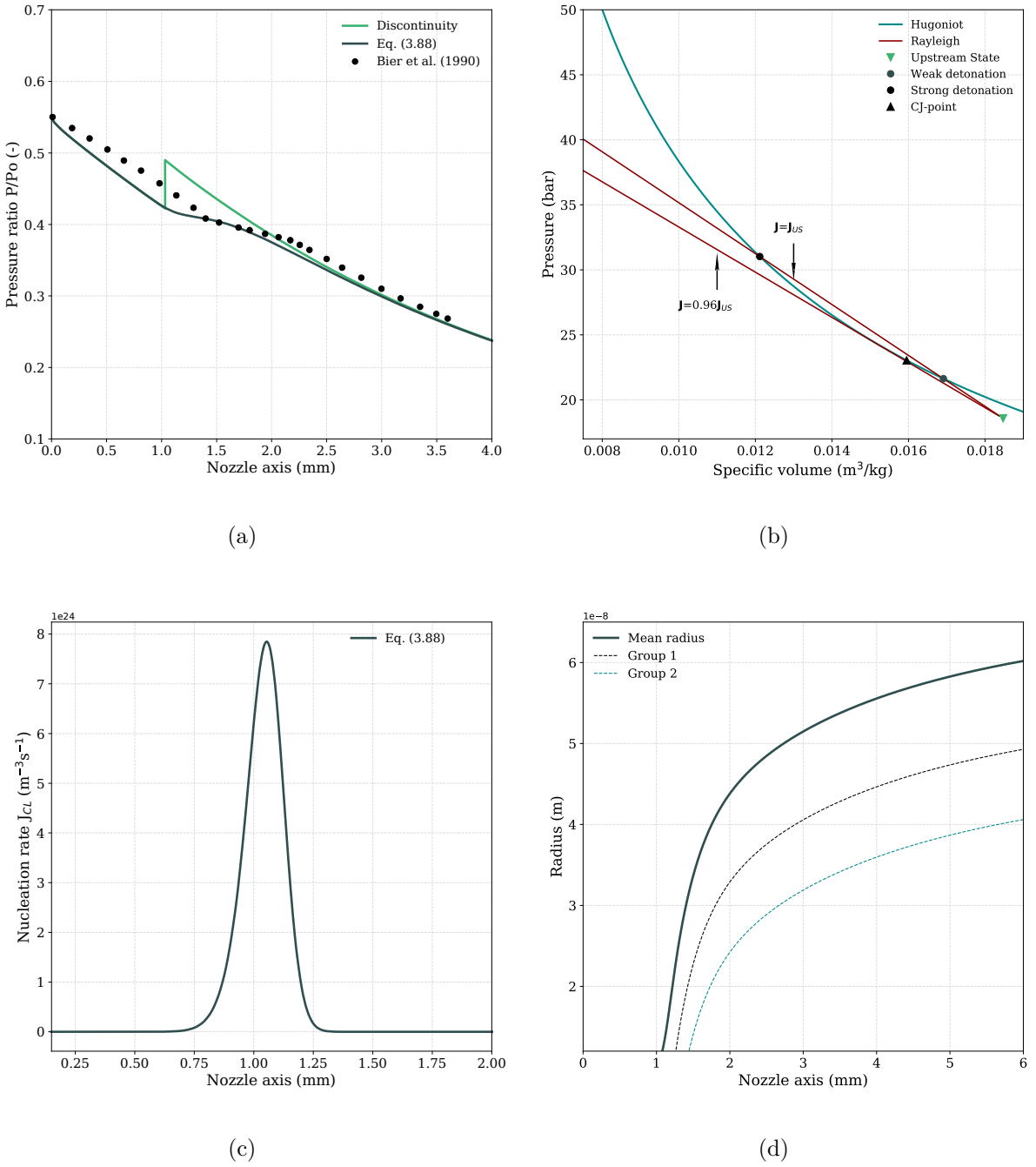

Figure 5.10 – Results for the case of Bier et al. (1990b): (a) pressure ratio profile P/P_o, (b) intersections on the Rayleigh and Hugoniot curves, (c) nucleation rate profiles J_{CL} and (d) radius of droplets $\bar{r}$.

Table 5.10 – Location and nucleation rate of the Wilson point state for carbon dioxide case.

Growth Model	Location (mm)	J_{CL} 10^{24} $(m^{-3}s^{-1})$	S (-)	ΔT (K)
Gyarmathy (1962)	1.117	7.848	1.4	10.48

Fig.5.10b displays the upstream and possible downstream states for a condensation shock from the discontinuity approach. The shock is located according to the Wilson point obtained from the kinetic solution.The flow attained pressure, temperature, and velocity respectively of 18.5 bar, 240 K, and 258.42 m/s at the upstream state of the shock. The weak detonation solution occasioned a fluid compression and pressure rise respectively of 0.02 m^3/kg and 3.05 bar across the discontinuity. Tab. 5.11 provides information regarding the detonation conditions and the upstream state.

Table 5.11 – Characteristics of upstream and downstream states for a condensation shock assumed as a discontinuity (carbon dioxide).

State	Sp. volume (m^3 kg^{-1})	Pressure (bar)	Mass flux (kg s^{-1} m^{-2})
Upstream	0.018	18.580	13991
Weak detonation	0.016	21.63	13991
Strong detonation	0.012	31.02	13991
Chapman-Jouguet	0.015	23.09	13431

In concordance with Fig. 5.10a, the predicted pressure ratio profiles by both discontinuity and kinetic approaches were in disagreement with the experimental data during the vapor expansion (from the throat to the Wilson point location), achieving discrepancies within 8 %. In the condensation shock region, from 1.11 to 2.75 mm, the implemented droplet growth model presented a maximum deviation of 4 percent, whereas the discontinuity achieved an error value of 8 %. Nevertheless, downstream of the latest location, both approaches predicted similar ratio profiles presenting deviations in the order of 3.5 % with the experimental measurements. From a general point-of-view, the calculated expansion lines from both models reported a similar distribution in respect to the experimental points but shifted to the left. The reasons for that shift are difficult to assess unequivocally since other studies in the literature have not worked with this geometry. It may be associated with turbulent and boundary layer detachment effects, phenomena that the implemented model is not able to capture and requires a future examination.

Finally, Fig. 5.10d displays the radius of two arbitrary groups of droplets and the mean radius of all droplets. As appreciated, their values ranged in the order of 10^{-8} m. It should be mentioned that Bier et al. (1990b) did not provide experimental data to validate the mean radius distribution.

5.1.3.2 Arina's nozzle

As noticed by Heinze (2015) and Trela et al. (2010), the occurrence of condensation in the Laval nozzle in ejector devices leads to lose of efficiency on this device's overall performance. Therefore, flow expansions were performed in the nozzle geometry of Arina (2004) with the purpose of reproducing carbon dioxide ejector's operating conditions free of condensation at a total inlet pressure of 75 bar.

Fig. 5.11, consequently, presents the pressure ratio profiles ranging within 325 and 351.4K inlet stagnation temperature (5.11a) and the Wilson point states obtained from the implemented

gas-kinetic model. It should be stressed that an uniform mesh with 4000 elements was used.

It can be observed from Fig. 5.11a that raises in the inlet stagnation temperature displace the onset of condensation in the nozzle. Therefore at $T_o = 351.5$ K, the Wilson state is located at the outlet, for that reason the pressure ratio distribution under those conditions behaves as an isentropic vapor expansion and temperatures above 351.5 K will establish flow conditions free of condensation in the nozzle. Furthermore, the Wilson states predicted by the gas-kinetic model were compared with the experimental Wilson line reported by Bier et al. (1990b) in Fig. 5.11b, as observed the results lies in agreement (less than 3%) with the experimental data.

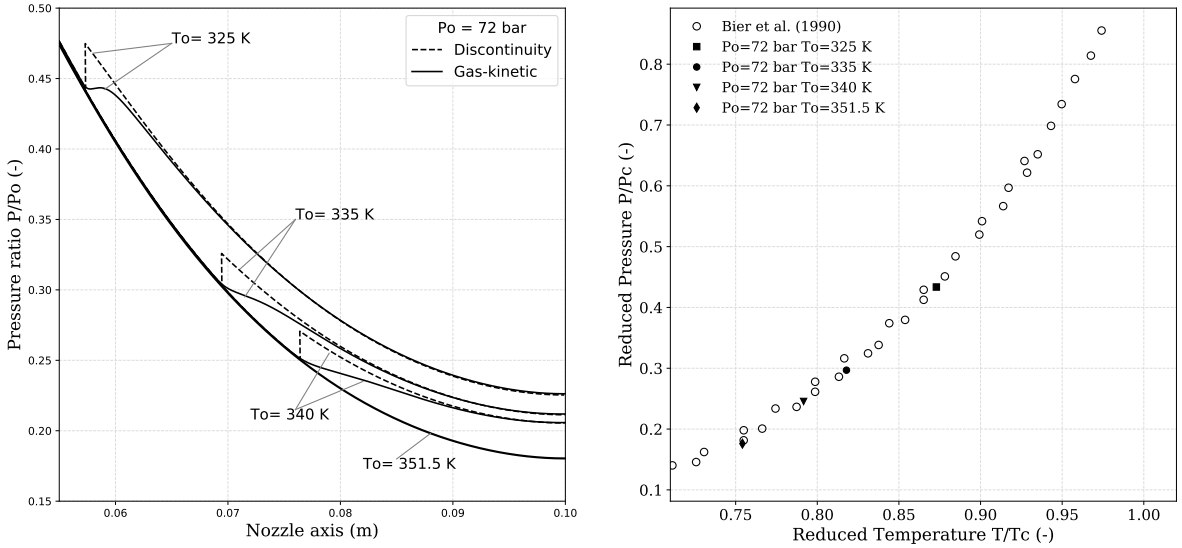

(a) (b)

Figure 5.11 – Results for the nozzle geometry of (Arina, 2004): (a) pressure ratio profile P/P_o, (b) Wilson point states.

Finally, The thermodynamic properties and the location of the Wilson points obtrained from the gas-kinetic approach are listed by Tab. 5.12.

Table 5.12 – Properties and location of the Wilson point states in Arina's nozzle.

$T_o(K)$	Location	Pressure (bar)	Vapor temperature (K)
325	0.057	31.985	265.48
335	0.069	21.889	248.73
340	0.076	18.104	240.75
351.5	0.01	12.98	229.35

5.2 iPRSV EoS

In order to evaluate the implemented condensation shock models with cubic equations-of-state, a final simulation was carried out with the iPRSV EoS in the nozzle geometry and conditions of the experiment 417 of Moses & Stein (1978) (steam being the working fluid, with total conditions of 308.5 K and 70.020 kPa at the inlet). An uniform mesh with 4000 elements was employed to determine the solution from the gas-kinetic theory, and Fig. 5.12 displays the main results for the discontinuity and droplet growth approaches.

The gas-kinetic solution revealed that the Wilson point state was located at 10.37 cm in the nozzle axis, achieving a nucleation rate of 1.91 m^{-3} s^{-1} as illustrated by Fig. 5.12c. Tab. 5.13 provides other information about the supersaturation ratio and subcooling attained at this state.

Table 5.13 – Characteristics of the Wilson point state (iPRSV case).

Growth Model	Location (cm)	J_{CL} 10^{24} $(m^{-3}s^{-1})$	S (-)	ΔT (K)
Gyarmathy (1962)	10.37	1.913	8.44	41.31

At the Wilson point location, the discontinuity model, on the other hand, reported that the flow attained a velocity, pressure, and temperature respectively of 557.34 m/s, 25.596 kPa, and 293.06 K, corresponding to the upstream conditions of the condensation shock. Fig. 5.12b, thus, displays the possibles solutions for the shock's downstream state. The Chapman-Jouguet's Rayleigh line implied 98 % of the mass flux of the upstream condition; hence, it did not satisfy the mass conservation requirement. The weak detonation solution obtained a pressure increase of 1.34 times regarding the upstream state yielding a compression of 0.81 m^3/kg. Also, Tab. 5.14 lists other relevant information for the detonation solutions.

Table 5.14 – Characteristics of upstream and downstream states for a condensation shock assumed as a discontinuity (iPRSV case).

State	Sp. volume (m^3 kg^{-1})	Pressure (kPa)	Mass flux (kg s^{-1} m^{-2})
Upstream	5.31	255.96	104.81
Weak detonation	4.50	345.54	104.81
Strong detonation	3.60	443.58	104.81
Chapman-Jouguet	4.11	382.47	102.71

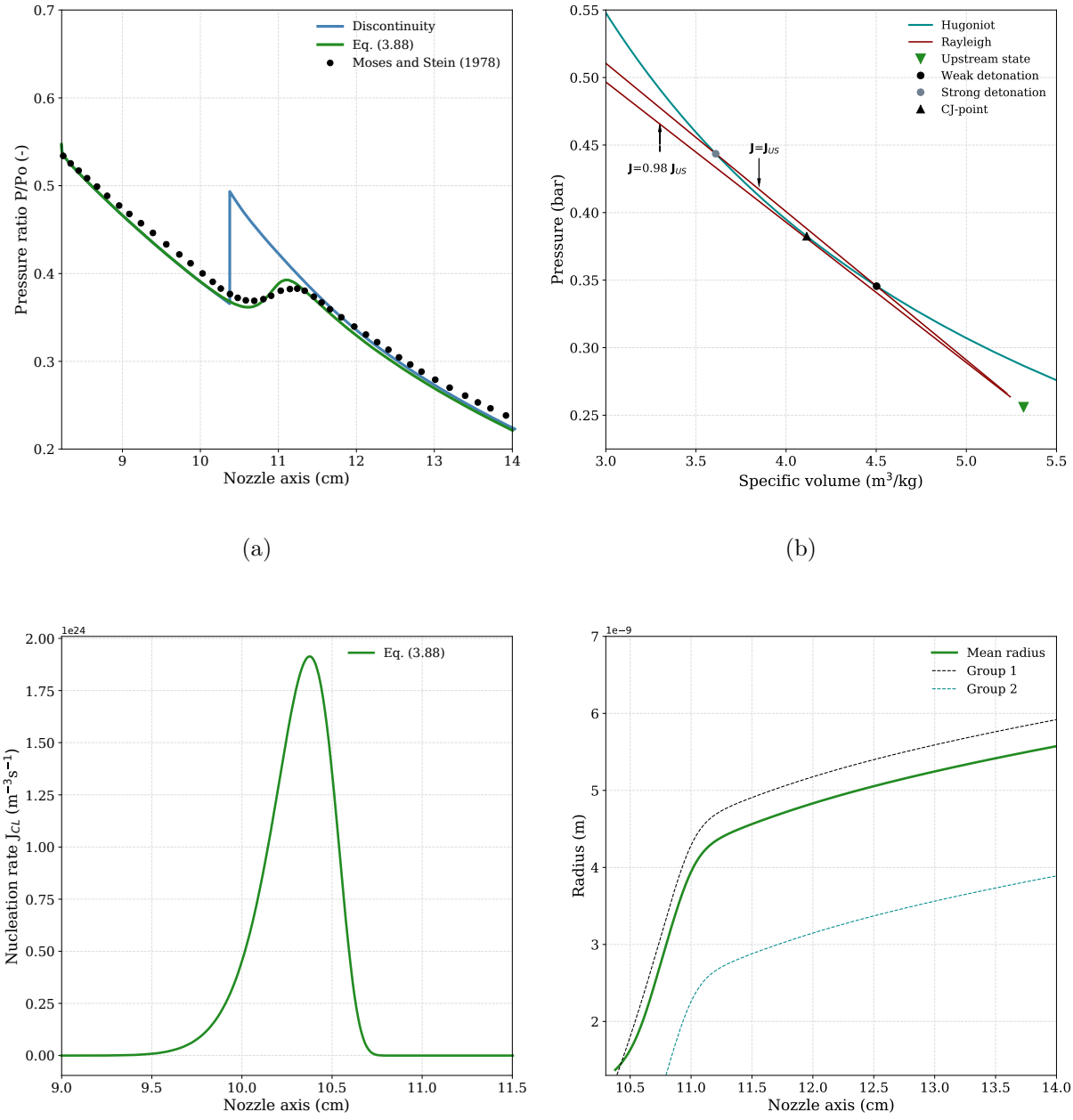

Figure 5.12 – Results for the iPRSV test: (a) pressure ratio profile P/P_o, (b) intersections on the Rayleigh and Hugoniot curves, (c) nucleation rate profiles J_{CL} and (d) radius of droplets $\bar{r}$.

As observed in Fig. 5.12a, the static pressure profiles obtained from Gyarmathy's growth model showed proper modeling of the phenomena regarding the experimental data, estimating the Wilson point location with accuracy. This approach presented deviations within 2.2 percent in the vapor expansion. In the condensation shock region, even the measured pressure profile was smoother than that of the kinetic model; the implemented droplet growth model presented discrepancies within 2.8 %. From 11.5 to 14 cm in the nozzle axis, it underestimated the pressure

ratio expansion lines by 3.9 %. The discontinuity model, on the other hand, reported similar deviations with the experimental data, with exception in the condensation shock zone.

In respect to the predicted mean radius distribution displayed by Fig. 5.12d, the kinetic model obtained values in the order of 10^{-9} m. It is worth mentioning that Moses & Stein (1978) did not provide experimental data for this test case.

6 SUMMARY AND CONCLUSIONS

The present study has implemented the iPRSV cubic EoS from departure function theory, other multiparemeter complex EoS based on the Helmholtz free energy such as the IAPWS-95 and SW formulations have been adopted from available open source thermodynamic libraries, in order to describe the non-ideal gas behavior of both steam and carbon dioxide substances. This Master's dissertation has also described two approximations for solving homogeneous condensation in nozzle flows; a SFM has been implemented by solving algebraic conservation equations for compressible flow in conjunction with gas-kinetic concepts related to nucleation and droplet growth, it has been demonstrated that the implemented SFM is able to take into account poly-dispersion of droplets. The second approach for condensation shocks assumed the phase-transition as a flow discontinuity, this being determined from intersections on the Rayleigh and Hugoniot curves. Both approximations were extensively tested and compared to experimental data in several nozzle geometries and conditions, leading to the following concluding remarks:

- The implemented gas-kinetic model characterized properly the pressure ratio distributions for both steam and carbon dioxide substances, achieving low deviations with experimental data of steam. For the carbon dioxide case, the pressure expansions lines obtained from the implemented droplet growth model captured the behavior reported by the experimental points. Nevertheless, it presented discrepancies within 8 % in respect to the reported measurements. It has been confirmed that the hypothesis $T_l = T_{\text{sat}}(P)$ does not result in loss of accuracy on the estimation of pressure expansion lines in condensing supersonic nozzle flows.

- The implemented droplet growth models compute the average droplet radius size distribution in the same order of magnitude of that of reported by the available experimental points.

- Intersections on Rayleigh and adiabatic Hugoniot (without heat release in the assumed control volume) curves occurs considering real gas behavior obtained from the Helmholtz energy based and iPRSV EoS. These occurrences have confirmed the theory developed by Guha (1994) but far from perfect-gas conditions.

- The discontinuity method describes properly the pressure distributions in condensing supersonic flows. Nevertheless, it fails on the pressure calculation in the condensation shock region reported by the experimental data. Downstream of the shock, heat and mass transfer processes involved in droplet growth take the flow pressure to an state which is also attained by a two-phase equilibrium expansion described by the discontinuity model.

- It has been demonstrated that the weak detonation state obtained from intersections on Rayleigh and Hugoniot curves estimates in agreement with the experimental data the pressure recovery that occurs in condensing nozzle flows. In most of cases, the

Chapman-Jouguet point's Rayleigh slope implies a mass flux lower than that of the upstream state, therefore, it does not guarantee the mass conservation in nozzle. It may occur that weak, strong and Chapman-Jouguet detonations coincide in the same predicted point as it has been observed in simulations in Moses and Stein's nozzle. For this particular situation the Chapman-Jouguet state also determines a solution for the condensation shock problem.

- It has been confirmed the accuracy of the iPRSV EoS to characterize condensing supersonic nozzle flows under low pressure conditions of steam.

It is relevant to mention that the methodology presented in this Master's dissertation have been published in Bolaños-Acosta et al. (2021).

6.1 Next steps

This Master's dissertation has described two methods for solving condensation shocks. As mentioned by Wegener & Mack (1958) a pure thermodynamic model can not describe the condensation process in supersonic condensing flows. Consequently, the present study has implemented a SFM from gas-kinetic theories in order to provide the Wilson point location for the flow discontinuity model. This can be enhanced by calculating such a state from an analytical method similar to the work developed by Azzini (2019). In terms of the implemented gas-kinetic model, a droplet growth model assuming evaporation effects must be examined. Theory about relaxations times to determine the applicability of a discontinuity condensation shock can be also developed. Finally, the present study will be extended to gas-mixture condensation shocks since that theory is still in early stages.

REFERENCES

Anand, G. *Phenomenological and Mathematical modeling of a high pressure steam driven jet injector*. 201 p. Ph.D thesis — The Ohio State University, 1993. Cited in page 17.

Anderson, J. D. *Modern Compressible Flow: With Historical Perspective*. 3. ed. [S.l.]: McGraw-Hill, 2003. (McGraw-Hill Series in Aeronautical and Aerospace Engineering). Cited 7 times in pages 35, 36, 37, 38, 39, 112, and 113.

Arina, R. Numerical simulation of near-critical fluids. *Applied Numerical Mathematics*, v. 51, n. 4, p. 409–426, 2004. Cited 3 times in pages 5, 91, and 92.

Azzini, L. *Numerical investigation of dense condensing flows for next-generation power units*. Ph.D thesis — Delft University of Technology, 2019. Cited 9 times in pages 17, 27, 28, 29, 55, 56, 59, 88, and 97.

Azzini, L.; Pini, M. Numerical investigation of high pressure condensing flows in supersonic nozzles. *Journal of Physics: Conference Series*, v. 821, p. 012008, 03 2017. Cited 4 times in pages 27, 29, 50, and 56.

Bakhtar, F.; Young, J. B.; White, A. J.; Simpson, D. A. Classical nucleation theory and its application to condensing steam flow calculations. *Proceedings of the Institution of Mechanical Engineers, Part C: Journal of Mechanical Engineering Science*, v. 219, n. 12, p. 1315–1333, 2005. Cited 7 times in pages 25, 28, 47, 50, 51, 52, and 113.

Barschdorff, D. Verlauf der zustandsgrößen und gasdynamische zusammenhänge bei der spontanen kondensation reinen wasserdampfes in lavaldüsen. *Forschung im Ingenieurwesen*, n. 37, p. 146–157, 1971. Cited 5 times in pages 18, 21, 23, 26, and 27.

Bell, I. H.; Wronski, J.; Quoilin, S.; Lemort, V. Pure and pseudo-pure fluid thermophysical property evaluation and the open-source thermophysical property library coolprop. *Industrial & Engineering Chemistry Research*, v. 53, n. 6, p. 2498–2508, 2014. Cited 3 times in pages 31, 52, and 61.

Bier, K.; Ehrler, F.; Niekrawietz, M. Experimental investigation and computer analysis of spontaneous condensation in stationary nozzle flow of CO2-air mixtures. *Adiabatic Waves in Liquid-Vapor Systems*, p. 113–127, 01 1990. Cited 2 times in pages 27 and 29.

Bier, K.; Ehrler, F.; Theis, G. Spontaneous condensation in stationary nozzle flow of carbon dioxide in a wide range of density. *Adiabatic Waves in Liquid-Vapor Systems*, p. 129–141, 1990. Cited 11 times in pages 5, 22, 23, 27, 28, 51, 69, 89, 90, 91, and 92.

Blondel, F.; Audebert, B.; Pasutto, T.; Stanciu, M. Condensation models and boundary conditions for non-equilibrium wet steam flows. 06 2015. Cited 7 times in pages 18, 26, 29, 54, 55, 56, and 59.

Blythe, P. A.; Shih, C. J. Condensation shocks in nozzle flows. *Journal of Fluid Mechanics*, Cambridge University Press, v. 76, n. 3, p. 593–621, 1976. Cited 3 times in pages 23, 25, and 41.

Bolaños-Acosta, A.; Restrepo, J.; Simões-Moreira, J. Two semi-analytical approaches for solving condensation shocks in supersonic nozzle flows. *International Journal of Heat and Mass Transfer*, v. 173, p. 121212, 2021. Cited in page 97.

Brinckman, K. W.; Hosangadi, A.; Liu, Z.; Weathers, T. Numerical simulation of non-equilibrium condensation in supercritical CO2 compressors. Vol. 9: Oil and Gas Applications; Supercritical CO2 Power Cycles; Wind Energy, 2019. Cited 3 times in pages 28, 29, and 56.

Carmo, b.; Orselli, R.; Galdino, R.; Volpe, E.; Cato, A.; Kavaba, L.; Costa, U.; Calvacante, J.; Hayashi, M.; Silva, E.; Yamabe, P.; Simões-Moreira, J.; Restepo, J.; Bolaños-Acosta, A.; Avancini, B.; Baxmann, I.; Costa, R.; Junio, D. *Development of gas supersonic separators - optimisation, numerical simulation and experiments*. [S.l.: s.n.], 2020. (Technical report, 3). Cited 2 times in pages 104 and 105.

Courtney, W. G. Remarks on homogeneous nucleation. *The Journal of Chemical Physics*, v. 35, n. 6, p. 2249–2250, 1961. Cited 2 times in pages 25 and 51.

Dykas, S. Numerical calculation of the steam condensing flow. *Task Quarterly*, v. 5, p. 519–535, 01 2001. Cited 10 times in pages 17, 18, 25, 28, 29, 51, 53, 54, 55, and 56.

Dykas, S.; Wróblewski, W. Single- and two-fluid models for steam condensing flow modeling. *International Journal of Multiphase Flow*, v. 37, n. 9, p. 1245 – 1253, 2011. Cited 4 times in pages 26, 29, 56, and 58.

Dykas, S.; Wróblewski, W. Numerical modelling of steam condensing flow in low and high-pressure nozzles. *International Journal of Heat and Mass Transfer*, v. 55, n. 21, p. 6191 – 6199, 2012. Cited 7 times in pages 26, 29, 54, 55, 56, 59, and 88.

Elliott, J. R.; Lira, C. T. *Introductory Chemical Engineering Thermodynamics*. 2nd. ed. [S.l.]: Prentice Hall, 2012. (Series in the Physical and Chemical Engineering Sciences). Cited in page 34.

Fakhari, K. *Numerical modeling and investigation of unsteady phenomena in condensing flows of industrial steam turbines*. Ph.D thesis — Ruhr-Universität Bochum, 2010. Cited 7 times in pages 16, 26, 29, 52, 53, 55, and 56.

Farag, A. Numerical study on condensation process of steam flow in nozzles. *International Journal of Advancements in Technology*, v. 06, 01 2015. Cited 4 times in pages 27, 29, 56, and 69.

Feder, J.; Russell, K. C.; Lothe, J.; G.M., P. Homogeneous nucleation and growth of droplets in vapours. *Advances in Physics*, Taylor and Francis, v. 15, n. 57, p. 111–178, 1966. Cited in page 25.

Grübel, M.; Starzmann, J.; Schatz, M.; Eberle, T.; Vogt, D. M.; Sieverding, F. Two-Phase Flow Modeling and Measurements in Low-Pressure Turbines: Part 1 — Numerical Validation of Wet Steam Models and Turbine Modeling. In: . [S.l.: s.n.], 2014. (Turbo Expo: Power for Land, Sea, and Air, Volume 1B: Marine; Microturbines, Turbochargers and Small Turbomachines; Steam Turbines). Cited 5 times in pages 26, 29, 51, 54, and 56.

Guha, A. A unified theory of aerodynamic and condensation shock waves in vapor-droplet flows with or without a carrier gas. *Physics of Fluids*, v. 6, n. 5, p. 1893–1913, 1994. Cited 5 times in pages 23, 24, 25, 41, and 96.

Gyarmathy, G. *Grundlagen einer theorie der naßdamfturbine*. 246 p. Ph.D thesis — ETH Zürich, 1962. Cited 8 times in pages 25, 26, 27, 53, 54, 55, 56, and 76.

Gyarmathy, G. Nucleation of steam in high-pressure nozzle experiments. *Proceedings of the Institution of Mechanical Engineers, Part A: Journal of Power and Energy*, v. 219, n. 6, p. 511–521, 2005. Cited 13 times in pages 5, 6, 22, 23, 26, 27, 82, 83, 84, 85, 86, 87, and 88.

Hasini, H.; Zamri, Y.; Abd, N. Numerical Modeling of Wet Steam Flow in Steam Turbine Channel. In: University Tenaga Nasional. *Mechanical Engineering*. Malaysia, 2012. cap. 19, p. 670. Cited in page 16.

Heinze, D. *Physically-Based Models for Two-Phase Flow Phenomena in Steam Injectors A One-Dimensional Simulation Approach*. 72 p. Ph.D thesis — Karlsruher Institut für Technologie, 2015. Cited 11 times in pages 16, 17, 27, 29, 46, 52, 53, 69, 70, 88, and 91.

Heybey, W. H.; Reed, S. G. Weak detonations and condensation shocks. *Journal of Applied Physics*, AIP Publishing, v. 26, n. 8, p. 969–974, 1955. Cited 2 times in pages 23 and 41.

Hill, P. G. Condensation of water vapour during supersonic expansion in nozzles. *Journal of Fluid Mechanics*, v. 25, p. 593–620, 1966. Cited 5 times in pages 25, 27, 53, 55, and 56.

Imaev, S. Z.; Bagirov, L. A.; Borisov, V. E.; Voytenkov, E. V.; Engineering, E. New low temperature process of CO2 recovery from natural gases. In: *SPE Asia Pacific Oil & Gas Conference and Exhibition*. [S.l.: s.n.], 2014. Cited in page 18.

Kantrowitz, A. Nucleation in very rapid vapor expansions. *The Journal of Chemical Physics*, v. 19, n. 9, p. 1097–1100, 1951. Cited 2 times in pages 25 and 51.

Karagiannis, A. *Numerical Examination of Non-Equilibrium Condensation in Supersonic Micronozzles*. 126 p. M.Sc thesis — Delft University of Technology, 2020. Cited 2 times in pages 24 and 56.

Kim, Y. J.; Wyslouzil, B. E.; Wilemski, G.; Wölk, J.; Strey, R. Isothermal nucleation rates in supersonic nozzles and the properties of small water clusters. *The Journal of Physical Chemistry A*, v. 108, n. 20, p. 4365–4377, 2004. Cited 2 times in pages 22 and 23.

Korpela, S. *Principles of Turbomachinery*. Second edition. [S.l.]: Wiley and Sons, 2012. Cited 4 times in pages 24, 40, 41, and 46.

Kuo, K. *Principles of combustion*. [S.l.]: John Wiley, 2005. Cited 3 times in pages 39, 42, and 44.

Lamanna, G. *On nucleation and droplet growth in condensing nozzle flows*. Ph.D thesis — Technische Universiteit Eindhoven, 2000. Cited 12 times in pages 16, 21, 22, 23, 28, 29, 46, 50, 51, 52, 53, and 55.

Lemmon, E. W.; ; Bell, I. H.; Huber, M. L.; McLinden, M. O. *NIST Standard Reference Database 23: Reference Fluid Thermodynamic and Transport Properties-REFPROP, Version 10.0, National Institute of Standards and Technology*. 2018. Cited in page 52.

Lettieri, C.; Paxson, D.; Spakovszky, Z.; Bryanston-cross, P. Characterization of non-equilibrium condensation of supercritical carbon dioxide in a de laval nozzle. *Journal of Engineering for Gas Turbines and Power*, v. 140, 09 2017. Cited 4 times in pages 16, 22, 23, and 28.

Moore, M.; Walters, P.; Crane, R.; Davidson, B. *Predicting the fog drop size in wet steam turbines*. Warwick: [s.n.], 1973. 37–73 p. Cited 13 times in pages 4, 5, 18, 21, 23, 24, 26, 27, 55, 75, 76, 77, and 78.

Moses, C. A.; Stein, G. D. On the Growth of Steam Droplets Formed in a Laval Nozzle Using Both Static Pressure and Light Scattering Measurements. *Journal of Fluids Engineering*, v. 100, n. 3, p. 311, 1978. Cited 9 times in pages 5, 18, 21, 23, 26, 27, 79, 93, and 95.

Mulero, A.; Cachadiña, I. Recommended correlations for the surface tension of several fluids included in the refprop program. *Journal of Physical and Chemical Reference Data*, v. 43, n. 2, p. 023104, 2014. Cited in page 52.

Niknam, P. H.; Mortaheb, H. R.; Mokhtarani, B. Dehydration of low-pressure gas using supersonic separation: Experimental investigation and CFD analysis. *Journal of Natural Gas Science and Engineering*, v. 52, p. 202–214, 2018. Cited 2 times in pages 16 and 17.

Oliphant, T. E. *A guide to NumPy*. [S.l.]: Trelgol Publishing USA, 2006. v. 1. Cited in page 60.

Oswatisch, K. Kondensationsercheinungen in Uberschallduisen. *Math. Mech*, v. 22, p. 1–14, 1942. Cited in page 24.

Pandey, A. *Numerical Modeling of Non- Equilibrium Condensing Steam Flows*. 74 p. M.Sc thesis — Delft University of Technology, 2014. Cited 12 times in pages 16, 26, 27, 29, 30, 31, 39, 47, 50, 52, 53, and 59.

Paxson, D. *Experimental Characterization of Condensation Behavior for Metastable Carbon Dioxide*. 191 p. M.Sc thesis — Massachusetts Institute of Technology, 2016. Cited 6 times in pages 22, 23, 27, 28, 31, and 105.

Pouring, A. A. Thermal choking and condensation in nozzles. *Physics of Fluids*, v. 8, n. 10, p. 1802–1810, 1965. Cited in page 24.

Powell, M. J. D. An efficient method for finding the minimum of a function of several variables without calculating derivatives. *The Computer Journal*, v. 7, n. 2, p. 155–162, 01 1964. Cited in page 61.

Pratt, R. Using the Peng-Robinson equation of state. *Chem. Eng. Educ.*, n. 35, p. 112–139, 2001. Cited in page 35.

Restrepo, J.; Bolaños-Acosta, A. F.; Simões-Moreira, J. Theoretical analysis of supersonic phase change for carbon dioxide in a de laval nozzle. In: *The 25 th international congress of refrigeration*. [S.l.: s.n.], 2019. Cited 2 times in pages 27 and 28.

Reynolds, W.; Colonna, P. *Thermodynamics: Fundamentals And Engineering Applications*. 1th. ed. Cambridge: Cambridge University Press, 2018. 420 p. Cited 3 times in pages 33, 35, and 112.

Senguttuvan, S.; Lee, J.-C. Numerical study of wet-steam flow in moore nozzles. *Journal of Mechanical Science and Technology*, v. 33, p. 4823–4830, 10 2019. Cited 5 times in pages 27, 29, 31, 56, and 79.

Sidin, R. S. R. *Droplet size distribution in condensing flow*. 199 p. Ph.D thesis — University of Twente, 2009. Cited 3 times in pages 16, 28, and 29.

Simões-Moreira J. R. *Adiabatic evaporation waves*. 275 p. Ph.D thesis — Rensselaer Polytechnic Institute, 1994. Cited 3 times in pages 40, 44, and 105.

Simões-Moreira, J. R.; Shepherd, J. E. Evaporation waves in superheated dodecane. *Journal of Fluid Mechanics*, Cambridge University Press, v. 382, p. 63–86, 1999. Cited 2 times in pages 40 and 44.

Simpson, J. A.; Weiner, E. S. C. *The Oxford English dictionary*. [S.l.]: Clarendon Press, 1989. (The Oxford English Dictionary, v. 17). Cited in page 16.

Sinha, S.; Wyslouzil, B. E.; Wilemski, G. Modeling of H2O/D2O condensation in supersonic nozzles. *Aerosol Science and Technology*, v. 43, n. 1, p. 9–24, 2009. Cited 8 times in pages 22, 28, 29, 57, 58, 68, 69, and 70.

Smith, J.; Ness, H. V.; Abbott, M.; Swihart, M. *Introduction to Chemical Engineering Thermodynamics*. 8. ed. [S.l.]: McGraw-Hill Education, 2018. Cited 4 times in pages 31, 32, 33, and 35.

Smołka, K.; Dykas, S.; Majkut, M.; Strozik, M. Application of a single-fluid model for the steam condensing flow prediction. *Journal of Physics: Conference Series*, IOP Publishing, v. 760, p. 012028, oct 2016. Cited in page 58.

Sova, L.; Jun, G.; Šťastný, M. Modifications of steam condensation model implemented in commercial solver. *AIP Conference Proceedings*, v. 1889, n. 1, p. 020039, 2017. Cited 6 times in pages 27, 29, 51, 54, 56, and 79.

Span, R.; Wagner, W. A new equation of state for carbon dioxide covering the fluid region from the triple-point temperature to 1100 K at pressures up to 800 MPa. *Journal of Physical and Chemical Reference Data*, v. 25, n. 6, p. 1509–1596, 1996. Cited 3 times in pages 28, 31, and 32.

Stepchkov, A. A. Condensation Shocks in Supersonic Nozzles. *Journal of the American Rocket Society*, v. 30, n. 7, p. 695–699, 1960. Cited in page 24.

Thompson, P. *Compressible-fluid dynamics*. [S.l.]: McGraw-Hill, 1988. (Control Systems Engineering Series). Cited 8 times in pages 23, 36, 37, 38, 40, 41, 44, and 63.

Trela, M.; Kwidzinski, R.; Butrymowicz, D.; Karwacki, J. Exergy analysis of two-phase steam–water injector. *Applied Thermal Engineering*, v. 30, p. 340–346, 03 2010. Cited 2 times in pages 17 and 91.

Turns, S. *An Introduction to Combustion: Concepts and Applications*. [S.l.]: McGraw-Hill, 2012. (McGraw-Hill series in mechanical engineering). Cited in page 39.

Van der Stelt, T. P.; Nannan, N. R.; Colonna, P. The iPRSV equation of state. *Fluid Phase Equilibria.*, v. 330, p. 24–35, 2012. Cited 4 times in pages 30, 31, 33, and 61.

Van Rossum, G. *Python Reference Manual*. Amsterdam: Stichting Mathematisch Centrum, 1995. 59 p. Cited in page 60.

Vargaftik, N. B.; Volkov, B. N.; Voljak, L. D. International tables of the surface tension of water. *Journal of Physical and Chemical Reference Data*, v. 12, n. 3, p. 817–820, 1983. Cited in page 52.

Virtanen, P.; Gommers, R.; Oliphant, T. E.; Haberland, M.; Reddy, T.; Cournapeau, D.; Burovski, E.; Peterson, P.; Weckesser, W.; Bright, J.; van der Walt, S. J.; Brett, M.; Wilson, J.; Millman, K. J.; Mayorov, N.; Nelson, A. R.; Jones, E.; Kern, R.; Larson, E.; Carey, C.; Polat, I.; Feng, Y.; Moore, E. W.; VanderPlas, J.; Laxalde, D.; Perktold, J.; Cimrman, R.; Henriksen, I.; Quintero, E.; Harris, C. R.; Archibald, A. M.; Ribeiro, A. H.; Pedregosa, F.; van Mulbregt, P.; Contributors, S. . SciPy 1.0: Fundamental algorithms for scientific computing in python. *Nature Methods*, 2020. Cited 2 times in pages 60 and 61.

Wagner, W.; Cooper, J. R.; Dittmann, A.; Kijima, J.; Kretzschmar, H.; Kruse, A.; Mares, R.; Oguchi, K.; Sato, H.; Stocker, I.; Sifner, O.; Takaishi, Y.; Tanishita, I.; Trubenbach, J.; Willkommen, T. The IAPWS Industrial Formulation 1997 for the Thermodynamic Properties of Water and Steam . *Journal of Engineering for Gas Turbines and Power*, v. 122, n. 1, p. 150–184, 01 2000. Cited in page 30.

Wagner, W.; Pruß, A. The IAPWS formulation 1995 for the thermodynamic properties of ordinary water substance for general and scientific use. *Journal of Physical and Chemical Reference Data*, v. 31, n. 2, p. 387–535, 2002. Cited 3 times in pages 28, 31, and 32.

Wegener, P.; Mack, L. Condensation in supersonic and hypersonic wind tunnels. *Advances in Applied Mechanics*, v. 5, p. 307 – 447, 1958. Cited 10 times in pages 23, 24, 40, 41, 43, 44, 46, 52, 67, and 97.

Wegener, P. P. Water vapor condensation process in supersonic nozzles. *Journal of Applied Physics*, v. 25, n. 12, p. 1485–1491, 1954. Cited 3 times in pages 21, 24, and 49.

Yang, Y.; Shen, S. Numerical simulation on non-equilibrium spontaneous condensation in supersonic steam flow. *International Communications in Heat and Mass Transfer*, v. 36, n. 9, p. 902 – 907, 2009. Cited 6 times in pages 18, 26, 29, 31, 55, and 56.

Yellott, J. Supersaturated Steam. *Transactions of the American Society of Mechanical Engineers*, v. 56, n. 1, p. 412–430, 1933. Cited in page 47.

Young, J. *Spontaneous Condensation of Steam in Supersonic Nozzles*. [S.l.]: Cambridge University, 1980. (Technical report). Cited 7 times in pages 25, 26, 27, 53, 54, 56, and 76.

Young, J. B. An equation of state for steam for turbomachinery and other flow calculations. *Journal of Engineering for Gas Turbines and Power*, v. 110, n. 1, p. 1–7, 1988. Cited 5 times in pages 25, 26, 27, 29, and 30.

Young, J. B. Two-dimensional, nonequilibrium, wet-steam calculations for nozzles and turbine cascades. *Journal of Turbomachinery*, v. 114, n. 3, p. 569–579, 07 1992. Cited 2 times in pages 58 and 59.

Young, J. B.; Guha, A. Normal shock-wave structure in two-phase vapour-droplet flows. *Journal of Fluid Mechanics*, v. 228, p. 243–274, 1991. Cited 3 times in pages 25, 28, and 59.

ANNEX A – INSTRUMENTATION AND DATA ACQUISITION SYSTEM FOR A SUPERSONIC GAS FLOW SEPARATOR

It is worth to mention that along this research development, it was also required to assist project 39 of the Research Centre for Gas Innovation hosted by Universidade de São Paulo with the instrumentation and data acquisition program of a supersonic gas flow separator test rig (Carmo et al., 2020).

A.1 Test rig's layout and description

Fig. A.1 displays the test rig layout, which is composed by six main locations, points 1 to 3 are called as "gas-mixture preparation zone", it consists of the carbon dioxide and air-compressed lines as well as a tank with capacity of 4 m^3, where the gas mixture with the desired mass-fraction is stored before running the experiments. Locations 4 to 6 belong to the test zone, when valve VA-001 is opened, gas flows through the settling chamber and consequently expands in the Laval nozzle. Finally, the main-stream is liberated to the medium by allowing the gas to flow to the exhaust when valves VA-002 and/or VA-003 are opened.

Note that Fig. A.1 only displays the data acquisition locations and valves that are activated

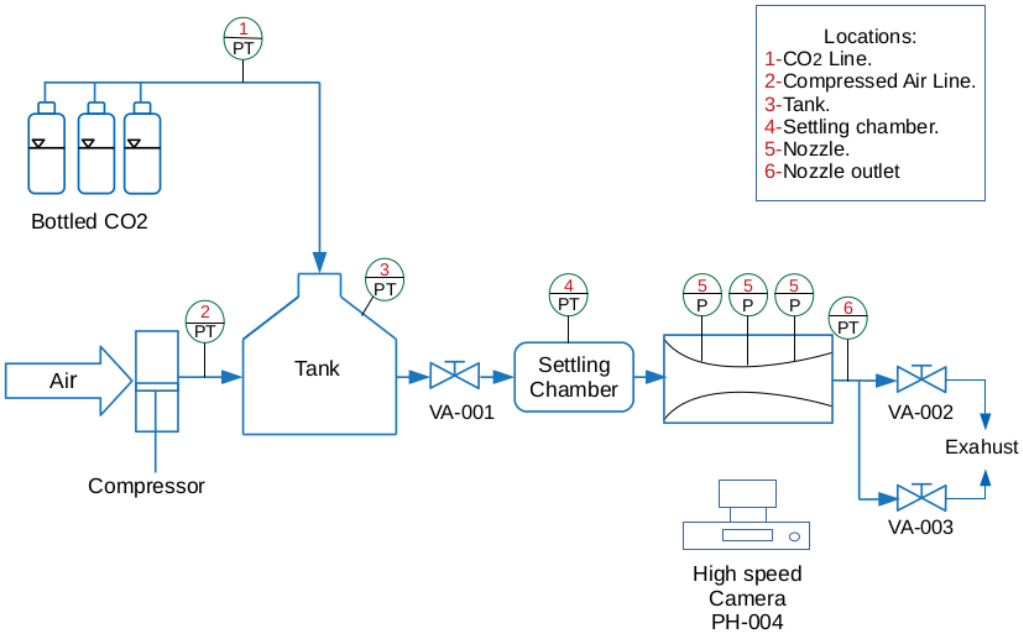

Figure A.1 – Test rig layout.

by means of the data acquisition system, other mechanical devices such as flow control valves have not been considered, refer to Carmo et al. (2020) for a detailed description of this test rig's components.

A.2 Signals and purchased instrumentation

Tab. A.1 reports the monitored variables in the test bench, their operating range and the desired signal to be acquired by the data acquisition system. Note that current input signals were selected for the gas preparation zone due to their low fluctuation and response rate when acquired. In turn, voltage signals have been chosen for the test zone because high sampling rates are required to characterize condensation phenomena in compressible flows, especially the pressure profile along the convergent-divergent nozzle.

Table A.1 – Required Input Signals.

Location	Variable	Tag Name	Range	Desired Signal
CO_2 Line	Pressure	CO2-PR01	0 to 44 bar	Current
	Temperature	CO2-PT01	-10 to 30 ^oC	
Compressed Air Line	Pressure	AC-PR01	0 to 44 bar	
	Temperature	AC-PT01	0 to 60 ^oC	
Tank	Pressure	TK-PR01	0 to 45 bar	
	Temperature	TK-PT01	-5 to 30 ^oC	
	Temperature	TK-PT02	-5 to 30 ^oC	
Settling Chamber	Pressure	SLC-PR01	0 to 45 bar	
	Temperature	SLC-TC01	-10 to 30 ^oC	
Nozzle outlet	Pressure	NZO-PR01	0 to 45 bar	Voltage
	Temperature	NZO-TC01	-10 to 30 ^oC	
Nozzle	Pressure	KTE 1 ... 20	0 to 35 bar	

Further, Tab. A.2 lists the purchased sensors to satisfy the requirements described by Tab. A.1. It is worth to mention that 20 pressure transducers with reference XTC-190 from KULITE company were purchased to capture the pressure distribution in the nozzle. These sensors have a low response time, which makes them suitable for compressible flow characterization as reported by Simões-Moreira J. R. (1994) and Paxson (2016).

Table A.2 – Purchased instrumentation.

Sensor	Quantity	Reference	Signal	Range	Location
Pressure	2	WTP-4010	4 to 20 mA	0 to 59 bar	Tank
	1			0 to 44 bar	CO_2 line
	1			0 to 44 bar	Compressed air line
PT-100	1	WTT-5000		-10 to 30 °C	CO_2 line
	1			0 to 60 °C	Compressed air line
T Thermocouple	2	WTT-6000		-5 to 30 °C	Tank
Pressure	2	WTP-4010	0 to 5 V	0 to 45 bar	Nozzle test rig
Barometer	1	SSB04-01		260 to 1260 hPa	
Pressure	10	XTC-190	0 to 10 mV	0 to 17 bar	Nozzle
	10			0 to 35 bar	

With respect to the data acquisition system, the chassis cDAQ-9189 has been acquired from National Instruments, Tab. A.3 reports cDAQ-9189's modules. Note that just one module (NI-9472) is dedicated to digital outputs (to open valves VA-001, VA-002, VA-003 and to trigger a camera high speed camera PH-004). Moreover, a MCS 1000 Lynx amplifier has been used to input Kulite pressure transducers' signals in NI-9220 modules.

Table A.3 – Required Input Signals.

Module	Quantity	Sampling rate	Signal	Channels	Resolution
NI-9213	1	75 S/s	Thermocouple	16	24
NI-9220	2	100 kS/s/Ch	± 10 Volts	16	16
NI-9201	1	500 kS/s	± 10 Volts	8	12
NI-9203	2	25 kS/s	4 to 20 mA	8	16
NI-9472 (DO)	1	100 μs	On/Off	8	-

A.3 Data acquistion interface

The interface of the data acquisition system was built by using LabVIEW. As observed in Fig. A.2, the interface displays the measured variables in the main locations of the test rig according to Tabs. A.1 and A.2, it also reports the actual data acquisition system's sampling rate, which can be configured up to 25000 samples per second, as well as the pressure distribution in the nozzle in real time that has been set for two modes of operation, the first occurs when the experimental test is below 16 bar, for this case, the algorithm only displays information of 10 pressure transducers whose operating range is up to 16 bar. Otherwise, the plot is built from all pressure transducers in the nozzle. Moreover, the interface has four buttons to open the valves VA-001, VA-002, VA-003 and to trigger the high-speed camera PH-004. And the final feature is that the LabVIEW interface writes a file containing the recorded data from all sensors.

Figure A.2 – Data acquisition interface.

A.3.1 LabVIEW algorithm

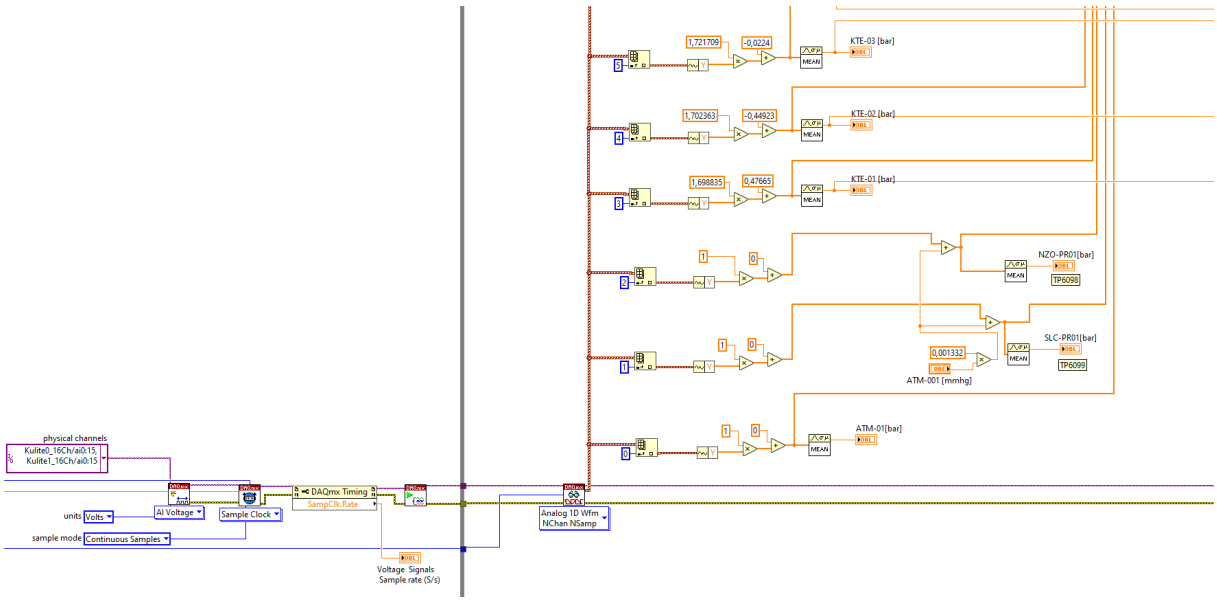

Figure A.3 – Data acquisition interface.

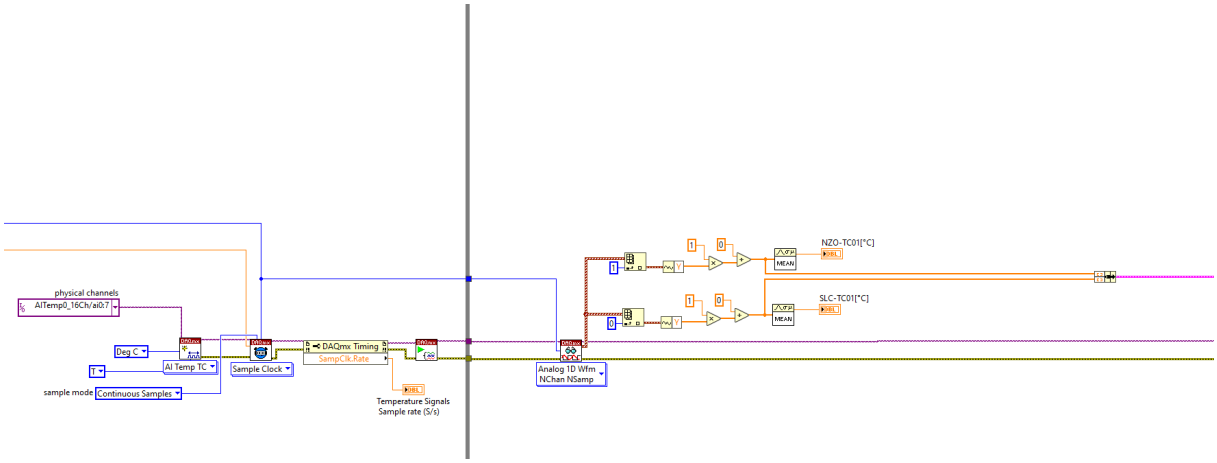

Figure A.4 – Data acquisition interface.

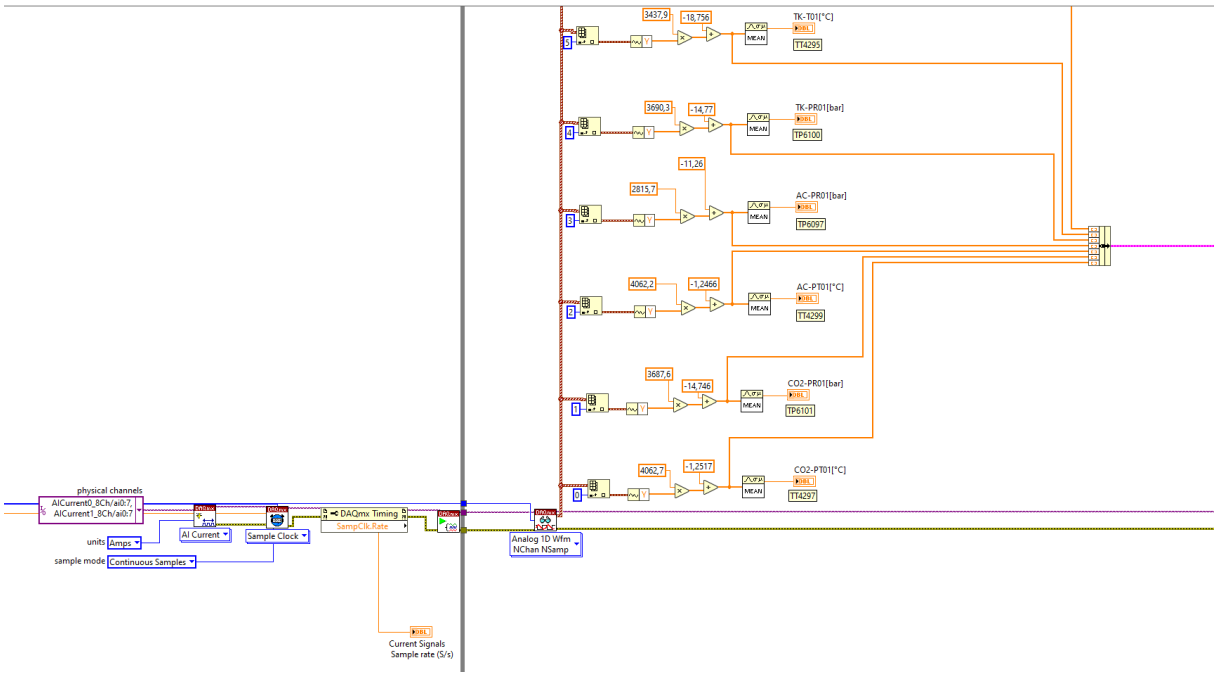

Figure A.5 – Data acquisition interface.

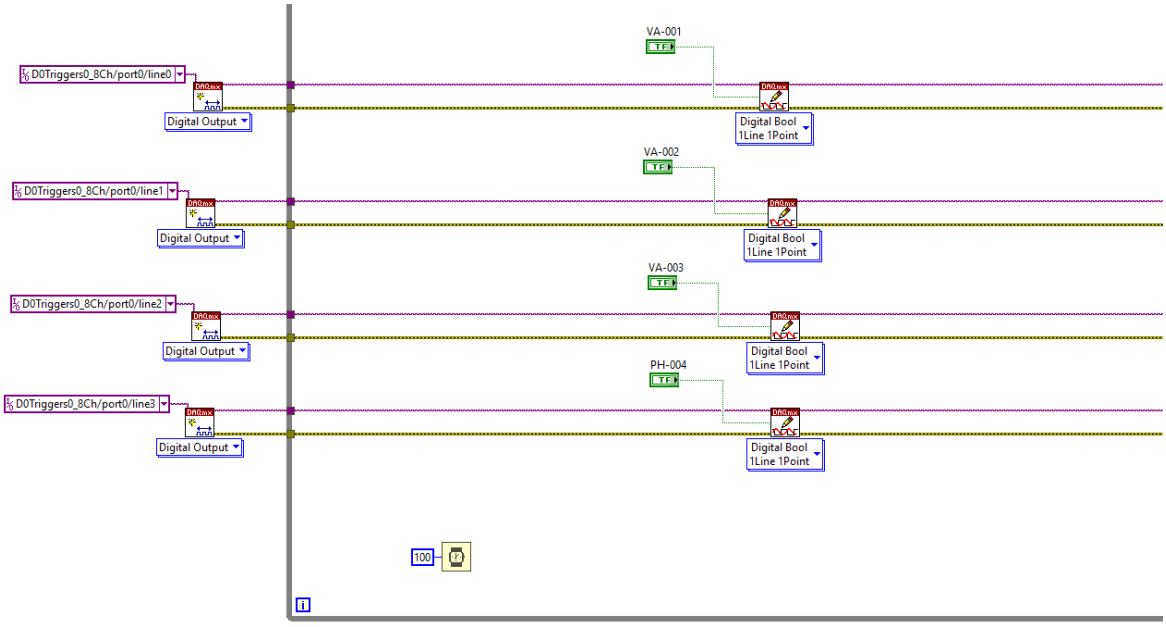

Figure A.6 – Data acquisition interface.

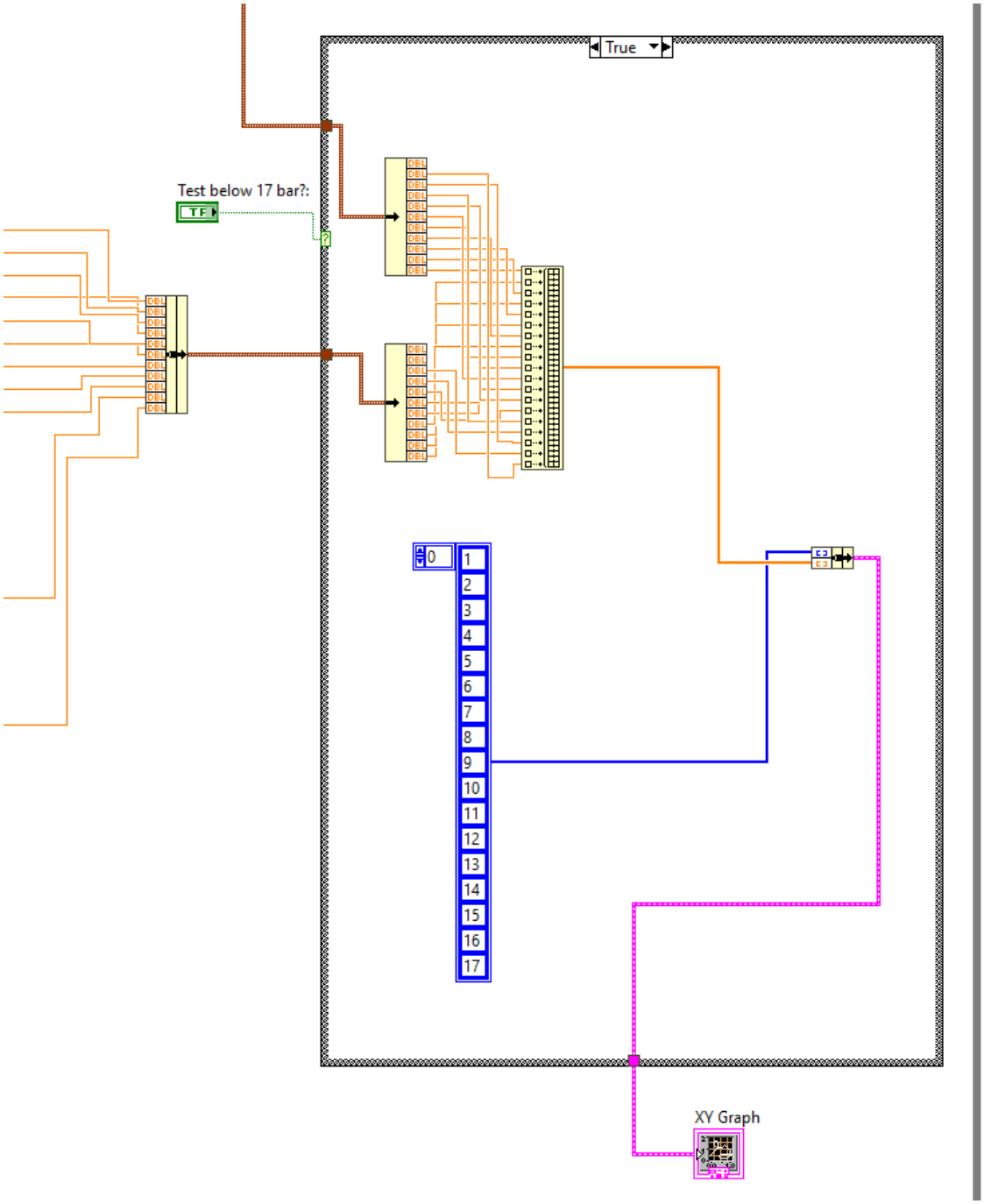

Figure A.7 – Data acquisition interface.

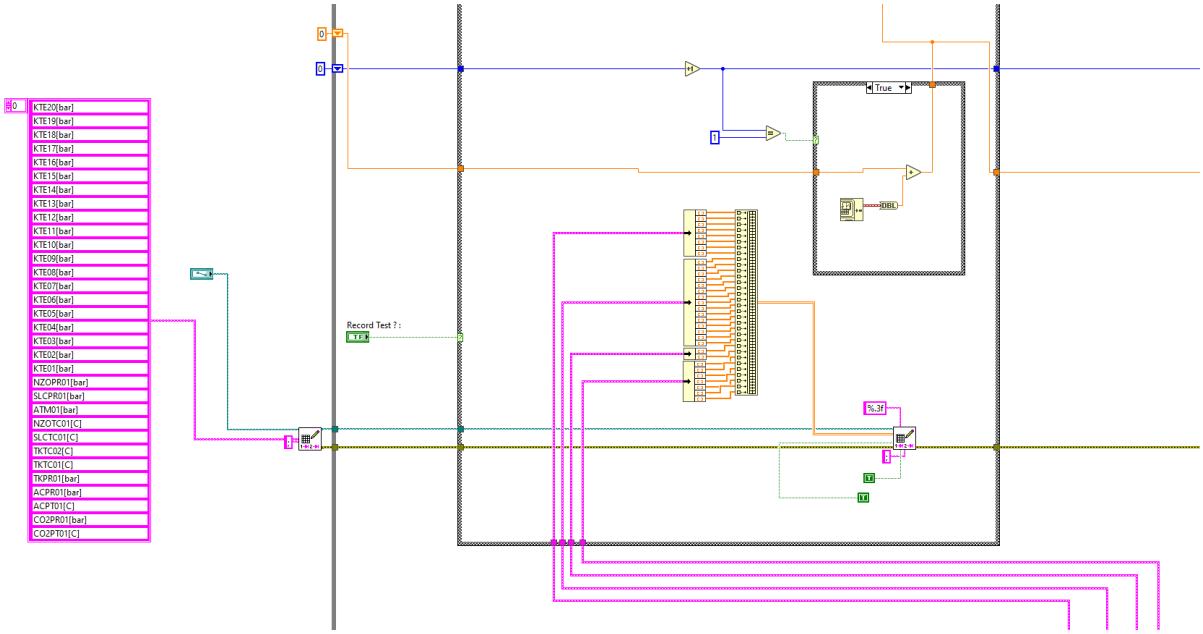

Figure A.8 – Data acquisition interface.

ANNEX B – MATHEMATICAL DERIVATIONS

B.1 Expressions for iPRSV's heat capacities

The following procedures and mathematical expressions have been taken from (Reynolds; Colonna, 2018).

The second derivative term of a (previously determined by Eq. (3.10)) in respect to the temperature is defined by:

$$\frac{d^2a}{dT^2} = 2a_c \left[\left(\tau_1 \frac{dk}{dT} - \frac{k}{2T_c\sqrt{T_r}} \right)^2 + (1+\tau_1 k) \left(\frac{k}{T_c^2 T_r^{3/2}} - \frac{\frac{dk}{dT}}{T_c\sqrt{T_r}} + \tau_1 \frac{d^2k}{dT^2} \right) \right] \tag{B.1}$$

Eq. (B.2) refers the second derivative of the k term in respect to the temperature.

$$\frac{d^2k}{dT^2} = \frac{-k_1(T_x - T_y)}{T_c^2} \left[\frac{D}{T_x T_y} + \frac{1}{4T_z^2} + \frac{D^2 T_z}{T_y^3 (T_x - T_y)} \right] \tag{B.2}$$

Eq. (B.3) defines the isochoric heat capacity for the iPRSV EoS.

$$c_v = c_v^o + T \int_\infty^v \left(\frac{\partial^2 P}{\partial T^2} \right) dv \tag{B.3}$$

With:

$$\int_\infty^v \left(\frac{\partial^2 P}{\partial T^2} \right) dv = \frac{\frac{d^2a}{dT}}{2\sqrt{2}b} \ln \left[\frac{Z + \left(1+\sqrt{2}\right)\Psi}{Z + \left(1-\sqrt{2}\right)\Psi} \right] \tag{B.4}$$

And Eq. (B.5) determines the isobaric heat capacity for the iPRSV EoS:

$$c_p = c_v - T \frac{\left(\frac{\partial P}{\partial T}\right)_v^2}{\left(\frac{\partial P}{\partial v}\right)_T} \tag{B.5}$$

With:

$$\left(\frac{\partial P}{\partial T} \right)_v = \frac{R}{v-b} - \frac{\frac{da}{dT}}{v^2 + 2bv - b^2} \tag{B.6}$$

B.2 Derivation of the area-velocity relation

The following procedure has been adopted from Anderson (2003).

The mass conservation in a converging-diverging nozzle can be written as:

$$\rho u A = \text{ constant} \tag{B.7}$$

Eq. (B.7) yields:

$$d(\rho u A) = 0 \tag{B.8}$$

Eq. (B.9) is obtained by applying the derivative chain rule to Eq. (B.8).

$$d\rho uA + \rho du A + \rho u dA = 0 \tag{B.9}$$

Dividing Eq. (B.9) by the expression ρuA, we obtain:

$$\frac{d\rho}{\rho} + \frac{du}{u} + \frac{dA}{A} = 0 \tag{B.10}$$

Invoking the Euler's equation (Anderson, 2003):

$$\frac{dP}{\rho} = -udu \tag{B.11}$$

Eq. (B.11) may be also written as:

$$\left(\frac{dP}{d\rho}\right)\left(\frac{d\rho}{\rho}\right) = -udu \tag{B.12}$$

Calling the definition of speed of sound in Eq. (3.29).

$$\left(\frac{dP}{d\rho}\right)_s = w^2 \tag{B.13}$$

Substituting Eq. (B.13) into Eq. (B.12), yields:

$$\frac{d\rho}{\rho} = -\frac{u}{w^2}du = -Ma^2\frac{du}{u} \tag{B.14}$$

Finally, the area-velocity relation Eq. (3.44) is obtained from substituting Eq. (B.14) into Eq. (B.8) (Anderson, 2003):

B.3 Nucleation rate derivation

The following mathematical derivation has been adopted from Bakhtar et al. (2005)

$$n_g \cong n_1 \exp\left(-\frac{\Delta G}{k_B T_v}\right) \tag{B.15}$$

Where n_g and n_1 are respectively the numbers per unit volume of g-mers and monomers. The exponential term in parentheses is defined by:

$$\frac{\Delta G}{k_B} = \frac{A_s \sigma}{k_B T_v} g^{2/3} - g \ln(S) \tag{B.16}$$

With

$$4\pi r^2 = A_s g^{2/3} \tag{B.17}$$

Starting with equation Eq. (3.73), n_g is substituted from Eq. (B.15) to give

$$J = \left[\int_{g=1}^{\infty} \frac{1}{C_g n_1 \exp\left(-\Delta G/k_B T_v\right) dg}\right]^{-1} \tag{B.18}$$

C_g is proportional to $g^{2/3}$, which is a slowly varying function of g compared to the rapidly changing exponential term that passes through a sharp maximum at $g = g_*$. C_g is therefore

approximated by C_{g*}. ΔG is expanded as a Taylor series about g_* as:

$$\Delta G = \Delta G^* + (g - g_*) \left(\frac{\partial \Delta G}{\partial g} \right)_* + \left(\frac{g - g_*}{2} \right) \left(\frac{\partial^2 \Delta G}{\partial g^2} \right)_* + ... \tag{B.19}$$

Truncating after the second-order term and noting that $(\partial \Delta G / \partial g)_* = 0$ gives:

$$J = C_g n_1 Z_e \exp \left(-\frac{\Delta G^*}{k_B T_v} \right) \tag{B.20}$$

Where Z_e is the so-called Zeldovich factor, given by:

$$\frac{1}{Z_e} = \int_{g=1}^{\infty} \exp \left[- \left(\frac{\partial^2 \Delta G^*}{\partial g^2} \right) \frac{g - g_*}{2 k_B T_v} \right] dg \cong \left[\frac{-\left(\partial^2 \Delta G / \partial g^2 \right)}{2 \pi k_B T_v} \right]^{-1/2} \tag{B.21}$$

he second expression is obtained by extending the lower limit of the integral to $g = -\infty$. Evaluating $\partial^2 \Delta G / \partial g^2)$ from Eq. (B.16) and substituting into Eq. (B.20) gives 3.74.